# FRICTION STIR ALLOYING OF IMMISCIBLE MAGNESIUM ALLOY AND MILD STEEL WITH ALUMINIUM AND CARBON NANOTUBES AS ADDITIVES

SUFIAN RAJA

FACULTY OF ENGINEERING
UNIVERSITY OF MALAYA
KUALA LUMPUR

2022

# FRICTION STIR ALLOYING OF IMMISCIBLE MAGNESIUM ALLOY AND MILD STEEL WITH ALUMINIUM AND CARBON NANOTUBES AS ADDITIVES

**SUFIAN RAJA**

**THESIS SUBMITTED IN FULFILMENT OF THE REQUIREMENTS FOR THE DEGREE OF DOCTOR OF PHILOSOPHY**

**FACULTY OF ENGINEERING**
**UNIVERSITY OF MALAYA**
**KUALA LUMPUR**

**2022**

**UNIVERSITY OF MALAYA**

**ORIGINAL LITERARY WORK DECLARATION**

Name of Candidate: SUFIAN RAJA

Matric No: KVA180071, 17199034/1

Name of Degree: Doctor of Philosophy

Title of Thesis: Friction stir alloying of immiscible magnesium alloy and mild steel with aluminium and carbon nanotubes as additives

Field of Study: Manufacturing Processes (Engineering and Engineering Trades)

I do solemnly and sincerely declare that:

(1) I am the sole author/writer of this Work;
(2) This Work is original;
(3) Any use of any work in which copyright exists was done by way of fair dealing and for permitted purposes and any excerpt or extract from, or reference to or reproduction of any copyright work has been disclosed expressly and sufficiently and the title of the Work and its authorship have been acknowledged in this Work;
(4) I do not have any actual knowledge nor do I ought reasonably to know that the making of this work constitutes an infringement of any copyright work;
(5) I hereby assign all and every rights in the copyright to this Work to the University of Malaya ("UM"), who henceforth shall be owner of the copyright in this Work and that any reproduction or use in any form or by any means whatsoever is prohibited without the written consent of UM having been first had and obtained;
(6) I am fully aware that if in the course of making this Work I have infringed any copyright whether intentionally or otherwise, I may be subject to legal action or any other action as may be determined by UM.

Candidate's Signature Date: 17-08-2022

Subscribed and solemnly declared before,

Witness's Signature Date:

Name:

Designation:

**FRICTION STIR ALLOYING OF IMMISCIBLE MAGNESIUM ALLOY AND MILD STEEL WITH ALUMINIUM AND CARBON NANOTUBES AS ADDITIVES**

## ABSTRACT

With growing environmental concerns, the need for more energy-efficient vehicles is bigger today than ever, and producing lighter vehicle support structures is a promising way to increase efficiency. Magnesium alloys welded with steel propose the possibility of weight-efficient structures, with the stronger steel in critical locations and magnesium alloy in locations where a stronger material (usually heavier) is not required. Friction stir alloying (FSA), as a solid-state process, is shown to be a promising method for joining dissimilar/ immiscible metals by using additives to improve joint properties. Dissimilar materials joining AZ31-mild steel using Al-Mg additives and AZ61 magnesium alloy-mild steel using Al-CNT additives were successfully produced by the friction stir alloying process. Al-Mg powder additives were injected in a gap between AZ31 and the mild steel specimen's butt prior to welding. The experiments were performed for different weight percentages of Al-Mg powder additives at welding speeds of 25 mm/min, 50 mm/min and 100 mm/min with a constant tool rotational speed of 500 rpm. The effect of powder additives and welding speed on tensile strength, microhardness, characterisation across welding interface and fracture morphology were investigated. Tensile test results showed significant enhancement of tensile strength of 150 MPa for 10% Al and Mg (balance) powder additives welded joint compared to the tensile strength of 125 MPa obtained for welded joint without powder additives. The loss of aluminium in the alloy is compensated by Al-Mg powder addition during welding under a suitable heat input condition identified by varying welding speeds. Microstructural analysis revealed that the Al-Mg powder was well mixed and dispersed at the interface of the joint at a welding speed of 50 mm/min. Intermetallic compounds detected in the welding interface contributed to the welding

strength. In other material combinations, another promising magnesium alloy, AZ61 used to join with mild steel with Al-CNT additives by the friction stir alloying. Before welding, Al-CNT additives were too injected in a gap between the AZ61 and steel specimens. The experimentation was performed using different welding speeds while tool rotational speed was kept constant for varying weight percentages of carbon nanotubes (CNT) in Al powder. The influence of additives and welding speed on tensile strength and characterisation across the welding interface was studied. Tensile strength of joint with 3% CNT improved up to 222 Mpa. In terms of improving joint strength qualities, CNT has a significant impact. Al-rich Intermetallic compounds were found at the welding contact, while the formation of $Al_2MgC_2$ carbide was detected, which contributed to CNT strengthening effects all to improved welding strength.

Keywords: Friction stir alloying, carbon nanotubes, dissimilar joint, magnesium alloy, mild steel, nanoscale analysis, phase identification, intermetallic compound, characterisation, mechanical properties

**PENGALOIAN KACAU GESARAN DI ANTARA ALOI TIDAK TERCAMPUR MAGNESIUM DAN KELULI LEMBUT DENGAN ALUMINIUM DAN KARBON NANOTIUB SEBAGAI BAHAN TAMBAH**

## ABSTRAK

Seiring dengan perhatian terhadap alam sekitar yang semakin meningkat, keperluan untuk kenderaan yang lebih cekap tenaga semakin besar pada hari ini. Pembinaan struktur sokongan kenderaan yang lebih ringan adalah suatu cara yang menjanjikan penigkatan kecekapan. Aloi magnesium yang dikimpal dengan keluli boleh memberikan struktur yang cekap berat dengan keluli yang lebih kuat di lokasi kritikal dan aloi magnesium di lokasi di mana bahan yang lebih kuat (biasanya lebih berat) tidak diperlukan. Pengaloian Kacau Geseran (PKG) ialah suatu proses dalam keadaan pepejal, sebagai kaedah yang berpotensi tinggi untuk mencantumkan logam yang tidak serupa/tak larut dengan kehadiran bahan tambah untuk memperbaiki sifat sambungan. Bahan tidak serupa yang bergabung dengan aloi magnesium AZ31 menggunakan bahan tambah serbuk Aluminium /Magnesium dan aloi magnesium AZ61 bersama-sama dengan keluli lembut menggunakan bahan tambah Aluminium-Karbon Nano Tiub (Al-KNT) telah berjaya dihasilkan melalui proses pengaloian kacau geseran. Bahan tambah serbuk Al-Mg dimasukkan ke dalam celah sisi antara AZ31 dan keluli sebelum dikimpal. Eksperimen dilakukan untuk peratusan berat yang berbeza bagi bahan tambah serbuk Al-Mg pada kelajuan kimpalan 25 mm/min, 50 mm/min dan 100 mm/min dengan kelajuan putaran alat dimalarkan pada 500 putaran per minit. Kesan bahan tambah serbuk dan kelajuan kimpalan ke atas kekuatan tegangan, kekerasan mikro, pencirian merentasi antara muka kimpalan dan morfologi patah telah disiasat. Keputusan ujian tegangan menunjukkan peningkatan ketara kekuatan tegangan 150 MPa bagi 10% Al dan Mg (imbangan) bahan tambah sambungan dikimpal berbanding dengan kekuatan tegangan 125 MPa yang diperolehi untuk sambungan dikimpal tanpa bahan tambah. Kehilangan aluminium dalam

aloi telah ditampung penambahan serbuk Al-Mg semasa mengimpal di bawah keadaan input haba yang sesuai telah dikenal pasti, dengan kelajuan kimpalan yang berbeza-beza. Analisis mikrostruktur mendedahkan bahawa serbuk Al-Mg telah dicampur dengan baik dan tersebar pada muka sambungan pada kelajuan kimpalan 50 mm/min. Sebatian antara logam yang telah dikesan dalam antara muka kimpalan menyumbang kepada kekuatan kimpalan. Dalam eksperimen seterusnya, aloi magnesium AZ61 telah digunakan untuk bergabung dengan keluli lembut dengan bahan tambah Al-KNT melalui proses pengaloian kacau geseran. Sebelum dikimpal, bahan tambah Al-KNT telah disuntik dalam jurang antara AZ61 dan spesimen keluli. Percubaan dilakukan menggunakan kelajuan kimpalan yang berbeza manakala kelajuan putaran alat dikekalkan malar untuk peratusan berat karbon nano tiub yang berbeza-beza dalam serbuk Al. Pengaruh bahan tambah dan kelajuan kimpalan ke atas kekuatan tegangan dan pencirian merentasi antara muka kimpalan telah dikaji. Kekuatan tegangan sambunagn itu dengan 3% CNT bertambah baik sehingga 222 Mpa. Dari segi meningkatkan kualiti kekuatan sambungan, tambahan KNT menunjukkan impak yang ketara. Sebatian antara logam yang kaya dengan Al ditemui pada sentuhan kimpalan, manakala pembentukan karbida $Al_2MgC_2$ yang telah dikesan telah menyumbang kepada kesan pengukuhan untuk menghasilkan kekuatan kimpalan yang lebih baik.

Kata kunci: Pengaloian aduk geseran, tiub nano karbon, sambungan tidak serupa, aloi magnesium, keluli lembut, analisis skala nano, pengenalpastian fasa, sebatian antara logam, pencirian, sifat mekanikal

## ACKNOWLEDGEMENTS

To begin with the name of ALLAH Almighty who inculcated the consecration upon me to fulfill the requirements of everything that I want.

In the first place, I would like to record my gratitude to my supervisors Dr. Mohd Ridha Bin Muhamad and Associate Prof. Dr. Farazila Binti Yusof for their advice and guidance from the very early stage of this work as well as for giving me extraordinary experiences throughout the work. There extensive discussions around my work and interesting explorations in difficult concepts have been very helpful for this study. I am indebted to them more than they know.

I would also like to thank all the members of the Friction stir welding group, especially Mohammad Syahid Mohd Isa, Seyed Mehrdad Yamani, Mohammad Ashraf Ariffin, and Muhammad Zulhiqmi Mohd Jamil, for their continuous support and cooperation in the success of my research endeavour. I would like to thank Mr Mohd Fauzi bin Bakri and Mrs Hartini Binti Baharum, Assistant Engineer, Mechanical engineering department, University Malaya, for their valuable support during my research journey.

I would like to thankfully acknowledge the Ministry of Higher Education Malaysia for providing financial support. This research is supported by the Fundamental Research Grant Scheme No. FRGS/1/2018/TK10/UM/02/2.

I am immensely grateful to my dear parents, Ahmad Hasan and Ishrat Parveen, for their unwavering support, guidance, and prayers. I also wish to thank all my family members and friends especially Ms Amtul Rahman, for their support and prayers and all those who have contributed in one way or another towards the success of this work.

## TABLE OF CONTENTS

## LIST OF FIGURES

## LIST OF TABLES

## LIST OF SYMBOLS AND ABBREVIATIONS

| | | |
|---|---|---|
| CNT | : | Carbon nanotube |
| CMT | : | Cold metal transfer |
| CR | : | Cold rolled |
| FSA | : | Friction stir alloying |
| FSW | : | Friction stir welding |
| FSP | : | Friction stir processing |
| FPP | : | Friction stir powder processing |
| FW | : | Fusion welding |
| FSLW | : | Friction stir lap welding |
| FAST | : | Friction-stir assisted scribe technique |
| GI | : | Galvanized iron |
| GNP | : | Graphene nanoplatelet |
| GN | | Graphene sheet |
| IMC | : | Intermetallic compound |
| LBW | : | Laser beam welding |
| MIG | : | Metal inert gas |
| MAG | : | Metal active gas |
| MJ | : | Mechanical joining |
| Al | | Aluminium |
| Fe | | Ferrum |
| Mg | | Magnesium |
| RSW | : | Resistance spot welding |

## LIST OF APPENDICES

# CHAPTER 1: INTRODUCTION

Environmental pollution and scarcity of fossil fuels are significant issues affecting the world today. One of the biggest contributors to these problems is the transportation sector. It is estimated there are approximately 1.2 billion motor vehicles on the road, which accounts for 75 per cent amount of pollution, 27 per cent of emission of greenhouse gases and 756 litres of petrol consumption per year (Brinson, 2021; John, 2021). The amounts of pollution and fuel consumption can be reduced significantly by improving the vehicle's fuel efficiency. At the moment, steel accounts for more than half of the weight of a typical automobile (Murdoch, 2008).

One method to improve fuel efficiency is to lessen the vehicle's weight using lightweight materials such as magnesium and aluminium (Karakizis et al., 2019; Wang et al., 2017). However, some parts of the vehicle, such as the body frame and structures, still require the high strength and toughness that the traditional use of steel can only fulfil. A possible solution is by using dissimilar materials joints that reduce the weight of the component without compromising the requirements of strength and toughness.

Magnesium alloys prove to be a better option as a dissimilar joint material than aluminium alloys since they are nearly as strong as aluminium, but magnesium is 33% lighter. Additionally, magnesium alloys have good energy absorption characteristics and high specific strength and are widely available (Patel et al., 2013; Zhang et al., 2015). Magnesium alloys, on the other hand, have some drawbacks as compared to aluminium and steel-based alloys. The primary disadvantage of magnesium alloys is that most alloys exhibit high chemical reactivity and poor resistance to corrosion. Many recently developed AZ (Aluminium and Zinc) series magnesium alloys, such as AZ31, AZ61 and AZ91E, have shown good corrosion resistance to previous magnesium alloys and are also suitable for automotive applications.

Although newly produced magnesium alloys with improved corrosion resistance have allowed the use of these lightweight alloys in vehicles, joining methods continue to be a significant barrier to widespread adoption. Friction stir welding (FSW) is a solid-state welding process that has shown success in joining similar and dissimilar metals (Dharani & Suresh, 2022; Raj & Biswas, 2022). FSW has been implemented successfully to produce automotive sub-frame structures from dissimilar aluminium and steel joining (Kusuda, 2013). Numerous studies have been reported for joining dissimilar materials using FSW. From these researches joining mechanism of dissimilar materials can be understood (Doley & Kore, 2016; Pourali et al., 2017a; Wang et al., 2018; Yusof et al., 2016; Zhao et al., 2015). Researchers reported the effect of process parameters, welding conditions and with or without interlayer between workpieces for dissimilar materials welding (Boucherit et al., 2017; Buffa et al., 2019; Chen et al., 2018; Kar et al., 2018; Mokabberi et al., 2018). AZ series magnesium alloys were used in a few investigations of different FSW of Fe/Mg combinations (Kasai et al., 2015b; Sahu et al., 2021). Nevertheless, immiscible materials, including Fe/Mg, make it difficult to develop quality joints since the immiscible materials prevent the formation of an Intermetallic compound (IMC) at the interface. Filler materials or additive materials have received a lot of interest since they may be utilised for both similar and dissimilar welding. During the FSW, several researchers used filler materials or additives to analyse the material flow (Liu & Wu, 2015). Friction stir alloying (FSA), which is based on the concepts of friction stir welding, has recently gained a lot of interest as a composite joint formation process by employing additives at the interface and a particular place. FSA is a very successful technology for fabricating metal–matrix nanocomposites, fine-grained metals with superplasticity, homogenising powder metallurgy processed and formation of composite joints for improved processed properties (Agrawal et al., 2020; Moiduddin et al., 2021; Sharma et al., 2022; Sharma et al., 2020). Therefore, to fully utilise the advantages of dissimilar

joints, AZ series magnesium alloy and mild steel must be carefully tested and extended to various AZ series magnesium alloy/ mild steel configurations with additives.

## 1.1 Problem statement and research question

The joining of magnesium to steel is challenging since the maximum solubility of Fe in Mg is only 0.00043 wt.% (von Goldbeck, 1982). This means that at ambient temperature, magnesium and steel do not mix and interact with one another (Mao & Bell, 1979). Additionally, there are significant variations in magnesium alloys and steel's physical, chemical, and mechanical properties, restricting the use of traditional fusion or solid-state joining techniques. However, zinc-coated low-carbon steel has been joined with AZ31 magnesium alloy using FSW (Chen & Nakata, 2009). An IMC layer of $Fe_2Al_{13}$ was detected with no presence of Zn at the joining interface of the magnesium and steel. The presence of zinc has improved the weldability between magnesium alloy and steel, and a good joining performance was obtained. FSW between several magnesium alloys (pure AZ, AZ31, AZ61) with low carbon steel has shown that increasing the percentages of aluminium content in the Mg alloys would enhance the mechanical properties of the welded joint (Kasai et al., 2015a). It was shown that the AZ61 alloy, having high aluminium content, produces joints with the highest tensile strength. This has been attributed to the IMC formation of $Fe_2Al_5$ at the interface of the joint.

Several techniques have been proposed to overcome the immiscibility of joining dissimilar materials. A friction powder processing (FPP) method has been developed, which utilises the addition of metal powders into the joining interface. For the joining of Al-Fe, it was found that the addition of Al powder into the gap of the join prevented the formation of defects, while the hardness increased when Cu powder was used (Inada et al., 2010). A similar technique was used in friction stir processing (FSP) of aluminium matrix reinforced with Fe particles. The stirred zone area exhibited superior microhardness values compared to other regions (Sarkari et al., 2015). FSA is a modification of

the FSW in which the alloying materials are reinforced in the workpiece material either at the interface or at a specified spot for localised property improvement (Karthik et al., 2017). Apart from the metal particle as reinforcement, carbonaceous nanomaterials, namely carbon nanotubes (CNT) and graphene, have gathered attention as a prospective reinforcing nanomaterial in FSA due to their exceptional mechanical, chemical, thermal, tribological properties (Jayabalakrishnan & Balasubramanian, 2018; Montazerian et al., 2019; Zhao et al., 2017).

The method of reinforcing material introduction at the interface is a crucial factor in determining the properties of the reinforced joint. In the initial stage of reinforced FSW or simply FSA, researchers preferred the open groove method for applying reinforcing material and reinforcements were pressed into the groove tightly (Bahrami et al., 2014; Fallahi et al., 2017; Paidar et al., 2018). However, during the FSA process, reinforcing material was splattered out from grooves due to force generated during the process. This made an inappropriate proportion of reinforcing material available inside the welding zone. To avoid this spilling problem, some authors used a slurry of nanoparticles mixed with ethanol inside the open groove and made nanoparticles manageable (Dragatogiannis et al., 2016; Kartsonakis et al., 2016). In some experiments before welding, the open grooves were subjected to a pinless tool to avoid expulsion of the nanoparticles out of the groove during the process (Bodaghi & Dehghani, 2017; Karakizis et al., 2018a). However, this pinless tool processing creates extra work, which is not feasible in industry practice. Therefore it is necessary to develop a new method of additive materials application at the interface of workpiece materials. To date, no studies have been carried out on joining AZ series magnesium alloy and mild steel with aluminium powder and CNT as additive materials and dispersion of nano additive method is not developed using PEG. This defines the novelty of current research.

After looking into the problem statement following research, questions come into mind.

a) How can sound joining of Mg alloy and steel be accomplished?
b) How can the depletion of Al be controlled while joining the Mg alloy and mild steel?
c) How can the addition of CNT nanomaterials improve joint strength?
d) How can nano-additive be introduced at the joint interface for uniform dispersion?

## 1.2 Research objectives

This research aims to fabricate joints with good mechanical properties from AZ series magnesium alloys (AZ31 and AZ61) and mild steel using the FSA technique with additives and to understand the microstructural evolution and the joining mechanism of these joints. The following are the specific objectives of this study:

1. To implement a novel and innovative method of dispersing nano-additive in FSA.
2. To evaluate the role of aluminium particles additive in forming the intermetallic compound for strength enhancement in FSA of mild steel with AZ31 magnesium alloys.
3. To determine the joint quality and the joining mechanism involved in FSA of mild steel and AZ61 magnesium alloy with aluminium and CNT additives.
4. To explain the strengthening mechanism involved in improving AZ61 magnesium alloy and mild steel joint properties.

## 1.3 Scope of research

The current thesis is essential for both researchers and auto manufacturers. Therefore, this research would assist researchers and welding engineers in developing a thorough understanding of the mechanisms behind the joining of magnesium alloys and steels. Additionally, welding engineers can use the findings of this study to establish magnesium

alloys and steel FSA joints using additives with superior mechanical properties. Also, this research may serve as a guide for the automotive sector to consider implementing FSA techniques using metal particles and carbonaceous nanoparticles as additives in their production lines for joining magnesium alloy and steel components.

## 1.4 Thesis framework

The thesis has been divided into five chapters which are as follows: The first chapter provides a short introduction to the topic and states the problem and objectives of the work. The significance of the thesis outcome is also briefly described in this chapter.

Chapter two describes the background of magnesium alloy and steel friction stir welding with aspects of microstructural and mechanical properties. Furthermore, the effect of the FSA technique using additives in various similar and dissimilar material processing will be reviewed. The background of CNT and its application as an additive to improve process characteristics will be discussed briefly

Chapter three presents the experimental methods used in this study, including the unique method of nano-additive introduction at the interface.

Chapter four describes the experimentally observed results and correlation between mechanical properties and microstructural features.

Finally, chapter five provides conclusions of the research results and recommendations for future studies.

# CHAPTER 2: LITERATURE REVIEW

## 2.1 Importance and issues of magnesium alloy and steel joining

The continuous growth in fossil fuel usage and decline in availability necessitates innovative technology to overcome these issues. Also, automotive industries accounted for 27 per cent of world energy-related $CO_2$ emissions (Brinson, 2021; John, 2021). Reduced vehicle weight minimises oil consumption and $CO_2$ emissions. Steel typically contributes almost 50 per cent of a car's weight (Murdoch, 2008). So substituting steel using lightweight materials is an easy way to reduce the weight of the vehicle. Alloys of magnesium, aluminium, and carbon fibre polymeric materials have been used to substitute steel. In addition, it should be able to establish strong joints with preexisting steel parts. Carbon fibre polymeric materials are more substantial than magnesium alloys and aluminium alloys but less resistant to heat. Alloys of magnesium are approximately as strong as aluminium alloys but are 33 per cent lighter. While issues common to dissimilar material joining apply to magnesium-steel, there are also unique concerns. Table 2.1 summarises magnesium and iron's physical and mechanical properties (Song et al., 2018). Due to the enormous variations between magnesium and iron, Mg/steel joints experience immiscibility.

**Table 2.1: Properties of pure magnesium and iron properties** (Song et al., 2018)

| Properties | Magnesium | Iron |
|---|---|---|
| Crystal structure | Hexagonal close-packed | Body-centered cubic and Face-centered cubic |
| Melting point (°C) | 650 | 1538 |
| Boiling point (°C) | 1090 | 2861 |
| Thermal conductivity (W/m.K) | 156 | 80.4 |
| Density ($g/cm^3$) | 1.738 | 7.874 |

The dissimilar joint of Mg and steel is distinct from Mg/Al and steel/Al joint welding. Numerous Fe-Al compounds are detected in the Fe/Al joint, as shown in Figure 2.1, all of which affect the Al/Fe joint's efficiency.

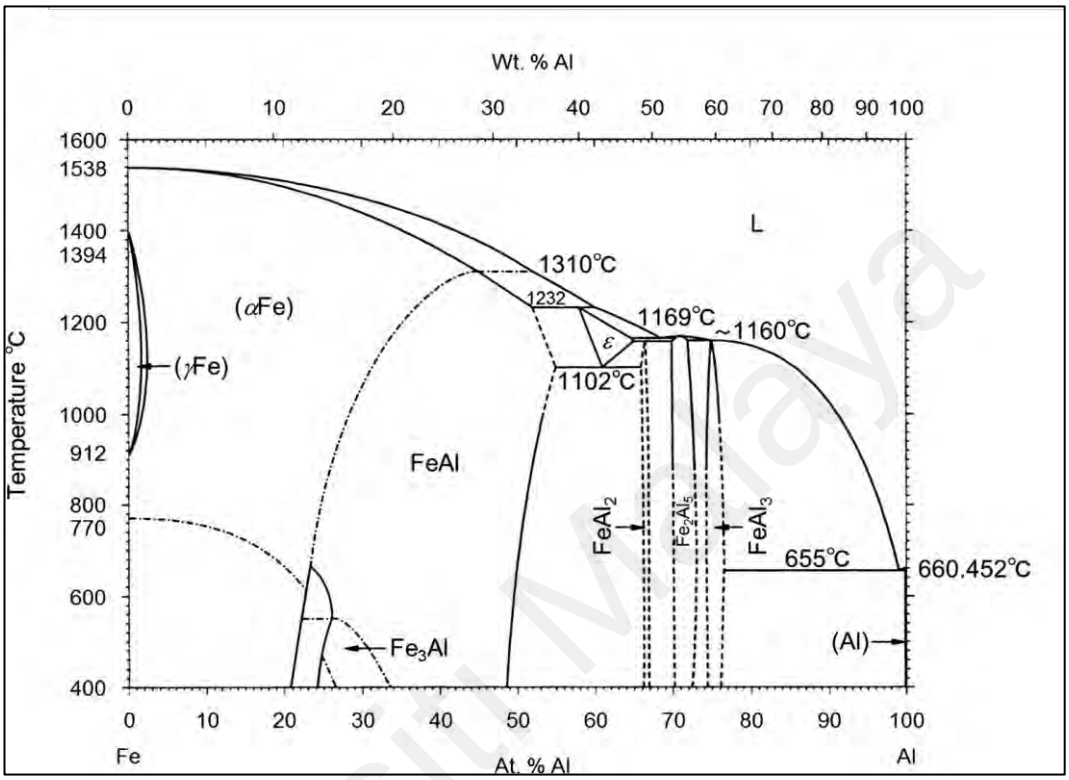


**Figure 2.1: Iron-Aluminium binary phase diagram** (Kasai et al., 2015a)

However, no IMC formed in the Mg/Fe joint, and the Mg-Fe system has low solid solubility, as shown in Figure 2.2. As a result, forming an interface layer and obtaining an appropriate magnesium and steel joint is challenging. Additionally, Fe has a significantly greater melting point (about 1538 ºC) than Mg (Kaye & Laby, 1997). In fact, the Mg boiling point (about 1090 ºC) is much lower than the Fe melting point (Kaye & Laby, 1997). This means that as steel melts, magnesium is instantly vaporized.

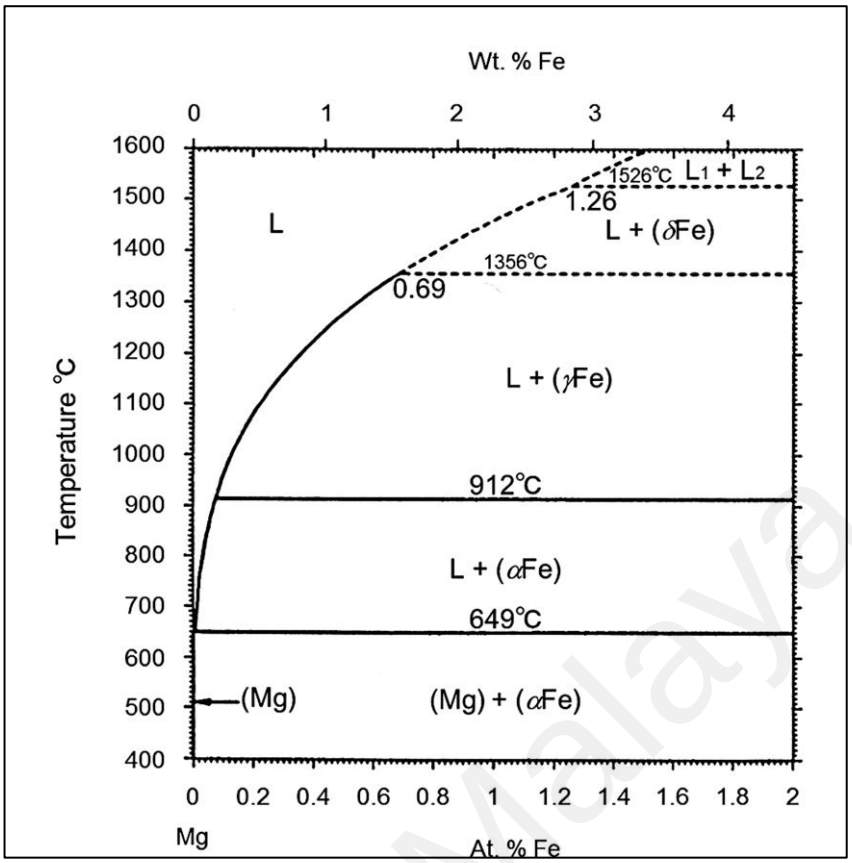


**Figure 2.2: Magnesium-Iron binary phase diagram** (Kasai et al., 2015a)

As a result, understanding how to produce an interface layer is critical for joining immiscible magnesium/steel. Enhancing interfacial reaction can form an IMC layer, resulting in a practical magnesium/steel welding. At this stage, the study on the joining of immiscible magnesium/steel dissimilar metals focuses primarily on utilising the alloying elements from base metal to form IMC aspects. The interface layer's elements are derived primarily from the base metal or incorporating additive elements. Thus, the objective of producing various types of IMC layers could be accomplished by selecting various components of the base metal and appropriate reinforcing elements, such as Al, Cu, Ni, Cu-Zn layers on the adjacent surface or Ni, Zn, and Sn coating.

## 2.2 Different methods for joining magnesium alloys to steel

Various joining methods are reported in joining dissimilar materials: mechanical, fusion, and solid-state (Martinsen et al., 2015). Bolted joints, fasteners, rivets, clinching,

and self-piercing rivets are mechanical joining processes. Magnesium alloy and steel have been joined using fusion welding techniques like resistance spot welding, laser welding, laser brazing, and laser/tungsten inert gas. Among solid-state joining techniques, friction stir welding and ultrasonic spot welding have been used. Various joining methods for Mg and steel are schematically shown in Figure 2.3.

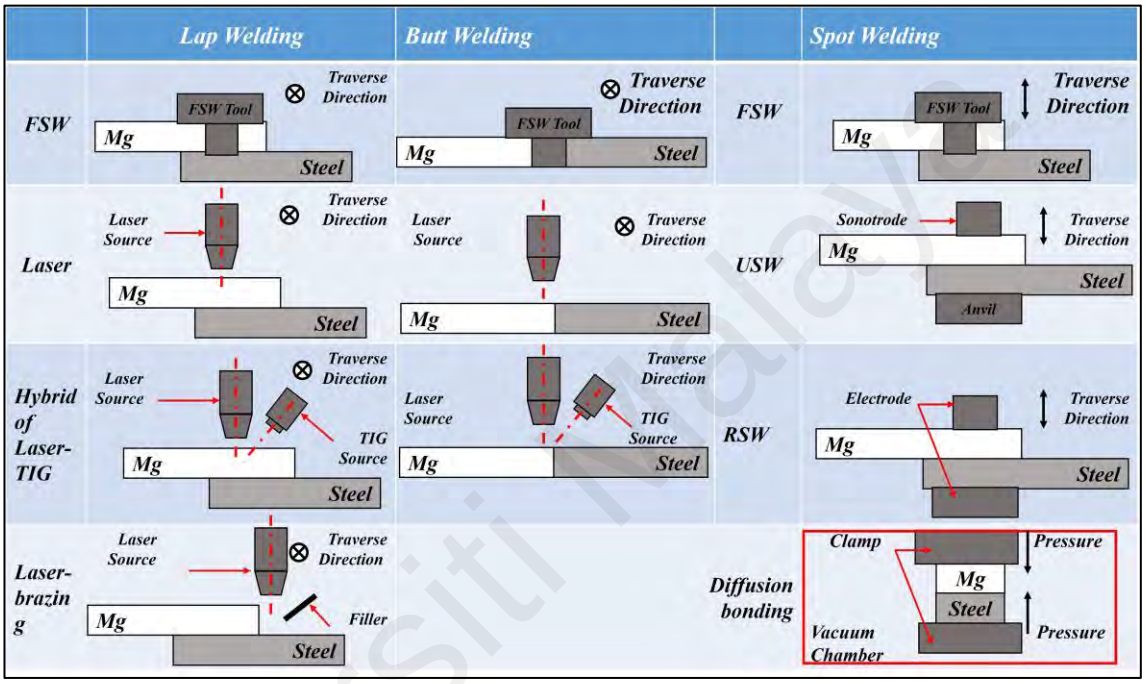


**Figure 2.3: Schematic of joining techniques used to join Mg and steel**

### 2.2.1 Mechanical joining (MJ)

Mechanical connection typically uses forces generated by mechanical interlock and interference between pieces. Materials can be joined by mechanical fasteners or inherent mechanical linkage. Mechanical fasteners include bolts, screws, rivets, pins etc. By making Knurled surface on the interface, mechanical bonding could be improved using increased surface friction. The mismatch in mechanical characteristics and poorer creep resistance of Mg alloys than steels induce stress relaxation when mechanically joined. This relaxation in stress might generate excessive strain, resulting in fastener mechanism failure (Messler, 2004).

Only if appropriate measures are taken do fasteners usually loosen with vibration. This action of vibration causes fasteners to lose force progressively. Then the force loosening process continues rapidly, causing the bolt, nut, and screw to be lost. Since various alloys have varying degrees of reactivity, distinct corrosion forms occur when an electrolytic solution penetrates the loosened gap between the mechanically joined surfaces. A joint's rigidity can be reduced due to pitting, galvanic and crevice corrosion (Messler, 2004).

### 2.2.2 Fusion welding (FW)

Fusion welding joins material surfaces by melting and solidifying them. A filler can be employed to enhance the joint properties and accommodate for variances in the workpiece materials composition. The major fusion welding technique usually employed to join Mg alloy and steel is discussed in subsequent sections.

#### 2.2.2.1 Laser beam welding (LBW)

Laser beam welding employs a beam of the laser without filler materials. The laser beam melts magnesium alloy, which reaches into a molten state and distributes over the steel surface (Ciao et al., 2010; Jiang et al., 2014; Ma et al., 2010). In another arrangement laser beam focused on the tip of the steel, the workpiece melted the magnesium alloy via heat conduction, generating a brazed joint (Casalino et al., 2017).

Researchers studied laser beam welding AZ31 alloy to Q235 steel joints. The AZ31 melted while steel melting was kept under restriction. As demonstrated in Figure 2.4, the molten AZ31 created a welding joint as a filler metal (Ciao et al., 2010; Miao et al., 2014, 2010).

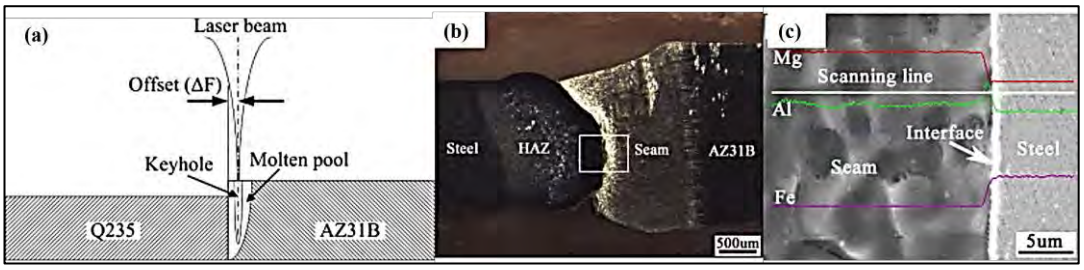


**Figure 2.4: Laser beam welding (a) schematic diagram (b) weld cross-section (c) elemental distribution at the interface** (Miao et al., 2010)

IMCs were formed for a significant metallurgical reaction at the faying surface. The Al-rich IMCs $Mg_{17}Al_{12}$, $Mg_2Al_3$, FeAl, and $Fe_4Al_{13}$ were formed. The distributions of elements changed significantly at the interface in the top section of the joint, attributed to steel dissolving, as shown in figure 2.3 (c). The tensile strength of joints was found to be 185 MPa at 0.6 mm laser offset, while fracture occurred at the interface. In a similar study, for joining Mg alloy with stainless steel, the researcher used the laser welding-brazing technique. At 0.2 mm laser offset to the AZ31 side, the highest joint strength was achieved, which was 89.8% of base AZ31.T the IMC at an interface might be made up of $Mg_{17}Al_{12}$ and $Mg_2Ni$, as the steel side fractured surface identified two IMC (Jiang et al., 2014).

As shown in Figure 2.5, researchers applied a laser offset to the sides to join with Mg alloy without applying any interlayer. With a laser offset of 0.3 mm and 0.4 mm process condition, the joints could be formed, but not in the 0.5 mm offset condition. The tensile strength of the joint was around 100 MPa (Casalino et al., 2017).

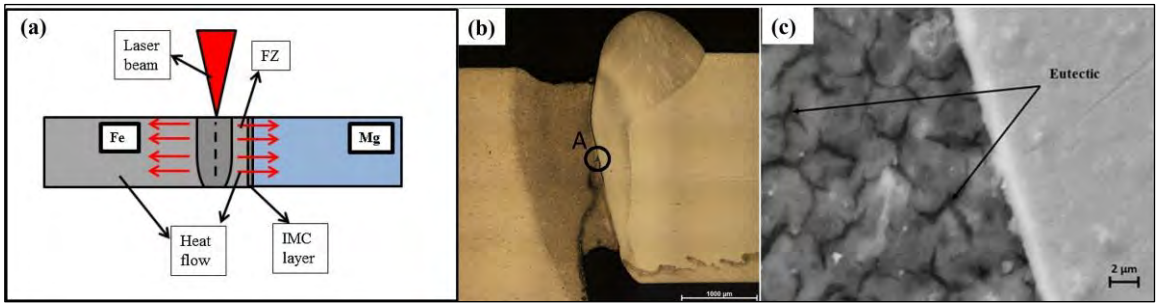


**Figure 2.5: Laser beam welding with offset (a) schematic diagram (b) joint cross-section (c) microstructure near the interface** (Casalino et al., 2017)

The interfacial reaction can be improved using LBW by applying the wire or by introducing coatings and interlayers. The interlayers of Zn (Li et al., 2013; Nasiri & Zhou, 2015; Tan et al., 2013; Wahba & Katayama, 2012), Ni (Tan et al., 2017), Al (Tan et al., 2016; Zhou et al., 2020), Sn (Hasiri & Al, 2015), AZ31 filler (Li et al., 2013; Tan et al., 2016), and AZ92 filler (Nasiri & Zhou, 2015), were used in Mg alloy and steel dissimilar welding.

The wetting properties of AZ92 as a temperature-dependent function over Ni-plated steel were investigated (Nasiri et al., 2014). Within a temperature range between 891 K - 1023 K, interactions between Mg and Ni resulted in 86º contact angle (Mode I), while $Mg_2Ni$+AlNi reactions were formed between steel and Mg joining (Mode II). Within the 1097 K to 1293 K temperature range (Mode II), 46º contact angle was recorded, as shown in Figure 2.6.

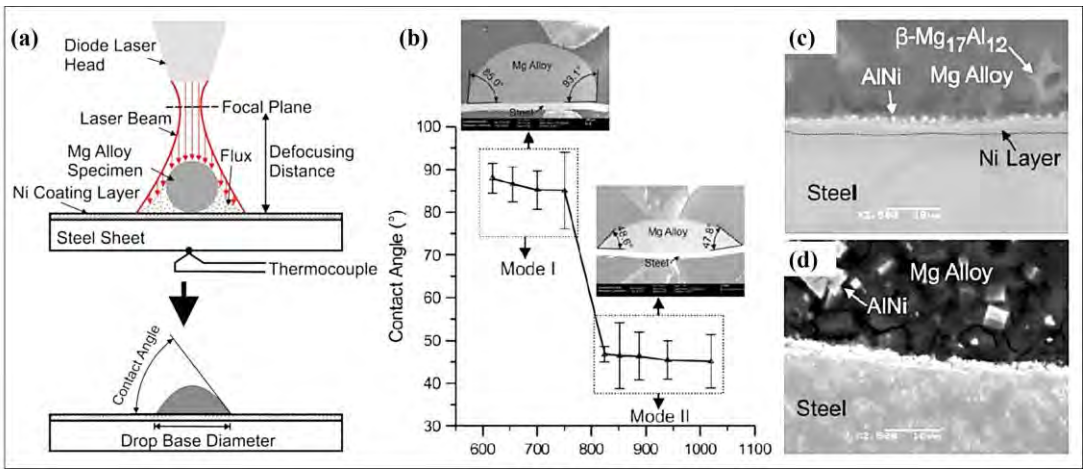


**Figure 2.6: (a) Wetting tests schematic (b) contact angle as temperature-dependent function (c,d) microstructure of interface at peak temperatures** (Nasiri et al., 2014)

Researchers experimented with laser welding of Mg alloy to nickel-coated steel workpiece and AZ92 filler. At the lower part of the joint, AlNi IMC in dendritic form and $\alpha$ −Mg+$Mg_2Ni$ are produced along the faying surfaces at the joint, whereas only an AlNi phase is formed in the top and middle of the joint, as illustrated in Figure 2.7. The joint's shear strength was measured at 96.8 MPa (Nasiri et al., 2019).

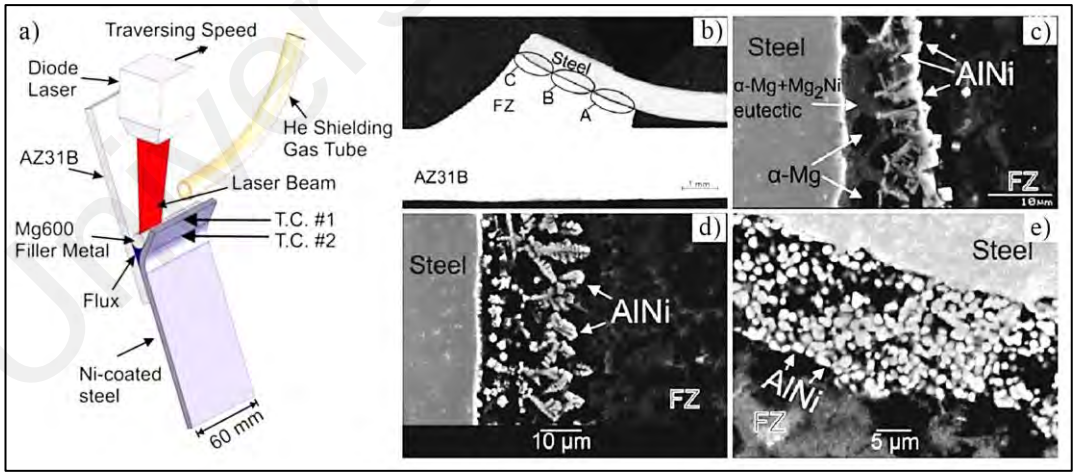


**Figure 2.7: (a) Schematic of laser beam welding of AZ31 and coated steel (b) joint cross-section (c,d,e) the SEM images of zones A, B, C at the interface** (Nasiri et al., 2019)

Researchers studied the effect of the aluminium interlayer on AZ31 and steel LBW. At the interface, metallurgical interaction at enhanced by the aluminium interlayer. When

the IMC thickness was less than 2 µm, it comprised two separate IMCs. In this case, IMC was Fe(Al) solid solution and $Al_8(Mn, Fe)_5$ at the AZ31 and steel faying surface and showed poor joint strength. On the other hand, when the IMC thickness was between 2.3 µm to 5.7 µm, the highest tensile shear strength was achieved, and IMC changed into $Al_6Fe$. An increased thickness of the aluminium interlayer led to crack development at the joint interface, as shown in Figure 2.8 (Tan et al., 2016).

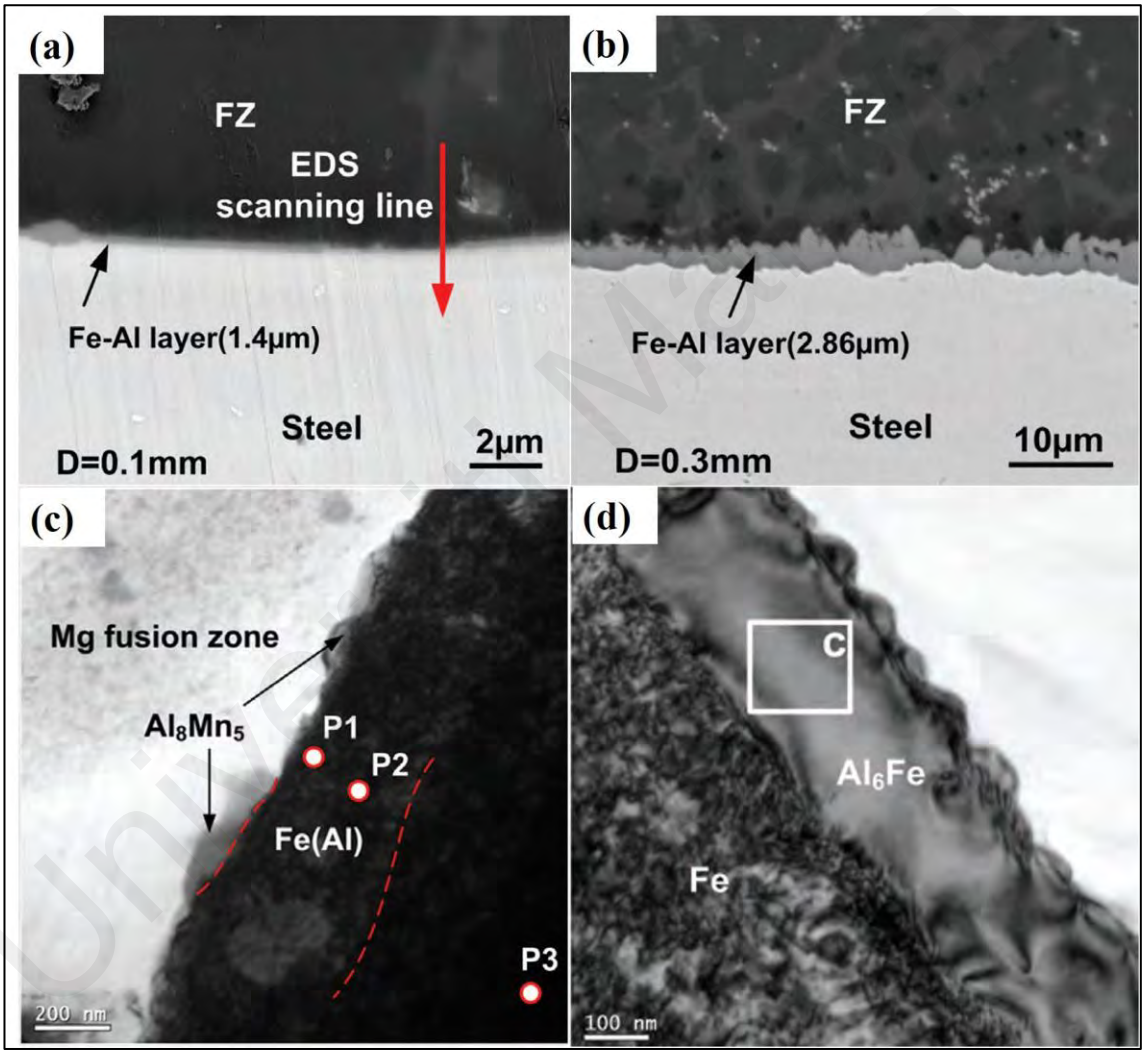


**Figure 2.8: (a,b) SEM of IMC formation with interlayer thickness variation (c) two different IMC formed in the case of 1.4 µm IMC thickness (d) formation of IMC in the case of more than 2 µm IMC thickness** (Tan et al., 2016)

#### 2.2.2.2 Cold metal transfer (CMT) welding-brazing

The cold metal transfer (CMT) welding technique is a modified version of gas metal arc metal inert gas (MIG) welding and metal active gas (MAG) welding. CMT welding

of Mg alloy to steel using copper as an interlayer has experimented, as illustrated in Figure 2.9. At the AZ31 and steel interface, two distinct joining mechanisms are experienced. At the nugget zone, IMC of $Al_3Cu_4Fe_3$ and $Fe_4Cu_3$ formed. The copper interlayer acted as a bridging agent, allowing AZ31 to be welded to steel and driving a metallurgical action at the interface (Ren & Liu, 2017).

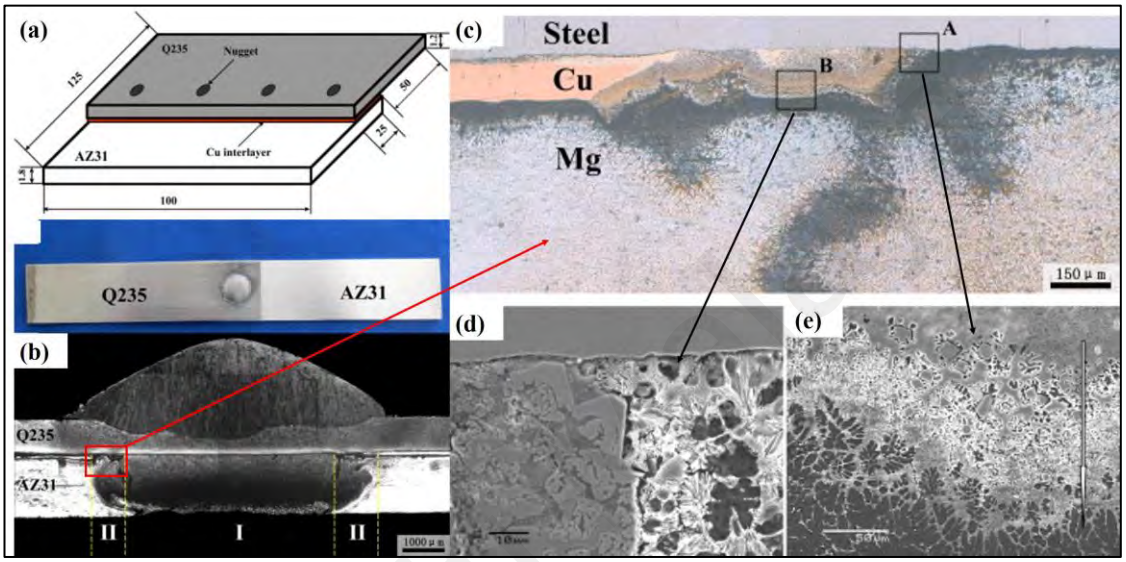


**Figure 2.9: (a) Welding arrangement with Cu interlayer (b) nugget zone macrograph and cross-section (c) SEM image of nugget edge (d,e) magnifying view of two different locations in nugget edge** (Ren & Liu, 2017)

In addition, the CMT welding technique was used to join AZ31 and galvanised mild steel, with Zn coating at mild steel being essential to a strong joint. The AZ31 and galvanized mild steel joint interface's wettability was better than the AZ31 and mild steel joint (Cao et al., 2018, 2016).

Researchers experimented with the joint characteristics of Mg alloy and steel using four different interlayer materials. Figure 2.10 demonstrated that different interlayer, which is in the form of a coating on the surface of the steel, shows specific wettability of magnesium with steel. Wettability was also affected by wire feed. Welding with galvanized iron (GI) and aluminized iron shows better wettability than welding with the other two types of the coated material. However, Mg alloy and cold rolled bare (CR) steel

joints show the highest joint strength. The Mg-Zn-Al IMC was often observed at the interface of Mg alloy- galvanized iron joints, limiting joint performance improvement. Because of the poor interfacial bonding between the Mg-Zn, the IMC consisted of the Mg-Zn had limited joining strength. Aside from the type of interlayer, the thickness of the interlayer had a significant impact on the mechanical characteristics (Kang et al., 2018).

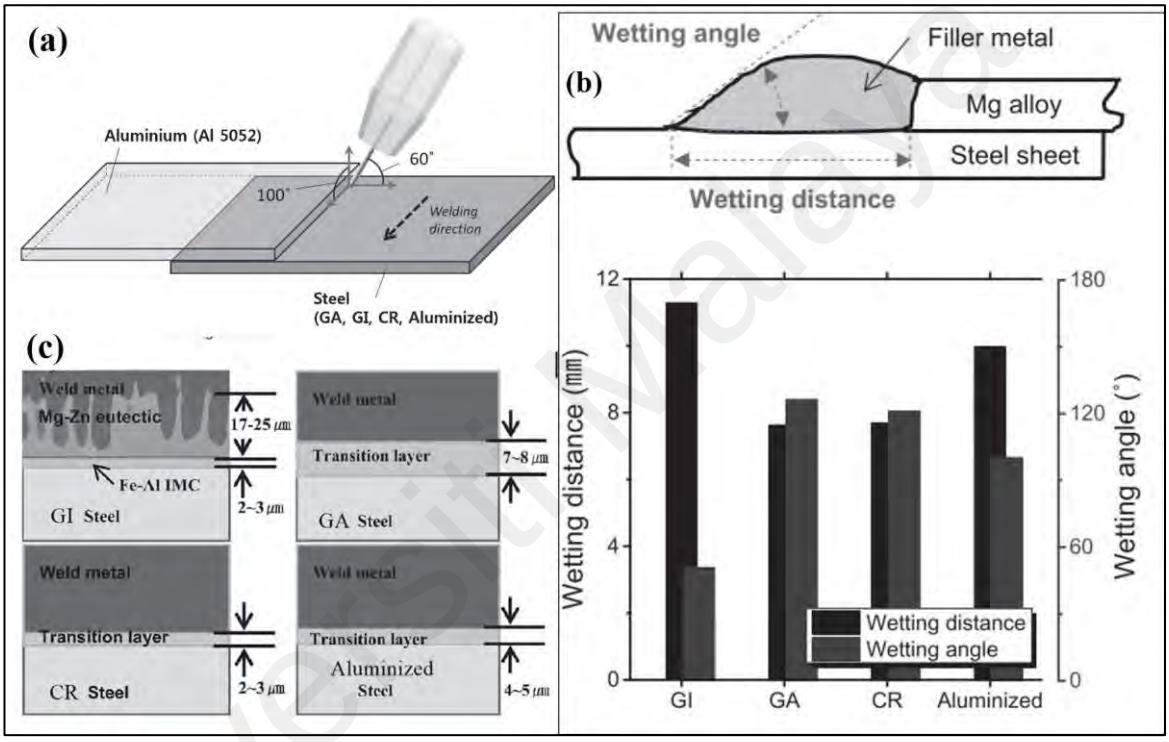


**Figure 2.10: (a) Lap CMT welding of AZ31 and steel schematic diagram (b) wetting angle measurement with a different coating material (c) microstructural view of the transition layer** (Kang et al., 2018)

### 2.2.2.3 Hybrid welding technique

Figure 2.11 shows the tungsten inert gas (TIG) and metal inert gas (MIG) hybrid welding of Mg alloy to steel using Cu interlayer (Ding et al., 2018). The joint cross-section comprises three distinct zones: partial melting zone, complete melting zone and remaining zone. The highest strength of AZ31 and steel joint was 57 MPa and 84 MPa, respectively, using 0.02 mm and 0.1 mm Cu interlayers, which means tensile strength increased by 47%.

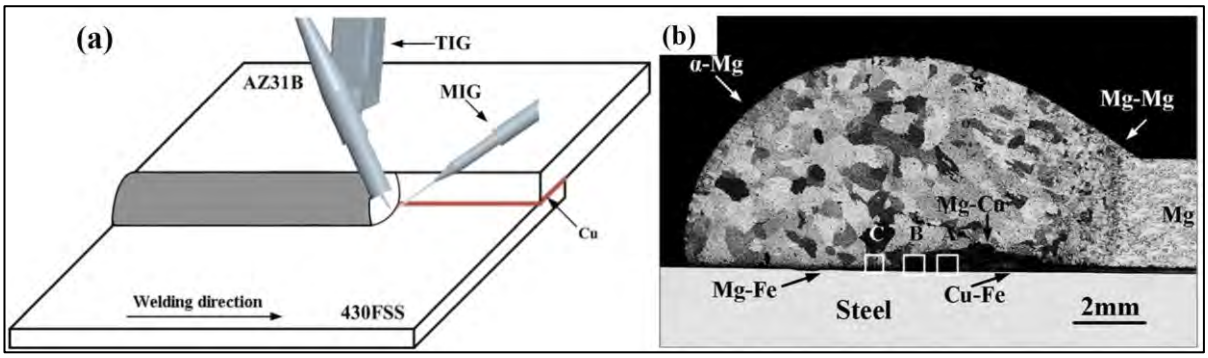


**Figure 2.11: (a) Schematic of hybrid welding using interlayer (b) joint cross-sectional view with 0.1 mm thickness interlayer** (Ding et al., 2018)

In another study, the laser-TIG hybrid welding technique effectively joined Mg alloys and Zn coated steel, Figure 2.12. The coating of the Zn layer might inhibit oxide formation at Mg and steel faying surfaces. The $Al_6Mn$ IMC is developed next to the $Fe_3Al$ IMC (Tan et al., 2017). With laser power of 1800 W, the highest tensile strength achieved was 68 MPa.

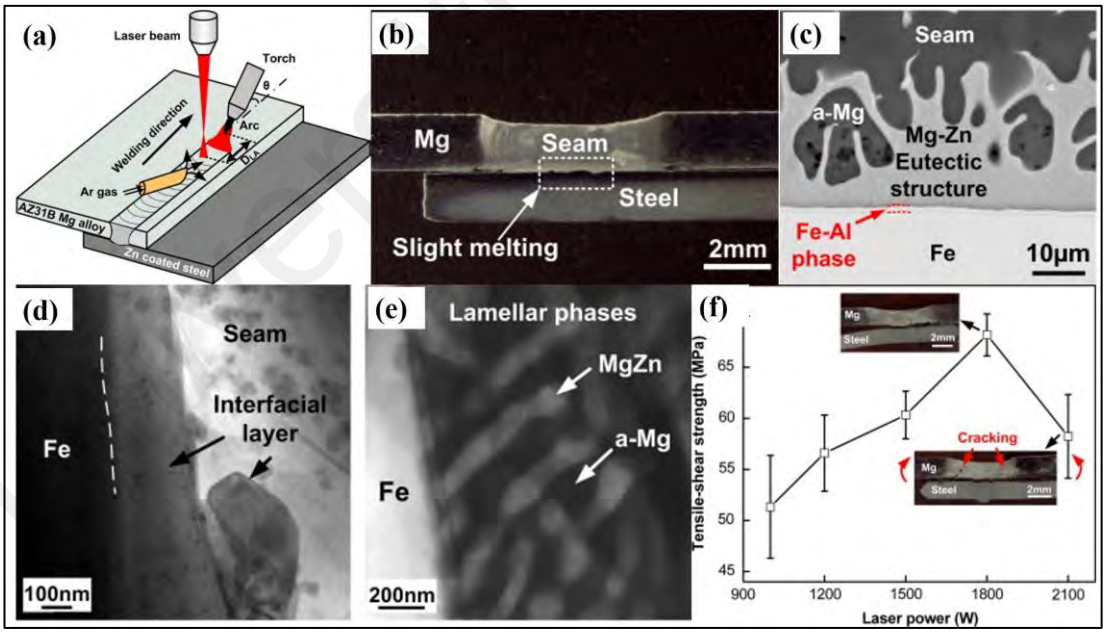


**Figure 2.12: (a) Schematic of laser-TIG hybrid welding technique (b) cross-sectional view (c) SEM image at 1200 W (d,e) TEM images indicating IMCs (f) tensile-shear strength at different laser power** (Tan et al., 2017)

Joining was carried out with laser-TIG hybrid welding using different interlayers such as Cu, Ni and Zn-Cu to eliminate the formation of oxides at the Mg alloy and steel

interface. The strength of a welded joint with an interlayer was higher than that of a joint without an interlayer one. The concept of interlayer choices should promote wettability while preventing the significant development of brittle IMC at the joint interface. Figure 2.13 depicts various joints formed by interlayers. Adjacent to the steel side, Ni-Fe solid solutions were developed, and IMC $Mg_2Ni$ IMC was formed adjacent to the Mg side using a Ni interlayer. In Cu interlayer addition joint, rod-like $Mg_2Cu$ IMC was reported by the researcher. The magnesium side interface depicts a dendritic shape $Mg_2Sn$ IMC while joining with the Sn interlayer (Liu et al., 2016).

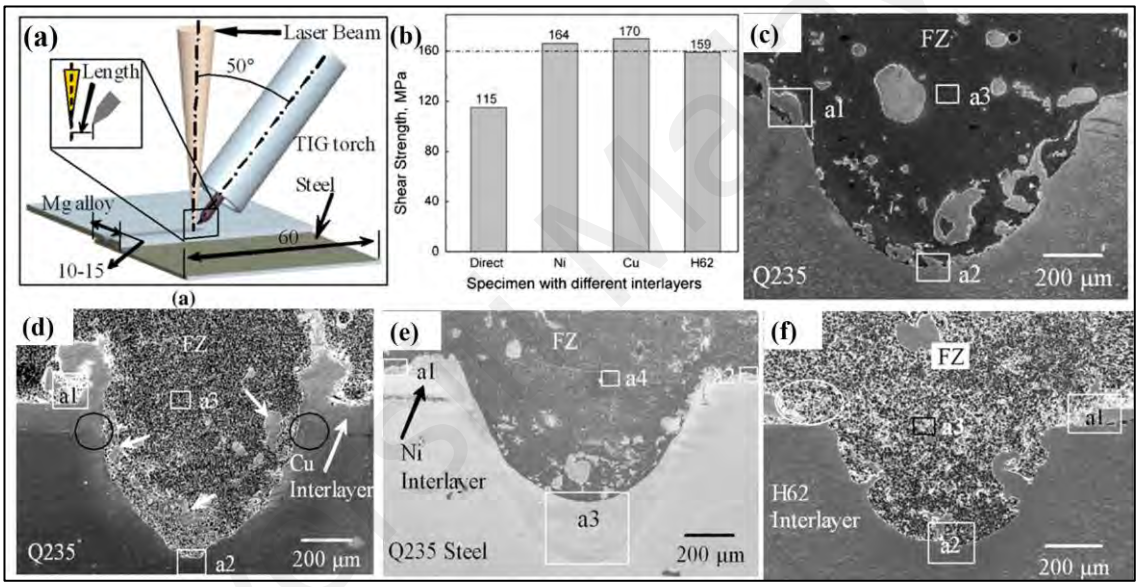


**Figure 2.13: (a) Schematic arrangement of hybrid welding (b) shear strength with different interlayer (c-f) microstructure of joints with no interlayer, Cu interlayer, Ni interlayer and Zn-Cu interlayer** (Liu et al., 2016)

The Nickel interlayer was used to join AZ31 alloy and steel in butt configuration with variable plate thickness, as shown in Figure 2.14 (Song et al., 2018). To melt down the nickel interlayer, which needed more significant heat input than other types of the interlayer, laser-TIG double-side hybrid welding was used. The fusion zone yielded fine particles of AlNi distributed uniformly, which sought to increase weld strength. A 0.1 mm offset towards steel gave 232 MPa tensile strength. Al-Mg, Ni-Mn-Fe IMC with 150

nm thickness and Fe-Ni IMC with a thickness of 60–500 μm were found between the weldment and the base steel.

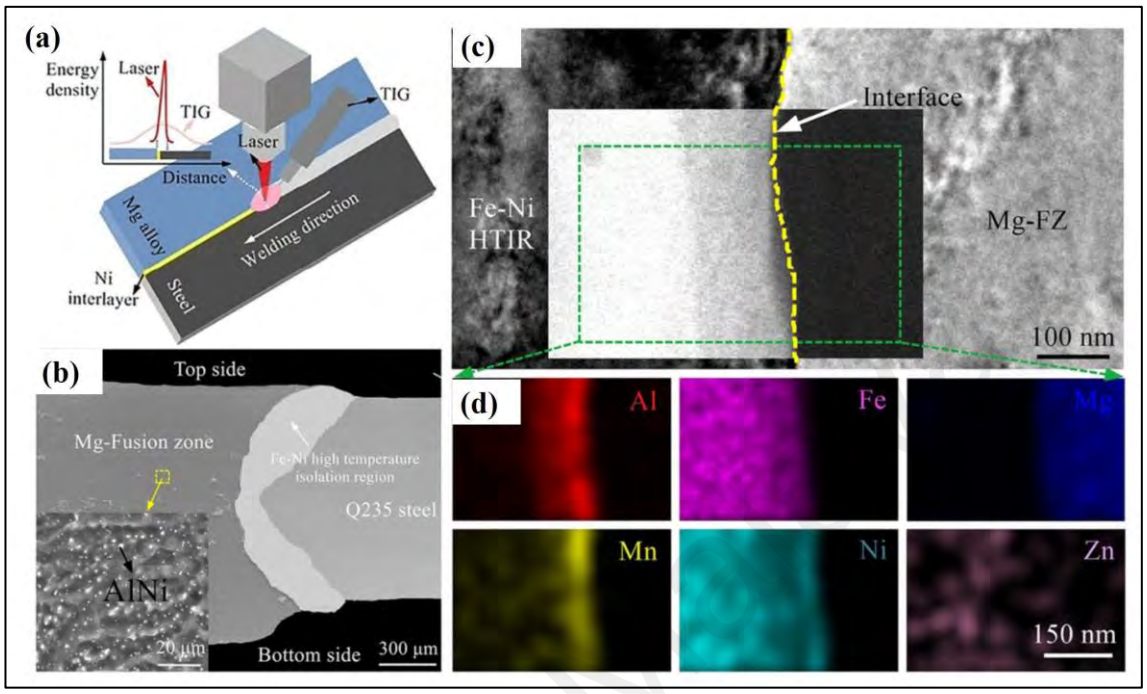


**Figure 2.14: (a) Double-side Laser-TIG hybrid welding (b) joint cross-sectional view (c) HR-TEM image near interface (d) TEM-EDS mapping from zone marked in (c)** (Song et al., 2018)

Laser-TIG hybrid welding of Mg alloy and steel in butt configuration was performed with AZ61 filler. As seen in Figure 2.15, an IMC rich in Al and Mn elements forms at the joint interface. The characteristics and fracture behaviour of the joint were influenced by the microstructural features of the Mg alloy and steel interface and the IMC thickness (Song et al., 2018).

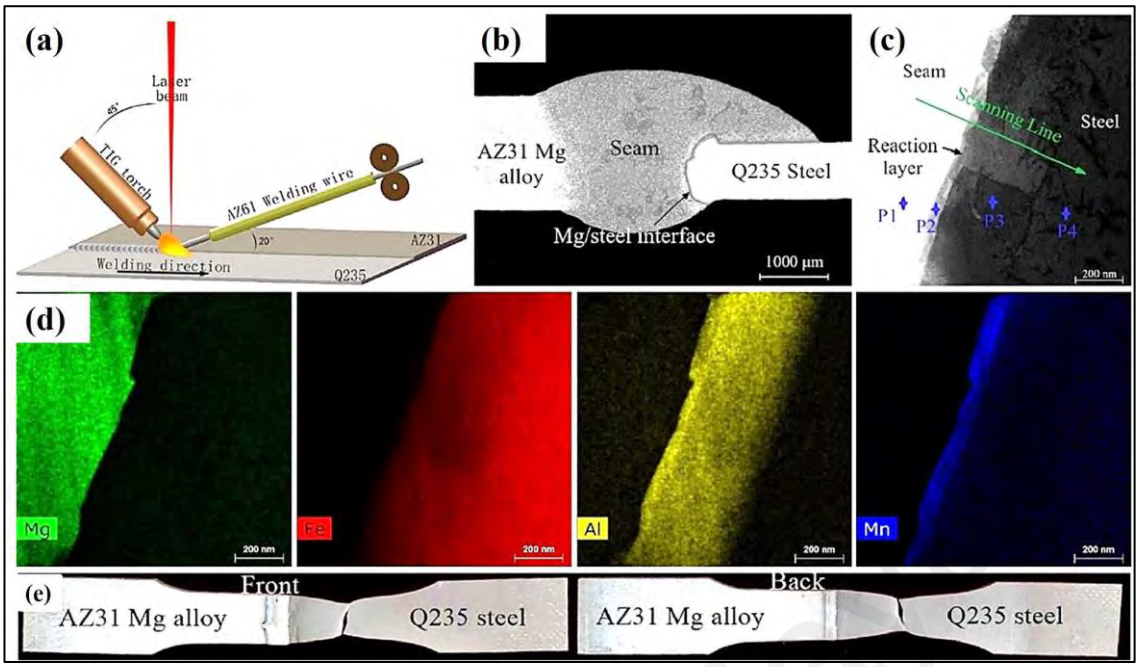


**Figure 2.15: (a) Schematic of welding arrangement with AZ61 filler (b) cross-sectional view of joint (c) STEM imaging at interface depicting scheme for elemental mapping (d) TEM-EDS mapping at the interface (e) fractured specimen** (Song et al., 2018)

#### 2.2.2.4 Resistance spot welding (RSW)

A joint is formed in RSW under a specific current and pressure. The materials are fused when resistive heat is produced and transferred to the workpieces. RSW successfully joined AZ31B and steel workpiece, as presented in Figure 2.16. researchers found that a $Fe_2Al_5$ coated interlayer with nanoscale thickness attached well enough with steel and magnesium lattices might be assisted in obtaining a good joint. Furthermore, they discovered that an IMC was not the only indicator of good magnesium and steel joint. The weld shear strength of an AZ31 and steel joint with a $Fe_3Al$ IMC was more potent than that of a pure magnesium and steel joint (Lei et al., 2017; Liu et al., 2018).

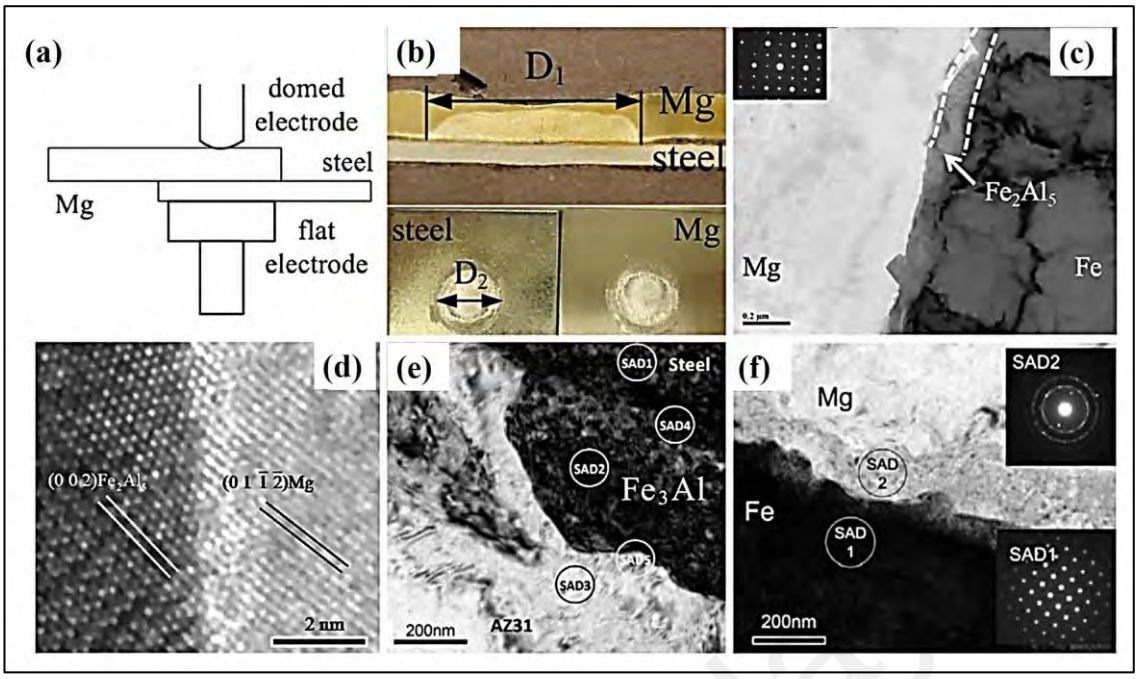


**Figure 2.16: (a) Schematic representation of RSW (b) weld-cross sectional and fractured surface macrograph (c) $Fe_2Al_5$ IMC at interface (d) lattice space of $Fe_2Al_5$ and Mg side (e) $Fe_3Al$ IMC formation (f) SAED in inset** (Lei et al., 2017; Liu et al., 2018)

Resistance element welding (REW) was also used to join magnesium and steel materials. Only one nugget appeared in the AZ31 alloy that exhibited a welding-brazing nature for the Mg alloy and steel bond, as illustrated in Figure 2.17 (a). As shown in Figure 2.17 (b), two nuggets were developed during REW: one near the steel rivet and steel workpiece contact and another near the magnesium and steel rivet in the magnesium alloy. The REW joints had a shear strength of 3.71 kN, which was greater than the RSW, which exhibited 2.23 kN (Manladan et al., 2017).

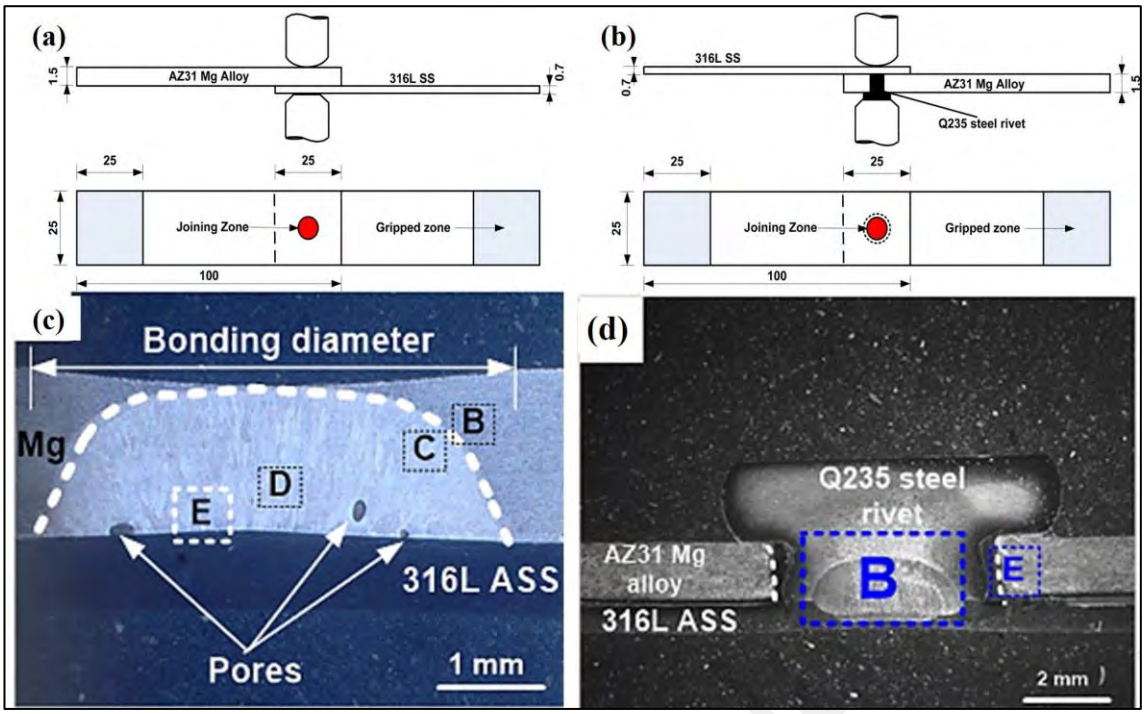


**Figure 2.17: (a) Schematic illustration of conventional RSW (b) Schematic illustration of REW (c,d) cross-sectional view of RSW and REW with B,C,D,E denotes different location of welding cross-sections** (Manladan et al., 2017)

In another experimental work, RSW was effectively used to join magnesium alloy and galvanised steel. It can be observed from Figure 2.18 that the fatigue behaviour of the magnesium/steel joint was nearly identical to that of magnesium similar joint (Liu et al., 2017).

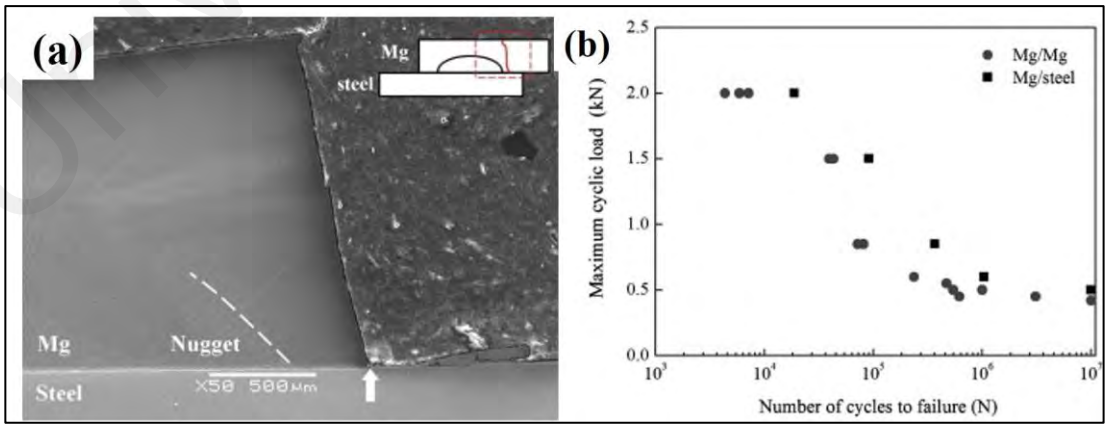


**Figure 2.18: (a) Fatigue fractured surface at maximum load (b) fatigue characteristic** (Liu et al., 2017)

### 2.2.3 Solid-state joining

#### 2.2.3.1 Diffusion bonding

Diffusion bonding is a solid-state joining method for similar, dissimilar, and immiscible materials such as magnesium and steel. The lap joint configuration is commonly used in magnesium and steel diffusion welding. The process consists of sealing the work material at an elevated temperature and pressure for an extended period to achieve diffusion at the atomic level in the material. The approach of introducing interlayers can be employed to develop a sound bonding of dissimilar materials with limited solubility in each other. The feature of this joining procedure is that the joining temperature is minimal, allowing materials to be joined without affecting the base materials' characteristics. Because of their metallurgical affinity with magnesium and iron, nickel and copper was chosen as the significant interlayer to bond magnesium alloy and steel.

The microstructural characterisation of diffusion bonded stainless steel to AZ31 was examined using a Ni interlayer. Figure 2.19 depicts the influence of bonding periods on joint microstructural development. A strength of 46 MPa was attained at 510°C with a 20-minute bonding period which was the highest among all bonding periods. The double-stage diffusion bonding of steel and AZ31 was used to enhance the bonding strength further. Due to the Ni interlayer with the double-stage bonding method, the joint strength improved to 54 MPa (Elthalabawy & Khan, 2015b).

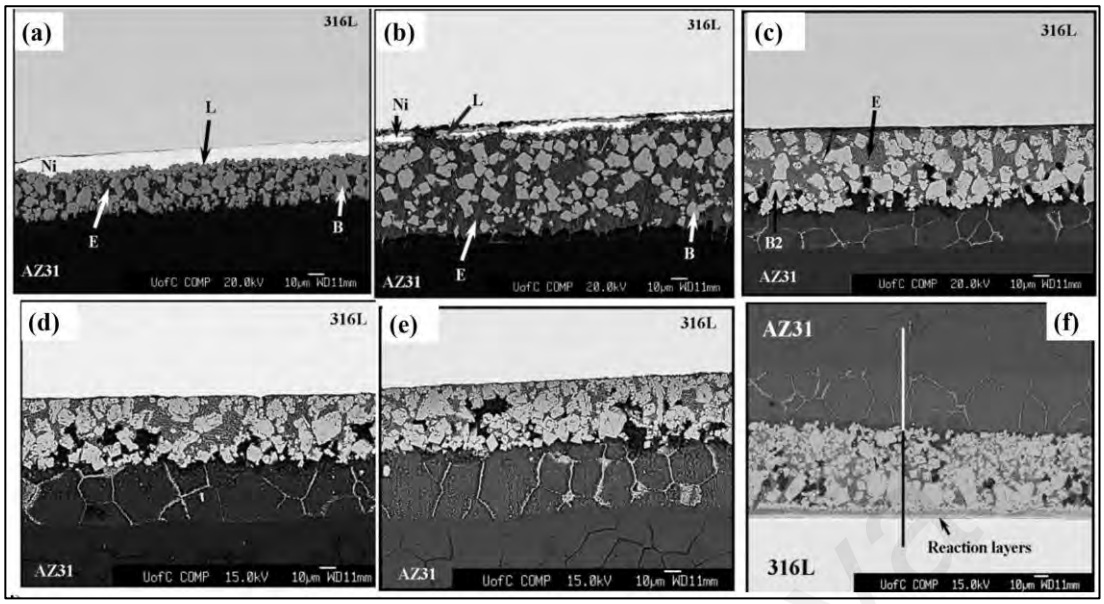


**Figure 2.19: SEM images of joint at 510 °C with various bonding periods (a) 3 minutes (b) 5 minutes (c) 10 minutes (d) 20 minutes (e) 30 minutes (f) double-stage diffusion bonding with 20 minutes** (Elthalabawy & Khan, 2015b)

Diffusion bonding was used to investigate the properties of magnesium alloy and steel joint with a copper interlayer. The bonding time effect at 530 °C temperature was investigated in terms of bonding strength. At 530°C and 20 minutes, the highest strength of 57 MPa was achieved, Figure 2.20 (Elthalabawy & Khan, 2015a).

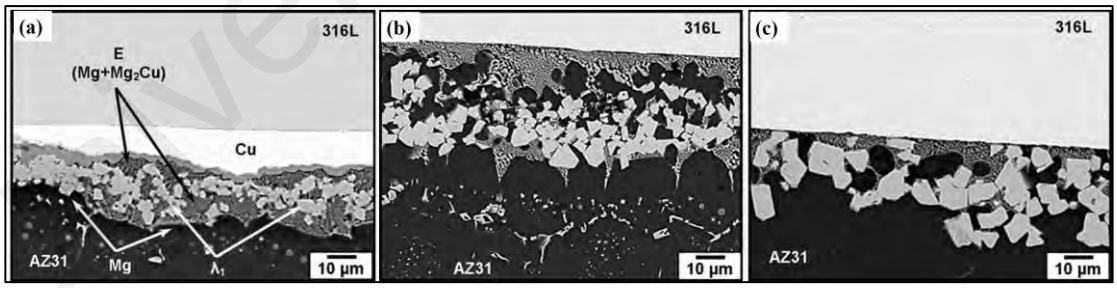


**Figure 2.20: SEM images of joint at 510 °C with various bonding periods (a) 5 minutes (b) 15 minutes (c) 30 minutes** (Elthalabawy & Khan, 2015a)

### 2.2.3.2 Ultrasonic spot welding (USW)

Figure 2.21 depicts the impact of various coatings on the joint characteristics of ultrasonic spot-welded magnesium and steel. The bonding strength of USWed magnesium alloy to steel without any interlayer was found to be low. The IMC for magnesium alloy with steel using an Sn interlayer joint was made up of $Mg_2Sn$. $Mg_7Zn_3$ and $Mg_2Zn_{11}$ IMCs were found in the magnesium alloy and zinc-coated steel joint interface. Magnesium alloy and Sn-coated steel joint strength were found to be maximum compared to other welding conditions (Patel et al., 2015).

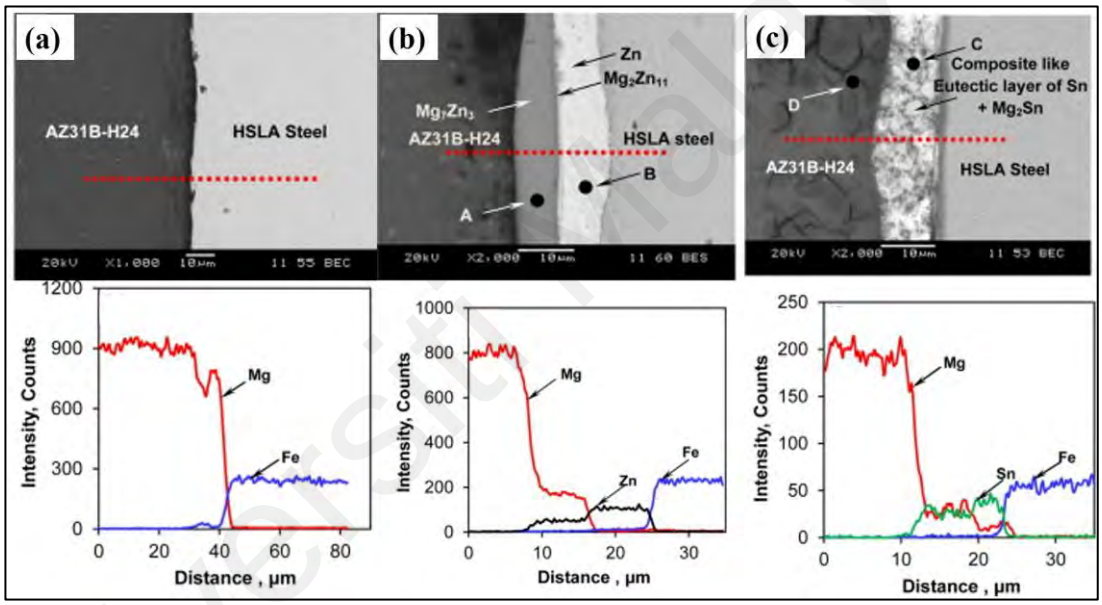


**Figure 2.21: SEM images of AZ31 and steel joint (a) without interlayer (b) Zinc interlayer (c) Sn interlayer** (Patel et al., 2015)

## 2.3 Friction stir welding (FSW) - an innovative solid-state welding technique for immiscible magnesium alloy and steel

### 2.3.1 Fundamentals of FSW

Friction Stir Welding (FSW), which is considered a solid-state welding process, was invented at "The Welding Institute Ltd." in the United Kingdom and was initially applied to aluminium alloys. In FSW, a non-consumable rotating tool generates frictional heat between the tool and the workpiece material, which induces severe plastic

deformation of the metal interface, resulting in mixing the workpiece materials welding path with many advantages over conventional joining methods for producing joint (Lohwasser & Chen, 2010; Yi et al., 2016). The basic schematic of the FSW process is shown in Figure 2.22 (Mishra & Ma, 2005a).

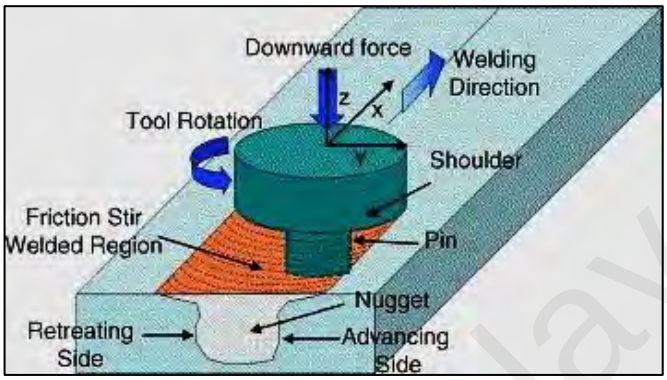


**Figure 2.22: Basic schematic of the friction stir welding process** (Mishra & Ma, 2005b)

As shown in Figure 2.23, the joint of FSW is divided into three distinct zones: (a) the stirred zone (SZ) or nugget zone at which severe plastic deformation takes place, (b) the thermo-mechanically affected zone (TMAZ), which is found between heat-affected zone and stirred zone, and (c) heat-affected zone (HAZ), which experienced thermal cycle because of welding process (Lohwasser & Chen, 2010; Wang et al., 2015; Weng et al., 2020; Zolghadr et al., 2019). Heat due to friction and plastic deformation in SZ leads to fine recrystallised microstructure, while TMAZ shows elongated grains (Imam et al., 2017; Zolghadr et al., 2019).

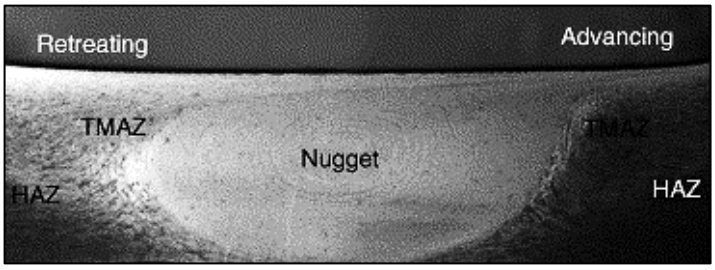


**Figure 2.23: Macrograph of the weld zone** (Raja et al., 2020)

After this, the area of FSW research broadened, and their excellent performance either in the joining of similar material or dissimilar material was documented (Ahmad et al., 2019; Buchibabu et al., 2017; Imam et al., 2017; Küçükömeroğlu et al., 2018; Patterson et al., 2016) and successfully used in various industries, including railway, automobile, defence, aerospace and renewable energy, as shown in Figure 2.24 (Magalhães et al., 2018; Meng et al., 2021).


**Figure 2.24: Application of FSW in various industries** (Meng et al., 2021)

### 2.3.2 FSW affected zones

In order to better describe the microstructure that forms after the FSW process, The Welding Institute has developed schemes that divide the cross-section into various areas based on how heat affects them. The scheme is accepted by the Friction Stir Welding Licensees Association (Sattari et al., 2012). Figure 2.25 below shows the four zones.

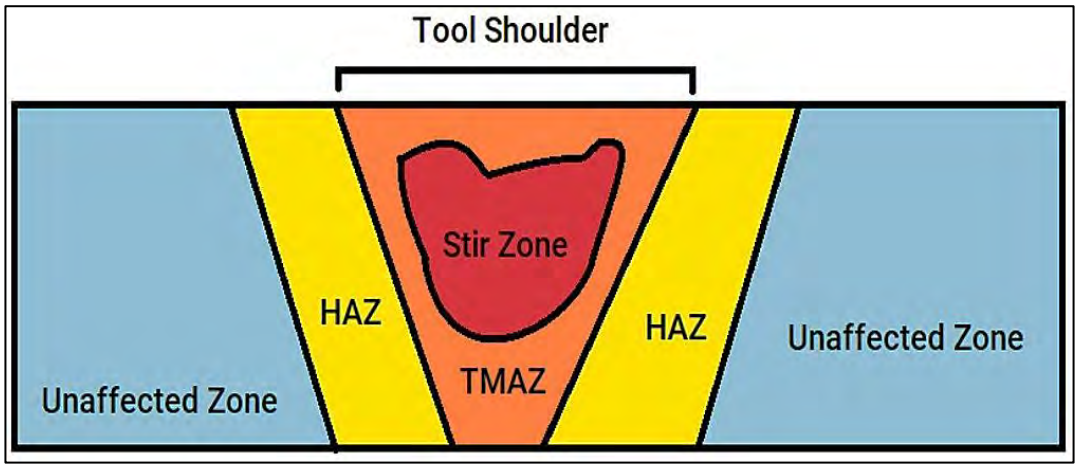


**Figure 2.25: FSW weld zones**

i. **Unaffected Zone:** This region is furthest from the weld centre and is not affected by the generated heat and thermal cycle. The mechanical property remains unchanged from the base/parent material in these regions.

ii. **Heat Affected Zone (HAZ):** Closer to the weld zone, this region experiences a thermal cycle, and the mechanical properties are altered. However, it does not experience any plastic deformation.

iii. **Thermo Mechanically Affected Zone (TMAZ):** In this region, the material experiences plastic deformation and its mechanical properties and microstructure change.

iv. **Stir Zone:** This part of the TMAZ experiences recrystallisation and the grain size that forms is said to be ten times smaller than that of the base material (McClure, 1998).

### 2.3.3 FSW of magnesium alloy and steel

As discussed in 2.1, the joining is complex due to the large miscibility gap between Mg and steel, lacking essential IMC formation. However, joining Mg alloy and steel can be possible by using alloying elements of base Mg alloy and steel to make IMC (Fu et al., 2022; Thomas et al., 2022). But this affects the base material properties. One possible solution is applying an interlayer, which is miscible with Mg and Fe between workpieces.

The Zn metal particle as a reinforcing agent is vital in achieving successful FSWed joints in most Mg/steel (Chen et al., 2015; Liu et al., 2017; Shen et al., 2016a; Xu et al., 2018). Zn coating is used to eliminate the oxide layer and pinch the new Zn phase to the surface, enhancing the weldability of Mg/steel. AM60 magnesium alloy with galvanised DP600 steel friction stir spot welding (FSSW) joints with a maximum shear load of 2.9 kN was obtained by optimising the welding parameters to achieve improved Mg/steel FSW joints (Liyanage et al., 2009). The Zn-coated DP600 steel and ZEK100 magnesium alloy were welded using refill FSSW, achieving a shear load of 4.7 kN (Chen et al., 2015). The joints between AZ31B and galvanised mild steel were welded using friction stir keyhole spot welding to achieve a maximum strength of 8.7 kN (Zhang et al., 2014).

Figure 2.26 depicts a typical FSLW between AZ31 and steel with the mechanical interlocking of steel fragments into the magnesium side (Jana et al., 2015).

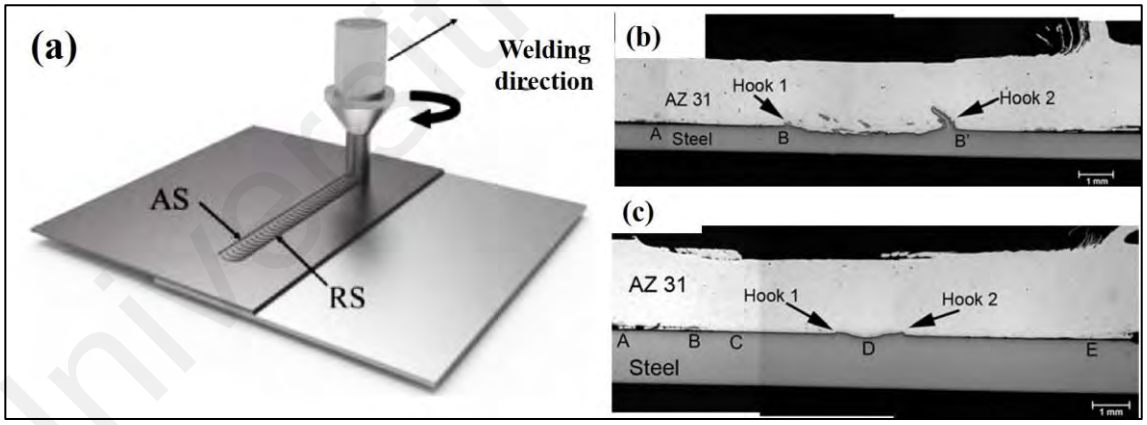


**Figure 2.26: (a) Schematic of FSLW between Mg/Steel (b,c) cross-sectional view of mechanical interlocking** (Jana et al., 2015)

The Friction-stir Assisted Scribe Technique (FAST) employs a regular FSW tool with a sharp scribe offsetting the welding tool probe, as shown in Figure 2.27. The scribe's hooks mechanically interlocked magnesium alloy and steel, which appears in enhanced strength. The joint interface consists of the eutectic layer of Mg-Zn with the FAST welding technique between Mg alloy and steel (Wang et al., 2020).

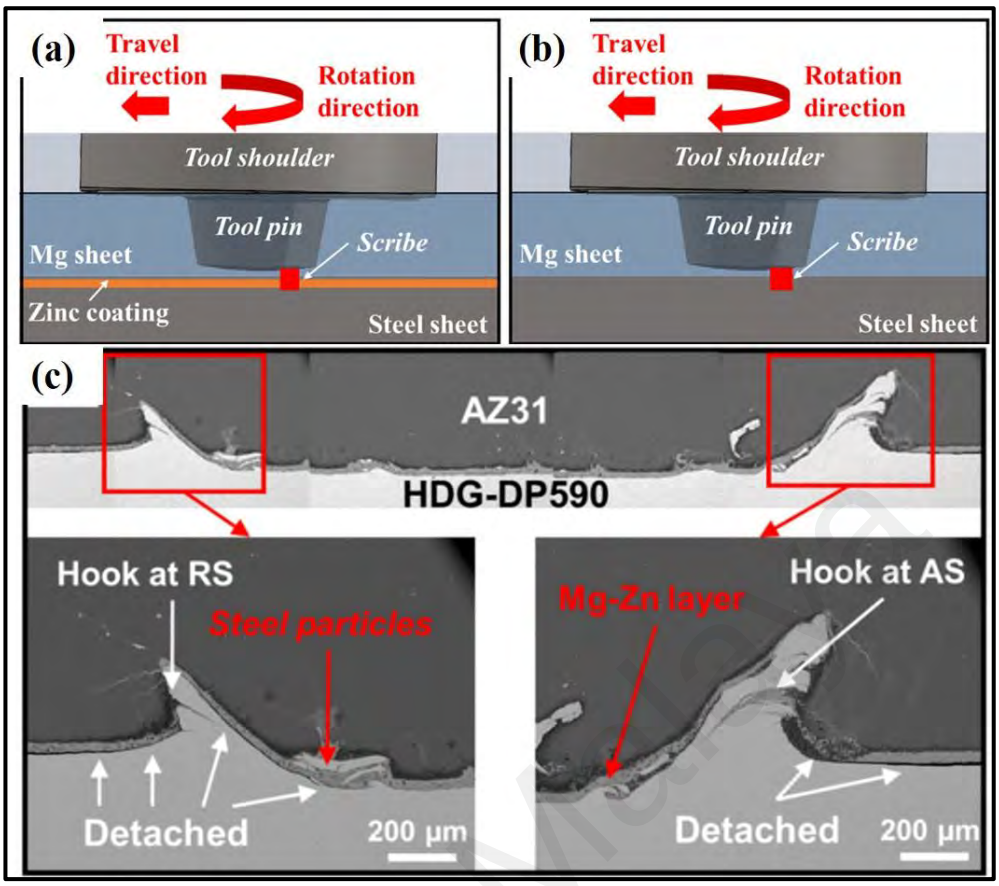


**Figure 2.27: (a) Schematic diagram of FAST with Zn-coating (b) schematic diagram of FAST without coating (c) mechanical interlocking and IMC formation at the interface** (Wang et al., 2020)

FSW procedure was used to weld a magnesium/steel butt joint. The study reported the influence of the Al content of Mg alloys on the mechanical properties of steel/magnesium butt joints using FSW (Kasai et al., 2015a). From Figure 2.28, it is clear that the AZ61/steel butt joint exhibited the highest tensile strength. The greater the Al content (pure Mg, AZ31, and AZ61 Mg alloys), the stronger the joint's tensile strength. Al elements are critical in bonding dissimilar metals such as Mg and steel (Joo, 2013). The Fe-Al IMC ($Fe_2Al_5$) layer formed at the magnesium/steel interface and was predominantly detected in AZ series magnesium alloy/steel joints. Additionally, the thickness of the interface layer has a significant impact on the strength of joints. The thinner the interface sheet, the stronger the joint.

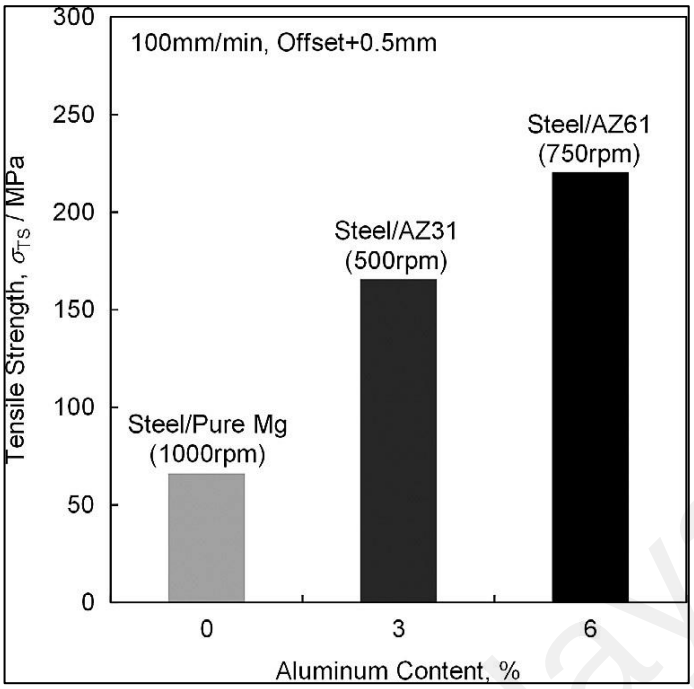


**Figure 2.28: Effect of aluminium content on strength** (Kasai et al., 2015a)

However, with joint cross-sectional surface EDS mapping and spot analysis, an Al depletion region near the interface was generated compared to the base magnesium alloy's Al content. Al in magnesium is thought to have been absorbed during the formation of the FeAl IMC (Kasai et al., 2015a). Further, Figure 2.29 illustrates STEM and mappings at the cross section's interface. Al content in Mg near the interface depleted. The aluminium reduction was severe due to the thicker IMC layer formed under the conditions of increased heat intake. This study shows that it is critical to control Al depletion and form a thin IMC at the interface to achieve strong steel/magnesium joints. From the above findings, one can conclude that by adding Al metal as reinforcement, somehow, Al content in parent material can be controlled.

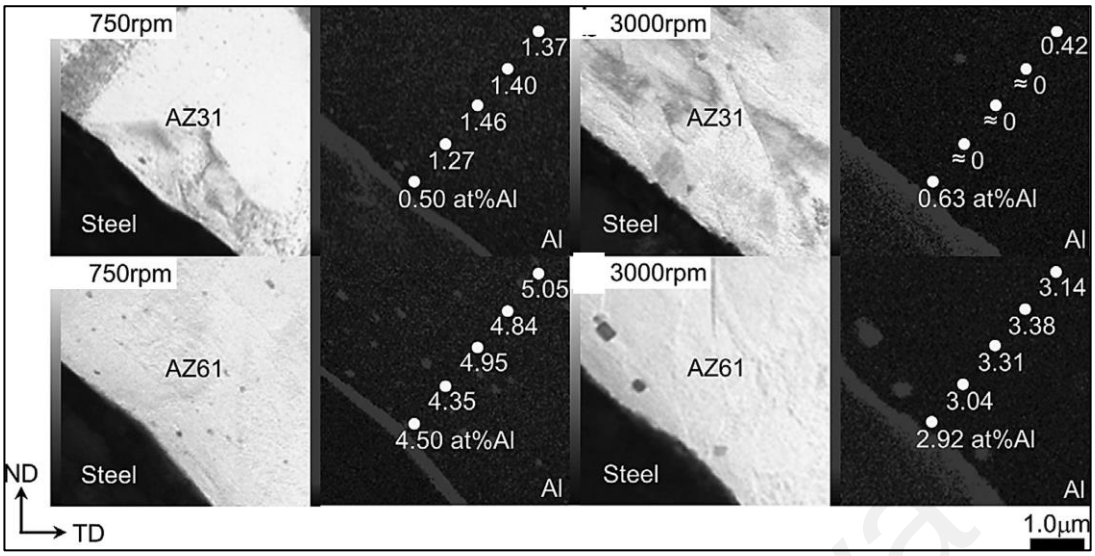


**Figure 2.29: STEM image and mappings at the cross section's interface with varying process parameters** (Kasai et al., 2015a)

In another study of FSW of Mg alloy and steel, defects are formed with different parameters. There were two modes of defect formation. Lack of fill defects occurs with low rotational speed and high tool traverse speed, whereas galling defects form when high heat input is provided during welding due to increased tool rotational speed, as shown in Figure 2.30 (Wang et al., 2019).

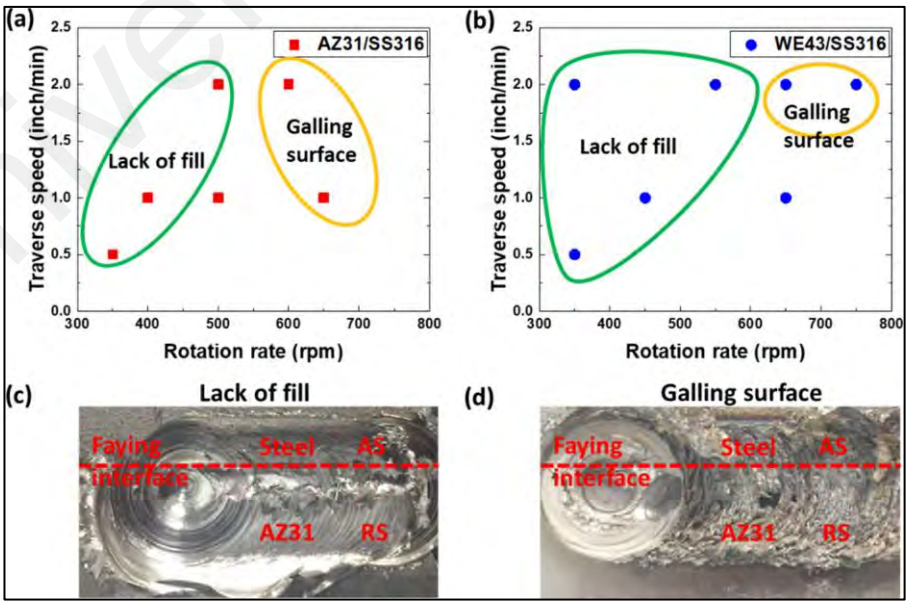


**Figure 2.30: (a) Welding parameters of AZ31 and SS316 steel (b) welding parameters of WE43 and SS316 steel (c,d) corresponding defects under varying process parameters window** (Wang et al., 2019)

Mechanical interlocking phenomena were also observed in the FSW of AZ31 and Q235 steel (Meng et al., 2021). Workpiece material was joined by a truncated cone probe. The purpose of the truncated cone was to increase stirring action for sound joint formation. The probe of the tool with a specific shape increased the flowability of steel to form steel-strip into magnesium side, as shown in Figure 2.31. Fe-Al IMC formed, which could also enhance joint properties apart from mechanical interlocking.

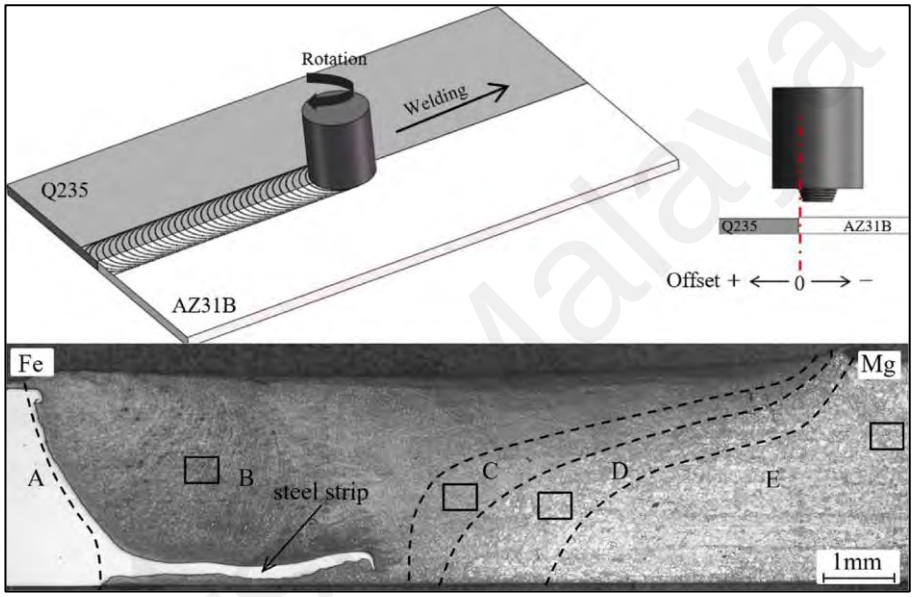


**Figure 2.31: Schematic of FSW with truncated cone shape tool and corresponding macrograph depicting steel strip into magnesium side** (Meng et al., 2021)

#### 2.3.3.1 Operating paramters of FSW of Mg and steel

The main FSW operating conditions are the tool rotational and welding speeds, the tool's tilt angle, and the tool offset. Various researchers have examined the effect of these parameters on the FSW of Steel and Mg alloys to achieve a defect-free and proper weld consistency. Table 2.2 summarises the main effects of this series of operating parameters on dissimilar FSW (Chen & Nakata, 2009; ESAB, 2009).

**Table 2.2: Major FSW operating constraint** (Chen & Nakata, 2009; ESAB, 2009)

| Parameters | Noteworthy effects |
|---|---|
| Tool rotational speed | frictional heat generator, mixing of work-material |
| Welding speed | Assist in deformed material smooth flow and heat control |
| Tool tilting angle | Extrusion and forging action |
| Offset of tool | Assist in the distribution of thermal stresses optimally for dissimilar welding |

(a) ***Effects of tool welding speed on magnesium-steel FSW process***

Tool welding speed (WS) means the rate at which welding tool advances along with workpiece material faying surface. Choosing WS is also challenging, as it directly affects the microstructural behaviour when joining magnesium alloy and steel with FSW (Ramachandran et al., 2015). Any changes in WS during FSW have an uncertain effect on joint properties (Sakthivel et al., 2009). The welding speed is typically determined by several variables, including the form of joint (e.g. butt or lap joint), the tool rotational speed, the plunging depth, and the material composition of the workpiece (Prasad et al., 2018; Shen et al., 2016b).

Any decrease in tool traverse speed while maintaining constant tool rotational speed or an increased tool rotational speed while maintaining constant tool traverse speed has the same effect on weld efficiency. Thus, it is recommended to choose the optimal traverse and rotatory speed combination to preserve the optimal heat supply, joint performance, and formation of IMCs in the FSW of Steel-Mg alloys (Alireza et al., 2017; Coelho et al., 2012; Zhang et al., 2014). During FSW, heat generation is inversely proportional to the traverse motion of the tool. The rapid tool traverse motion results in insufficient heat generation, which results in incomplete weldments. While, at a relatively

high welding speed, less heat is produced, which results in improper intermixing of weld materials and the creation of void defects (Sharma et al., 2017; Zhang et al., 2014).

Insufficient deformed material flow occurs at a higher tool linear speed, resulting in the forming of cavities such as tunnelling defects at the interface of the weld joint. By decreasing the tool traverse speed, the temperature of the weld interface increases, which leads to reduce in thermal stress, improved material flowability and reduced cavity defect formation (Kim et al., 2006; Zhang et al., 2014).

(b) ***Effects of tool rotational speed on FSW of Steel-Mg alloys***

Tool rotational speed is one of the essential decisive parameters in assessing the joint quality of weldment. When FSW of dissimilar materials is performed at a high tool rotational speed, the thermal energy generated is enormous, and the joint interface area is increased proportionately (Liyanage et al., 2009). The tool rotational speed should be optimised since lower speed results in less generation of heat and inadequate intermixing of deformed materials in Steel-Mg alloys in the FSW (Watanabe et al., 2006). If the FSW tool's rotational speed is less than 900 rpm, micro-holes will form due to a lack of heat input and insufficient material filling (Singarapu et al., 2015).

However, high tool rotational speed results in immense stirring and forging of metals. This results in a large number of metal particles (steel) fragmented from the steel plate, which is unable to distribute uniformly in the weld nugget. As a result, weak bonding and the detection of defects such as cracks and voids in the welding zone (Bisadi et al., 2013; Esmaeili et al., 2011; Schneider et al., 2011).

Thus, it is essential to select the optimum tool rotational speed in FSW of Steel-Mg alloys since both incredibly low and high rotational speeds degrade the microstructure

and mechanical properties of the weldment (Bisadi et al., 2013; Liyanage et al., 2009; Schneider et al., 2011).

(c) ***Tool tilt or inclination angle***

The tilt or inclination angle of a tool is described as the tool's relative location in relation to the workpiece surface position. Zero (0°) or no tilt angle denotes the tool's perpendicular positioning to the workpiece location (Tolephih et al., 2013). FSW of magnesium alloy and steel with a 1.5°–3° tool tilt angle produces greater strength and microstructural bonding than with no or 0° tool tilt angle. Since a higher tool tilt angle produces a greater perpendicular axial force, which facilitates the flow of steel fragments through the magnesium metal matrix, contrary to the perception that FSW with a 0° tool tilt angle results in worn-out tool pin and shoulder (Chen & Nakata, 2009; Shah & Badheka, 2016; Zhang et al., 2014; Zhao et al., 2018).

(d) ***Tool offset***

The tool offset is defined as the FSW tool moving away from the joint's centre line toward either of the base plate's sides or, in other words, when the distance between adjoining edges to the tool axis line changes. When the welding tool is precisely positioned over the weld centre line, no or negligible pin eccentricity occurs.

The eccentricity of the pin toward the lower thermal conductivity or weaker work material resulted in a sound and defect-free joint. For FSW of Steel-Mg alloys, a pin eccentricity of 1–2 mm was recommended to ensure high-quality welding (Kasai et al., 2015a; Mishra & Ma, 2005b; Zhao et al., 2018).

## 2.4 Friction stir alloying (FSA)

Insert filler materials as second phase reinforcement additives used for miscible and immiscible materials welding have received much attention. Many researchers used

additives during FSW to study material flow or enhance joint mechanical characteristics (Ibrahim et al., 2016; Muhamad et al., 2021). Friction stir alloying (FSA), which is based on the concepts of friction stir welding, has gained a lot of traction as a surface modification and fabrication of alloyed joints (Sharma et al., 2020). FSA is a very effective approach for fabricating metal–matrix nanocomposites, fine-grained metals, homogenising powder metallurgy processed and cast materials, and composite joints using second phase additive. Apart from thermal exposures and mixing, the FSA tool stirring combined with the extrusion of base materials results in a substantial microstructural modification that happens during the FSA process owing to applying severe plastic deformation to the material (Moiduddin et al., 2021; Shukla et al., 2020).

### 2.4.1 Nanomaterials additives in friction stir alloying

In recent years, researchers have been utilising the fabrication of MMC by the FSP method to develop MMC welded joints owing to the excellent properties by adding various additives at abutting edges of plates in the FSA process. The first research used SiC particles as additive particles during the FSA of copper plates in the butt joint configuration (Sun & Fujii, 2011). Researchers observed that the microhardness of the FSA joint was considerably enhanced using SiC reinforcement as compared to without reinforcement. Researchers investigated the effect of SiC nanoparticle reinforcing in the FSA of AA7075-O (Bahrami et al., 2014; Bahrami et al., 2015; Helmi et al., 2014). They reported remarkably improved tensile strength, fatigue life and toughness of joints. Karthikeyan and Mahadevan (2015) examined the SiC particle reinforced FSA of AA6351 alloy. They reported that growth in grain boundary was hindered because the pinning effect of SiC led to enhanced tensile properties. Recently apart from using SiC particles, researchers are also examined nanoparticles such as metal powder, $B_4C$, and $Al_2O_3$ as reinforcement in the FSA process (Abioye et al., 2019; Singh et al., 2016).

The size of the reinforcement particle is very crucial in deciding the properties of MMC; therefore, their particle size affects the joint properties most significantly (Balog et al., 2014; Poletti et al., 2011). Researchers examined the effect of reinforced particle size in FSA. They used three different Al particle sizes, 9 μm, 63 μm and 250 μm, as reinforcement. They found that by increasing particle size, tensile strength and hardness decrease. The best result came with the lowest particle size reinforcement (Nosko et al., 2019). Also, researchers investigated the FSA of the AA6092/SiC composite plate. At three different tool rotational speeds, 1000 rpm, 1500 rpm, and 2000 rpm, they got different nugget zone particle sizes. They found that at 1500 rpm higher amount of fine particle size is present in the nugget zone, which subsequently leads to higher tensile strength, elongation and ductile mode fracture (Acharya et al., 2019). Nowadays, researchers are focusing on reinforcement FSW using nanoparticles as a reinforcing agent. Researchers reported a study on FSA using copper metal nanoparticles (Rezaee et al.,2018), $TiO_2$ nanoparticles (Pouriamanesh et al., 2019), TiC nanoparticles (Dragatogiannis et al., 2016) and CNT (Zhao et al., 2017) as an additive material.

#### 2.4.1.1 Types of nanomaterials additives and their effect on joints properties

A variety of reinforcement additives has been used in FSA as reinforcing materials to achieve metal matrix composite joints (Abioye et al., 2019; Inada et al., 2010; Nosko et al., 2019; Singh et al., 2016). Reinforcement particles initial size is a decisive parameter to the properties of metal matrix composite (MMC), an additional benefit to the strengthening mechanism when an incoherent reinforcement/matrix interface is accomplished altogether with an excellent distribution of reinforcing particles (Balog et al., 2015, 2014, 2011). Due to this incoherency, load-bearing capacity can be increased between the reinforcing agent and matrix in the composite structure (Kurmanaeva et al., 2015; Lavernia et al., 2008). According to the Zener pinning effect, in the presence of nanomaterials additive reinforcement particles, the grain boundary movement, which is

migrating because of the growth of grain and recrystallisation, may be pinned by reinforcement particles. The grain size limitation through the Zener limit, R(lim) is expressed in equation (2.1) below (Phaneesh et al., 2012; Rohrer, 2010).

$$R(\lim) = \frac{4r}{3f} \tag{2.1}$$

Where r and f are the mean radii and volume fraction of pinning particles, respectively, according to equation (2.1), the refinement of grain by reinforcement particles improves with the increase in particle volume fraction and decrease in size of the particle—the schematic of reinforcement particles pinning is represented in Figure 2.32.

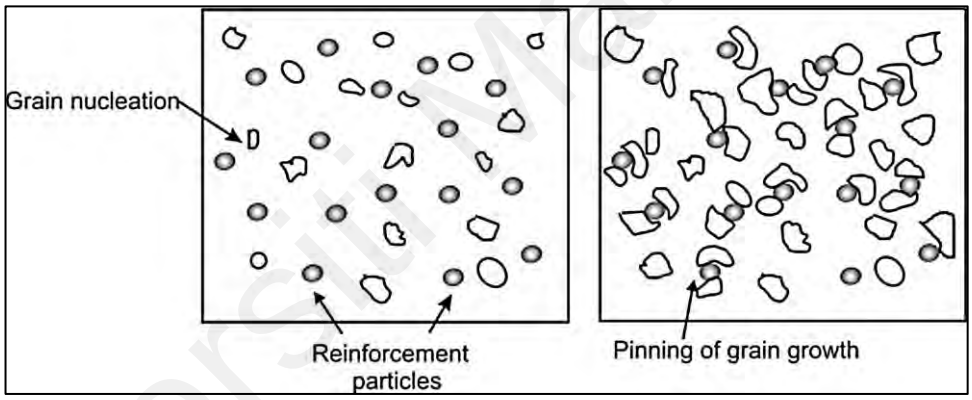


**Figure 2.32: Grain growth pinning by reinforcement particles** (Sharma et al., 2015)

Researchers investigated the effect of micro and nano silicon carbide (SiC) reinforcement on the properties of dissimilar FSW between AA6061 and AA2024. They found that the nano SiC reinforced nugget zone's grain size has decreased more than that of the micro SiC reinforced weld nugget zone's grain size during the FSW process. Further, tensile strength and toughness improved in nano SiC reinforced joints as compared to that micro SiC. They reported that due to the large particle area of the micro SiC reinforcement, agglomeration of micro SiC was more visible than that of nano SiC (Moradi et al., 2018). A similar conclusion has been drawn from alumina reinforced FSW

of aluminium composite by using three different size reinforcement particles (Nosko et al., 2019). This finding agrees with the Zener pinning effect, as mentioned in equation (2.1).

Commonly used nanoparticles reinforcement in FSW to make composite joints are silicon carbide (SiC) (Tebyani & Dehghani, 2015), aluminium oxide or alumina ($Al_2O_3$) (Derazkola & Khodabakhshi, 2020), titanium carbide (TiC) (Karakizis et al., 2018b), titanium dioxide or titania ($TiO_2$) (Mirjavadi et al., 2017) and carbon-based nanomaterial like carbon nanotubes (CNTs) and graphene. The nanomaterials used as reinforcement in FSW can be categorised into ceramic nanoparticle reinforcement and carbonaceous nanomaterials reinforcement. Figure 2.33 illustrates the nanomaterials which were already addressed in reinforcement FSW in research.

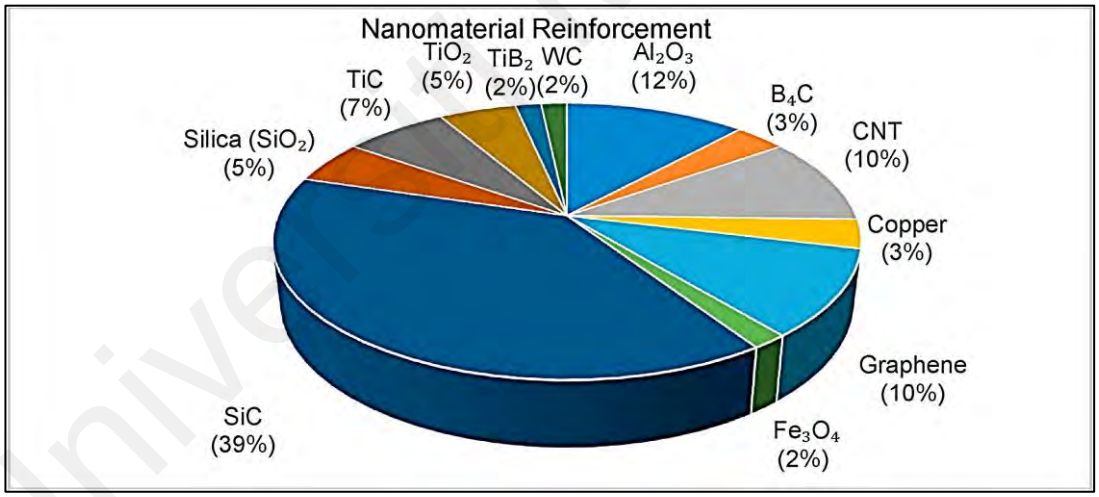


**Figure 2.33: Nanoparticle reinforcement FSW: identification of the nanomaterials addressed in research**

Research in the domain of carbon was revamped by carbon nanotubes (CNTs) and graphene discovery, which are also termed wonder materials (Geim & Novoselov, 2007; Iijima & Ichihashi, 1993). It has been soon noticed by researchers that graphene and CNTs reinforce abilities across the globe. Thus, CNTs and graphene emerged as ideal reinforcement for composite structures due to their intrinsic characteristics (planar

geometry, high aspect ratio) and exceptional physical, mechanical, electrical and thermal properties (Baig et al., 2018). Owing to these excellent properties study was conducted in the field of FSP to make composites. Carbonaceous nanomaterial's (CNTs and graphene) large surface area accommodates its adequate interfacial bonding with the matrix of the composite. A tremendous decline in the rate of wear has been observed during the processing of Al-graphene composite through FSP (Maurya et al., 2016). Similarly, there is a 15% increase in thermal conductivity by the FSP process observed (Jeon et al., 2014). As well a 50% of hardness increment has been observed in the graphene reinforced composite material (Khodabakhshi et al., 2018). Table 2.3 shows the significant properties of CNTs and graphene.

**Table 2.3: Properties of CNTs and graphene** (Baig et al., 2018)

| **Properties** | **CNTs** | **Graphene** |
|---|---|---|
| Physical Structure | Tube | Platelet |
| Available Types | Single or Multiple walls | Single or Multiple sheets |
| Dimensions (nm) | Single wall diameter = 1–2 nm | Single Sheets thickness ~1 |
| | Multiwall diameter = 4–20 nm | Multiple sheets thickness =(Approx.) ~no of sheets × 1 nm |
| Tensile Strength (GPa) | 60–150 | 130±10 |
| Thermal Conductivity (W/(mK)) | 3500 | $(4.84\pm0.44)\times10^3$ to $(5.30\pm0.48)\times10^3$ |
| Electrical Conductivity (S/m) | 3000–4000 | 7200 |
| Electron mobility ($cm^2$ /(V s)) | $\sim10^5$ | $2.0 \times 10^4$ |

Further research was conducted in owing to achieve better joint with carbon-based nanomaterials reinforcement during the FSW process. An experiment was performed using FSW on CNTs reinforced Al-Mg-Cu alloy composite plates (Zhao et al., 2017). During FSW in the NZ, CNT tubular morphology was retained even with severe

deformation. However, a reduction in the length of CNT was reported by authors from about 150 nm to about 80 nm. The size of grain in the nugget zone is coarsened to about 400 nm. It is due to the combination of severe deformation and heat input, as earlier researchers reported that composite CNT/Al grain size would remain stable when subjected to annealing at 723 K (Lipecka et al., 2011). Eccentric weave FSW was conducted on AA6061 T6 and Pure copper plates reinforced with graphene. Weave welding is a form of Friction stir welding technique in which the tool is stirred eccentrically in the weaving format. The tool path forms a sinusoidal pattern. With Pin offset and weaving motion, proper dispersal of graphene particles has been observed and an enhanced mechanical property reported by authors. Possible strengthening mechanisms might be the diffusion of graphene nanoparticles at nano levels, which fortify the yield strength of joints. According to the Hall-Petch relation, the reinforcement particle's grain size affects the mechanical strength of the joint. Hence the graphene serves as filler in the voids (Jayabalakrishnan & Balasubramanian, 2018).

Apart from using the carbonaceous nanomaterial for reinforcing the metallic joint produced by FSW, polymers also have been welded through FSW using carbon-based nanomaterial as a reinforcing agent. Researchers reported dissimilar thermoplastic friction stir welding between high-density polyethylene (HDPE) and acrylonitrile butadiene styrene (ABS) reinforcing with multi-walled carbon nanotubes (MWCNTs). A groove was fabricated with different widths, such as 0.2 mm, 0.3 mm and 0.4 mm, on the ABS plate to accommodate different volume fractions of MWCNTs reinforcement. After filling of MWCNTs into the groove of the ABS plate, the HDPE plate was placed at the top surface of the ABS plate. Lastly, to provide submerged friction stir welding (SFSW) system water tank was mounted on the plate. The joint reinforced with 1.5 volume per cent of MWCNTs shows the highest value of the tensile strength, 14.7 MPa, improved up to 65.3% compared with base HDPE. Apart from 1.5 volume per cent, tensile strength

decreased in both 1.0 and 2.0 volume per cent of MWCNTs reinforced joints. Furthermore, the tensile strength of MWCNTs reinforced joint with all volume content exceeded that joint without MWCNTs (Gao et al., 2015).

Another application of carbon-based nanomaterial reinforced FSW, besides enhancing joining strength, is to make Carbon nanotubes reinforced Al composite foam. The authors fabricated a foamable precursor by mixing titanium hydride ($TiH_2$) as blowing agent powder and carbon nanotubes (CNTs) as reinforcement into 1.5 mm thick AA1080 aluminium sheets using the FSW route. Subsequently, the closed-cell Carbon nanotubes and aluminium composite foams are obtained by placing the precursor in a furnace for foaming. For this, three aluminium plates were stacked and clamped for the FSW process. Before stacking, the $TiH_2$ and CNTs were distributed homogeneously into each AA1080 plate. An overlapping FSW with multi passes has been performed to mix segregated $TiH_2$ and CNTs uniformly (Pang et al., 2019).

(a) ***Effect of carbon-based nanomaterials additive on microstructural characterisation***

The fabrication of joint in nanomaterial additive reinforced FSA is a complicated procedure involving thermomechanical actions among work material, tool and reinforcing material. Microstructural characterisation of joints produced by FSA must be analysed to examine the behaviour of nano-additive and base material with each other during FSA. An overview of the microstructural is conveyed in this section. The characterisation is mainly focused on the weldment's different zone.

Carbonaceous nanomaterials, mainly graphene and CNTs extensively used as reinforcing material in metal matrix composites due to their excellent inherent properties. The use of carbonaceous nanomaterial in FSW as a reinforcement is also emerging nowadays. Several initial studies reported on the use of carbon-based nanomaterial as a potential reinforcing material. Montazerian et al. (2019) investigated dissimilar FSW

between pure aluminium and pure copper with graphene reinforcement. It has been observed that the addition of graphene nanoparticles enhances the mixing of copper and aluminium in the stir zone. The hardness of graphene particles is high in comparison with base metals, which causes the detachment of finer copper particles from the copper base metal during the welding. The graphene nanoparticles and detached fine copper particles inside the aluminium matrix are directed to the development of a layered structure due to the rotating tool stirring action. The development of these layered structures increases the actual interface between aluminium and copper. This layered structure makes an area across the interface for the interdiffusion of Al and Cu atoms to extend. Furthermore, the average grain size of the stir zone is not affected by the graphene addition. The reason behind the almost similar grain size of stir zone with and without graphene is the agglomeration of graphene at just one pass of FSW. These large graphene reinforcement agglomerates cannot pin the grain boundaries, and thus they have no substantial effect on the grain structures. However, an increase in the stirring time because the following passes one after another reduces the size of the graphene reinforcement agglomerates and enhances the proper distribution of the graphene particles. Graphene reinforcement particles with submicron size may reduce the grain size by pinning into the grain boundaries during the grain growth.

In addition to grain refinement, graphene can also serve as a welding defects inhibitor effectively (Sharma et al., 2020). Authors experimented with FSW of AA6061 alloy in lap configuration with a graphene interlayer as reinforcement. Various defects and microstructure of different zones are represented in Figure 2.34 with GNP interlayer and Figure 2.35 without GNP interlayer.

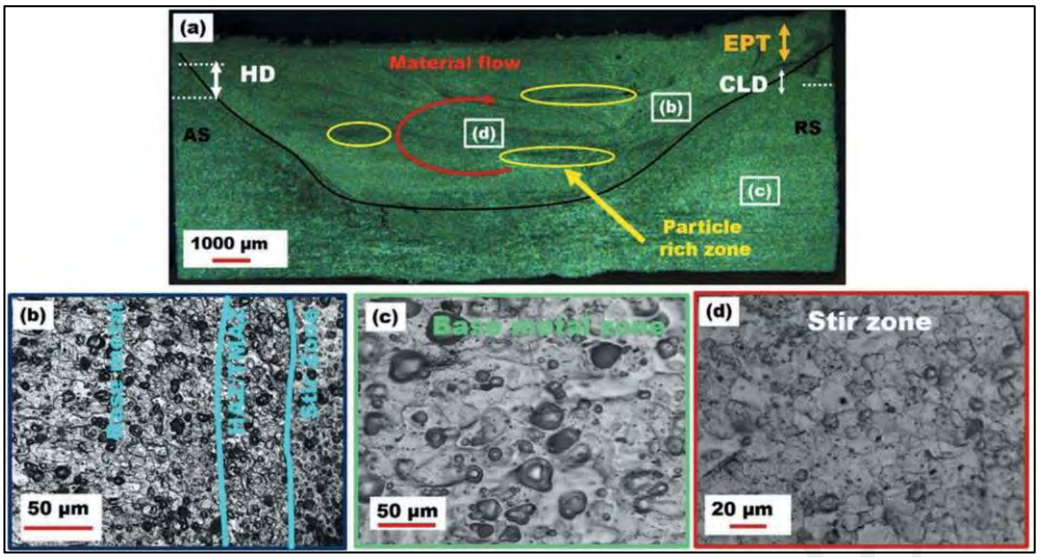


**Figure 2.34: (a) Macrostructure, (b–d) microstructural images with GNP interlayer** (Sharma et al., 2020)

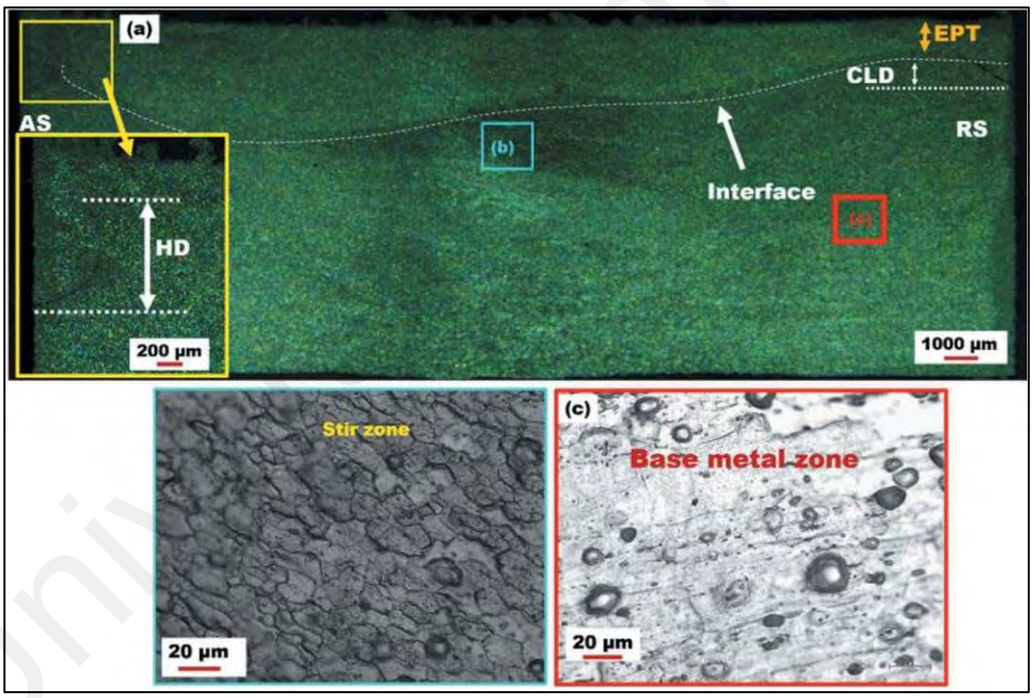


**Figure 2.35: (a) Macrostructure, (b and c) microstructural image without GNP interlayer** (Sharma et al., 2020)

Defects like cold lap defect (CLD) and hooking defect (HD) were visualised by researchers. This CLD and HD imply that the effective plate thickness (EPT) is inadequate and affects the shear strength of the joint negatively. They also reported the joint with GNP interlayer as reinforcement for both CLD and HD height, significantly reduced compared to the joint without GNP interlayer. The reason behind the reduction

in the height of defects is as the probe of the tool reaches the interface, the GNP interlayer at that place gets deformed and goes up from corners, as in the case of back extrusion during forming of thin sheets. Because of the stirring of the probe, this deformed interlayer gets fragmented and formed into GNP particles. Since a significant portion of heat is generated by the tool shoulder in FSW, the portion of material gets heated up, which is in contact with the shoulder and further loses its yield strength as compared to material available at the interface or bottom of the workpiece.

Carbonaceous nanomaterials are not only successfully applied in metal welding but also emerge as a potential reinforcement for the FSW of polymers. One such successful use of MWCNTs as reinforcement in the FSW of HDPE and ABS is addressed (Gao et al., 2015). They found joints produced without chipping and smooth on the advancing side (AS), whereas white chipping and some flashes were found at the retreating side (RS). The factor responsible for this difference is during FSW of polymer, a rotational zone forms on the advancing side because of material rotation with the pin of the tool at this side, while this is not happening on the retreating side. Additionally, the polymer's poor conduction of heat limited the heat transfer to the retreating side. FSW joints without MWCNT reinforcement contained defects such as flashes, cracks and material chippings. The difference in heat distribution between AS and RS cause poor material flow, and the surface produced is non-uniform and defective. On the other hand, the joints with MWCNT appeared smooth and well mixed. Because when MWCNT is applied between HDPE and ABS, thermal conductivity inside the weld zone improves, and this improvement in heat conduction promotes the forming property of the weld. Although at a low volume of MWCNT, this improvement is not noticeable; the surface got better with an increase in the content of MWCNT, as reported by the authors.

(b) ***Effect of carbon-based nanomaterials additive on FSA joint properties***

Reinforced FSWed specimen's mechanical properties are influenced by several factors, including interaction responses of base materials and nanoparticles with each other under various process parameters, grain size, and dislocation density. According to the Hall-Petch relationship, a reduction in the size of grain leads to the enhancement of tensile strength ( $\sigma_y$ ). (Equation 2.2) (Sanaty & Zadeh, 2012).

$$\sigma_y = \sigma_0 + k_y d^{-\frac{1}{2}} \tag{2.2}$$

Where $\sigma_0$ is the original strength of the material, $k_y$ is the material constant and $d$ is the grain size of the material. In the unreinforced FSW process, grain refinement due to dynamic crystallisation is responsible for the mechanical properties of joints. However, in the particle reinforcement condition, additional parameters include the bonding between matrix and reinforcements, which contributes to load transfer applied to the joint (load-bearing effect), particle dispersion, dislocations due to thermal expansion coefficient mismatch between reinforcement particle and matrix (Orowan strengthening) also taken into consideration (Sanat & Zadeh, 2012; Sato et al., 2003).

One of the purposes of adding nanoparticles during FSW is to improve mechanical properties like tensile strength, hardness, toughness, and fatigue. The mechanical characterisation is one of the criteria onto which one can decide whether weld quality is acceptable or not. It has been observed that nanoparticles can fulfil these requirements when used as reinforcement during welding.

As mentioned in the previous section, owing to the excellent properties of carbonaceous, mainly CNTs and graphene nanomaterials, it could be futuristic reinforcement material on a large scale. In the current scenario, there is limited research

conducted on carbon-based nanomaterials reinforcement, but results of available literature indicate that in upcoming years it would be a better choice as reinforcing material in the FSW process and other welding processes. The research was carried out by using a graphene interlayer as reinforcement in the lap welding of AA6061 alloy ( Sharma et al., 2020). Researchers reported that there was an improvement in the failure load from 14 N/mm in the joint without GNP reinforced interlayer to 31 N/mm in the joint with GNP reinforced interlayer, which is about a 121% increase in the joint strength. Additionally, elongation was also improved by 53%, from 0.45% in the joint without GNP reinforcement to 2.83% in the joint with GNP reinforcement. It has been observed that a significant yielding of material took place before failure under the loading with the GNP interlayer specimen. Fine dimples depict a ductile mode of fracture along with the insignificant amount of featureless region that is cleavage fractures. Fracture with the mixed-mode at the different regions is because of GNP dispersion variation across the stir zone.

There are possibly four strengthening mechanisms behind the improved mechanical properties of joint reinforced with GNP, namely (a) coefficient of thermal expansion (CTE) gap between aluminium matrix and GNPs, (b) Hall-Petch mechanism associated with refined grain, (c) shear lag or load transfer mechanism and (d) Orowan mechanism. According to the Zener-Holloman effect hindering grain growth results in the reduction of grain size from 10.23 μm in joint without GNP reinforcement to 5.18 μm in joint with GNP. Thus, almost 50% reduction in the size of grain by using GNP as reinforcement. There is a massive mismatch between the CTE of the matrix and reinforcement exist. This mismatch results in punching of dislocation at the boundaries. Also, there is an increase in the dislocation density in the aluminium matrix due to the consistent dispersion of GNP. Moreover, due to this, piling up of dislocations at the matrix and GNP interface improves joint strength further. These generated dislocations along Al-GNP boundaries

are blocked by tiny-sized GNP particles according to the Orowan mechanism. Consequently, there is a bending of these locations, which generates back stress and further enhances the yield strength of weld zone material. Transfer of load between aluminium and GNP was established along with the interface of the aluminium and GNP. The load transfer is governed by bonding strength within the Al and GNP matrix. There are two more mechanisms that may have helped in the strengthening of joint with reinforcement of GNP;(a) $Al_2O_3$ formation prevention at the interface and (b) graphene nanoplatelets delamination into a few layers.

As there is an increase in the use of CNT as reinforcement to make composites observe. Their welding is challenging through the conventional process. However, researchers successfully welded CNTs reinforced AA2009 alloy by the FSW process (Zhao et al., 2017). The ultimate tensile strength (UTS) of the FSW joint strength of the CNT reinforced specimen has been improved by 87% up to 550 MPa, from a base metal strength of 630 MPa. However, lower ductility shows the direction of tension was perpendicular to the carbon nanotubes alignment direction. The hardness of the welded specimen with reinforcement shows a fluctuated manner with the lowest value of 175 HV as compared with BM hardness, 208 HV. Coarsening of nugget zone grain which is reported by authors, is probably the reason behind the decrease in hardness value. Furthermore, the author observed that the orientation of CNT in NZ was random, whereas, in BM, it was aligned. Since testing of microhardness acts as a micro compression test and due to misalignment of CNT in the nugget zone, this fluctuation and reduction of hardness observe. Similarly, researchers analysed the effect of per cent volume MWCNT reinforcement on mechanical properties of FSWed Al/MWCNT composite joints (Lee et al., 2018). They reported that MWCNT is dispersed well in the aluminium matrix with retaining in its tubular structure. It has been observed that $Al_4C_3$ with a length of 500 nm is produced due to bonding between decomposed MWCNT and

Al matrix in small quantity. It has been found that with an increase in volume per cent of MWCNTs, engineering stresses also increased. The mechanical properties of tensile strength, yield strength and total elongation improved to 450 MPa, 400 MPa, and 13.9% for the specimen with 3 volume per cent MWCNT from 323 MPa, 250 MPa, and 19.9% for the specimen with 1 volume per cent MWCNT, respectively, due to transfer of load efficiently of MWCNTs in the aluminium matrix. Weldability of the MWCNT reinforced FSWed specimen was calculated as the ratio of tensile properties (tensile strength and total elongation) of the weld to that of the base metal. Weldability based upon tensile strength is found to be more than 80%, irrespective of plunging load and MWCNT per cent content. Similarly, weldability based upon total elongation enhanced significantly and achieved 236.7% for 600 kg plunging load and 3 volume percent of MWCNT.

Furthermore, lap joints hook defect is inevitable. The authors tried to enhance the strength of the hook defect tip to improve overall joint efficiency. A lap joint of AA2014 aluminium alloy fabricated with graphene nanosheets (GNs) with a thickness of 50-100 nm by FSSW. The shear strength of the GN reinforced joint was found to be 5212 N, with an improvement of 31% observed as compared to the shear strength of (3973 N). unreinforced joint. Additionally, the joint fracture displacement is enhanced by about 20%. Thus, the area below the load-displacement curve is remarkably increased, which signifies joint toughness. It has been illustrated that graphene nanosheets played an essential role in deciding the aluminium matrix strength. The strain hardening strengthening mechanism contributes to enhanced shear strength. Furthermore, crack bridging and crack defection are mechanisms accountable for the increased toughness of reinforced joints. Crack bridging enhances the essential resistance to microstructure deterioration and fractures in front of the crack tip where it takes place. GNs reinforcement bridge the elongated crack in the back of the crack tip. The crack defection

mechanism aims to diminish the intensity of local stress experiences in the front or back of the crack tip (Wang et al., 2020).

## 2.5 Method of nanoparticles deposition

The amount of reinforcing material in the weld nugget zone is a crucial factor in determining the properties of the reinforced joint. Researchers applied various methods for the deposition of nanomaterial in the welding zone. In the initial stage of reinforced FSW, researchers preferred the open groove method for applying nanoparticles in which the adjoining side of the specimen was machined to allow a groove formation and reinforcements were pressed into the groove tightly (Bahrami et al., 2014; Fallahi et al., 2017; Paidar et al., 2018). However, during the FSW process, nanoparticles were splattered from grooves due to the force generated during the process. This made an inappropriate proportion of nanoparticles available inside the welding zone. To avoid this spilling problem, some authors used a slurry of nanoparticles mixed with ethanol inside the open groove and made nanoparticles manageable (Dragatogiannis et al., 2016; Kartsonakis et al., 2016). In some experiments before welding, the open grooves were subjected to a pinless tool to avoid expulsion of the nanoparticles out of the groove during the friction stir welding process (Bodaghi & Dehghani, 2017; Karakizis et al., 2018a). Apart from the conventional groove method, authors have developed various innovative methods of nanoparticle deposition. Researchers developed the nano-particle deposition system (NPDS) (Hong et al., 2017). Before FSSW, carbon was coated as reinforcement on the surface of the Al6061-T4 alloy sheet (the upper sheet of the dissimilar lap joint) using the NPDS system. In this system, graphite compressed air carried powder from the powder feeder to the nozzle. A converging nozzle has been used between the nozzle inlet and outlet to accelerate the powders. This accelerated powder fed into the deposition chamber at room temperature. Then there was an impact made between accelerated graphite and the surface of the aluminium 6061-T4 alloy sheet for deposition. The mixing

of graphite into the metal matrix during FSSW with NPDS has been confirmed by Raman Spectrum analysis. Researchers used the FSP process to seal the SiC nanoparticles. For this purpose, a groove was machined on the AZ31 faying surface. FSP method using a pinless tool and with three passes has been carried out to seal the groove to avoid the nanoparticles splashing out during FSW, as shown in Figure 2.36 (Abdollahzadeh et al., 2019).

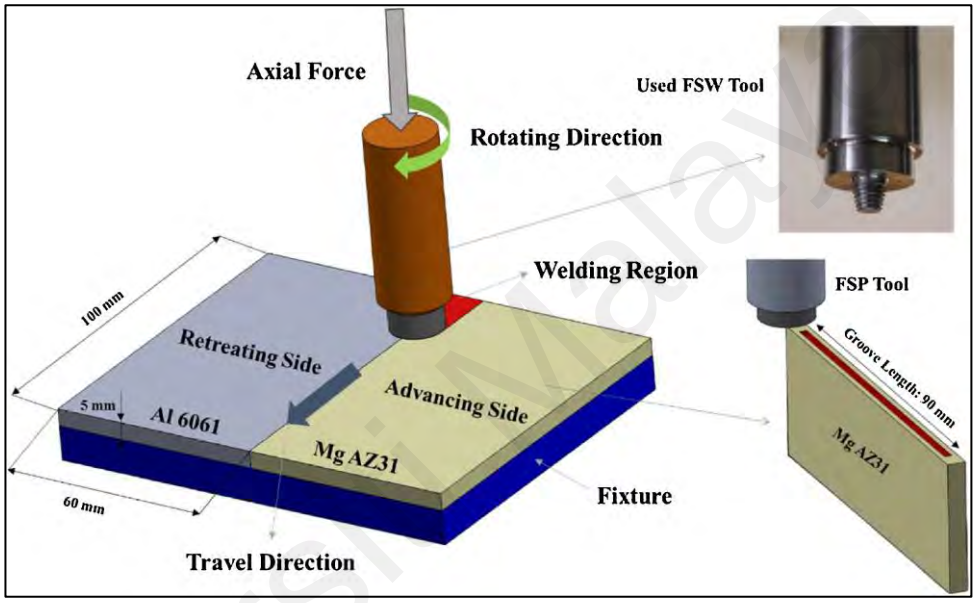


**Figure 2.36: FSA processes image** (Abdollahzadeh et al., 2019)

The dispersal of nanoparticles on the AZ31 faying surface can be seen in Figure 2.37, with different passes. We can see that with one pass, SiC particles agglomerated around the initial groove. With two passes FSP, the initial groove has vanished, and the extent of agglomerated particles low than the previous single pass. Whereas uniform dispersal of SiC is observed after three FSP passes. EDS peak verifies the occurrence of SiC rich zone. This enhanced dispersal of nanoparticles is because of particle separation during every pass from agglomerated clusters.

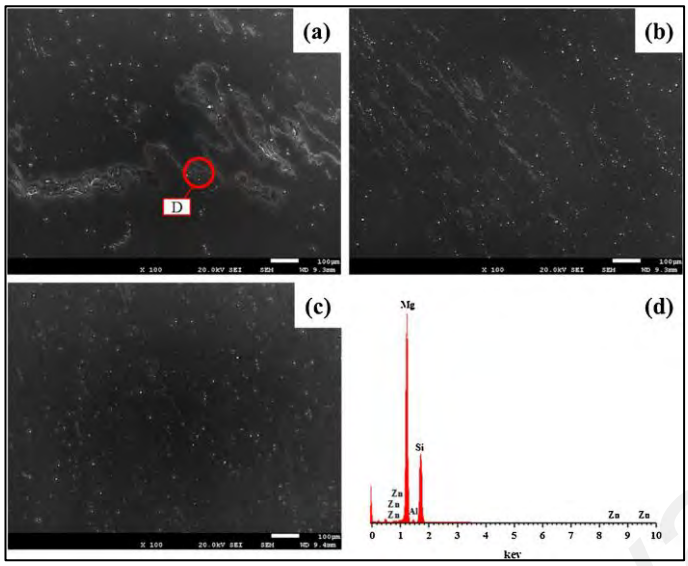


**Figure 2.37: FESEM images of the faying surface of Mg with friction stir processed: (a) one pass, (b) two passes, (c) three passes, (d) EDS peaks of point D denoted in (a)** (Abdollahzadeh et al., 2019)

In another innovative method of deposition, Singh et al. (2020) incorporated reinforcement nanoparticles into cylindrical 30 holes, with a diameter of 1.5 mm and depth of 3 mm drilled at the faying edges of the base material, Figure 2.38.

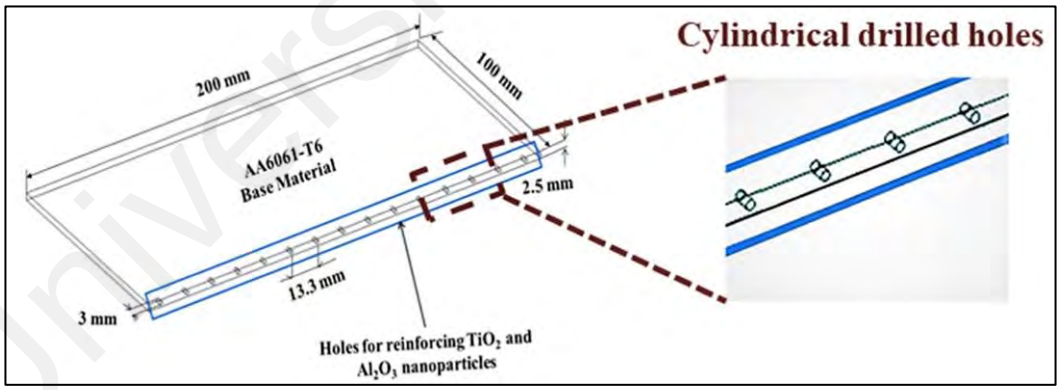


**Figure 2.38: Schematic of nanoparticles deposition** (Singh et al., 2020)

Furthermore, an innovative groove has been designed by authors in such a way that the reinforcing particles are fully sealed between the specimens to ensure that there is no reinforcing nanopowder expulsion during the welding process. In this groove design, a groove with 1.5 mm depth in Mg plate and a raised height of 1 mm in Al plate have been created, which are illustrated in Figure 2.39 (a). Lastly, an embedded groove having 0.5

mm depth is obtained between the plates when the locking of workpieces takes place, according to Figure 2.39 (b) (Sharifi et al., 2019).

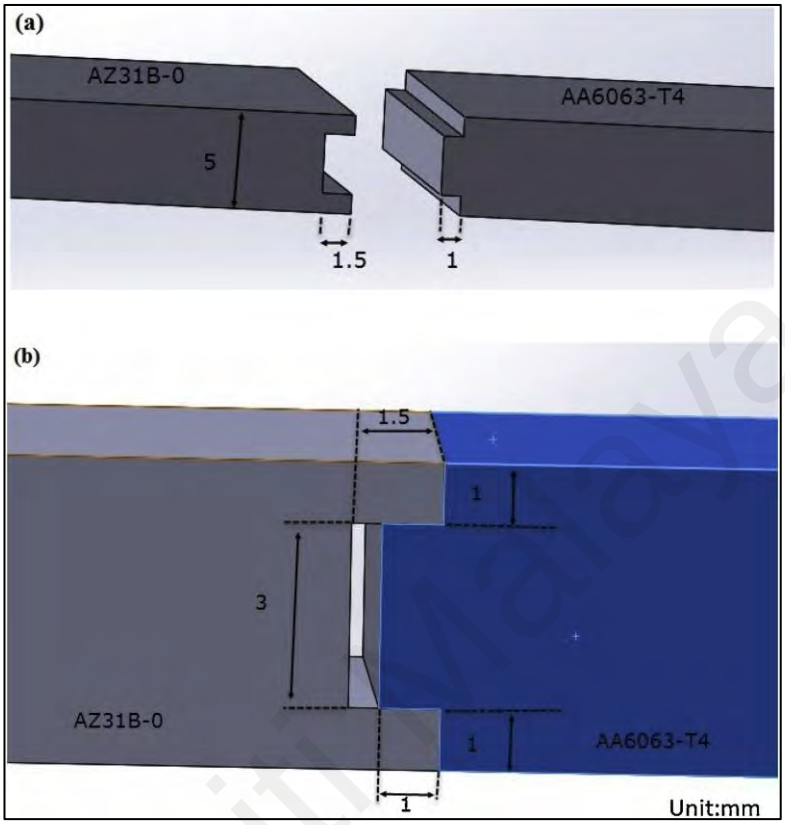


**Figure 2.39: Novel groove design to embed nanoparticles: (a) initial workpieces (b) after interlocking** (Sharifi et al., 2019)

In carbon-based reinforcement, the method of deposition depends upon process requirements. It may be in interlayer form, slurry form or powder form. In one such study of graphene reinforced FSW, a graphene interlayer is prepared on the upper surface of the bottom plate. Initially, 0.1 gm of GNP is ultrasonicated for 60 minutes in 20 mL distilled water. The solution of 0.1 gm PVA in 20 mL distilled water is prepared separately by using a magnetic stirrer at 80°C for 60 minutes. Both solutions are then mixed and again stirred for another 60 minutes at 80°C. The interlayer is obtained by dipping the substrate (5 mm thick) in the solution (dip-coating) and holding it inside for 60 seconds. At last, the PVA is removed by drying it in the vacuum oven at 80°C for 4 hours. Finally, a graphene interlayer has been obtained (Sharma et al., 2020). In another

set of studies, according to process requirements, MWCNT was deposited in submerged FSW. The groove was fabricated with different widths of 0.2 mm, 0.3 mm and 0.4 mm, on the ABS plate to facilitate different volume fractions of MWCNT reinforcement. After filling of MWCNTs into the groove of the ABS plate, the HDPE plate was placed at the top surface of the ABS plate. Lastly, to provide submerged friction stir welding (SFSW) system water tank was mounted on the plate, Figure 2.40 (Gao et al., 2015).

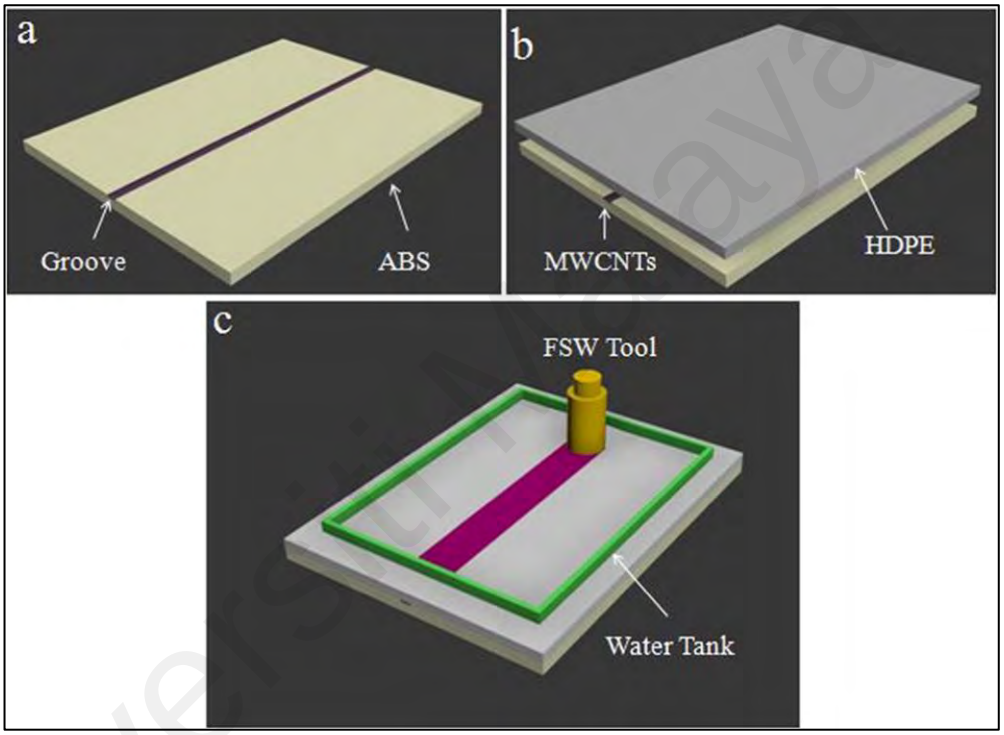


**Figure 2.40: Schematic of the FSW thermoplastics joint with MWCNT reinforcement (a) groove (b) workpieces arrangement (c) water supply** (Gao et al., 2015)

Figure 2.41 illustrates the common issues and possible solutions in immiscible magnesium and steel joining.

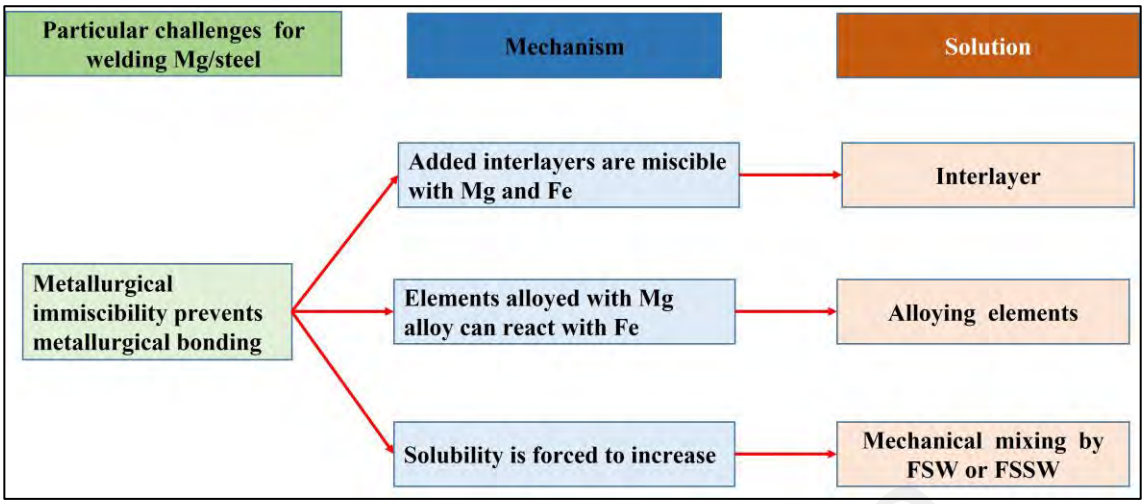


**Figure 2.41: Issues and solution schematic of immiscible joining between magnesium and steel**

## 2.6 Summary

As per the principle of joining dissimilar metals, magnesium alloys will increasingly be used in the car industry, alongside steel sheets for the primary body construction. Both AZ31 and AZ61 magnesium alloys will account for a significant portion of magnesium alloys used in future vehicle construction due to their adequate strength and lightweight properties. Additionally, mild steel is chosen to benefit from its outstanding combination of strength and cost-effectiveness in the current research. As a result, even though compatible metals are selected following the principle of the optimal dissimilar material joint, the issue of how to join dissimilar magnesium alloy and steel persists. The primary problems with Mg/steel dissimilar metal joints are the significant melting point gap, the absence of Mg-Fe IMCs, and the low solubility of solids in an Mg-Fe framework. Figure 2.41 illustrates the common issues and possible solutions in immiscible magnesium and steel joining.

Friction stir welding successfully overcomes significant melting point differences between magnesium and steel dissimilar metals and avoids welding flaws associated with fusion welding. Even though friction stir welding (FSW) is used with optimised parameters, the absence of favourable IMC layers at the interface of Mg–Fe dissimilar

welds seriously affects the welds' mechanical properties. Furthermore, change in base material elemental composition, as reported by researchers, further affect the joint properties. An efficient approach is to facilitate IMC forming at the weld interface to achieve better joint properties from a metallurgical viewpoint. Two potential approaches can be adopted to achieve this goal.

a) Firstly, second-phase metal particles can be used at the interface of Mg-Fe too, which is miscible with both Mg and Fe. So an IMC can be formed with acceptable joint properties.
b) Secondly, the application of promising nanomaterials at the interface of base materials enhances the joint strength further.

Carbon-based nanomaterials such as CNT and graphene can improve mechanical properties like tensile strength, hardness, toughness, and fatigue. The mechanical characterisation is one of the criteria onto which one can decide whether weld quality is acceptable or not. It has been observed that carbon-based nanoparticles can fulfil these requirements when used as reinforcement during welding. Several methods have been developed for the dispersion of reinforcing particles at the joint interface. Methods developed are impractical in terms of industrial use. A proper strategy should be developed for the uniform dispersion of reinforcing nano additive material.

So far, research carried out on FSW of Mg alloy and steel with butt joint configuration is limited. Also, the effect of aluminium particles with and without CNT as reinforcing material is not reported in dissimilar FSW of AZ series magnesium alloy and steel despite potential application in transport industries. The friction stir alloying technique, which is the “FSW process with the additive”, can be employed to achieve both IMC formation and nanomaterials interaction during the immiscible joining process.

# CHAPTER 3: MATERIALS AND METHODOLOGIES

## 3.1 Introduction

This chapter describes the materials utilised and the methods adopted to achieve the objectives. This research used the FSA technique to join immiscible AZ31 and AZ61 with mild steel using different additive materials. Additive materials were selected based on the miscibility of both workpiece materials. In the following section, details from materials and related methods will be described. Figure 3.1 illustrates the flow chart of the experimental work followed.

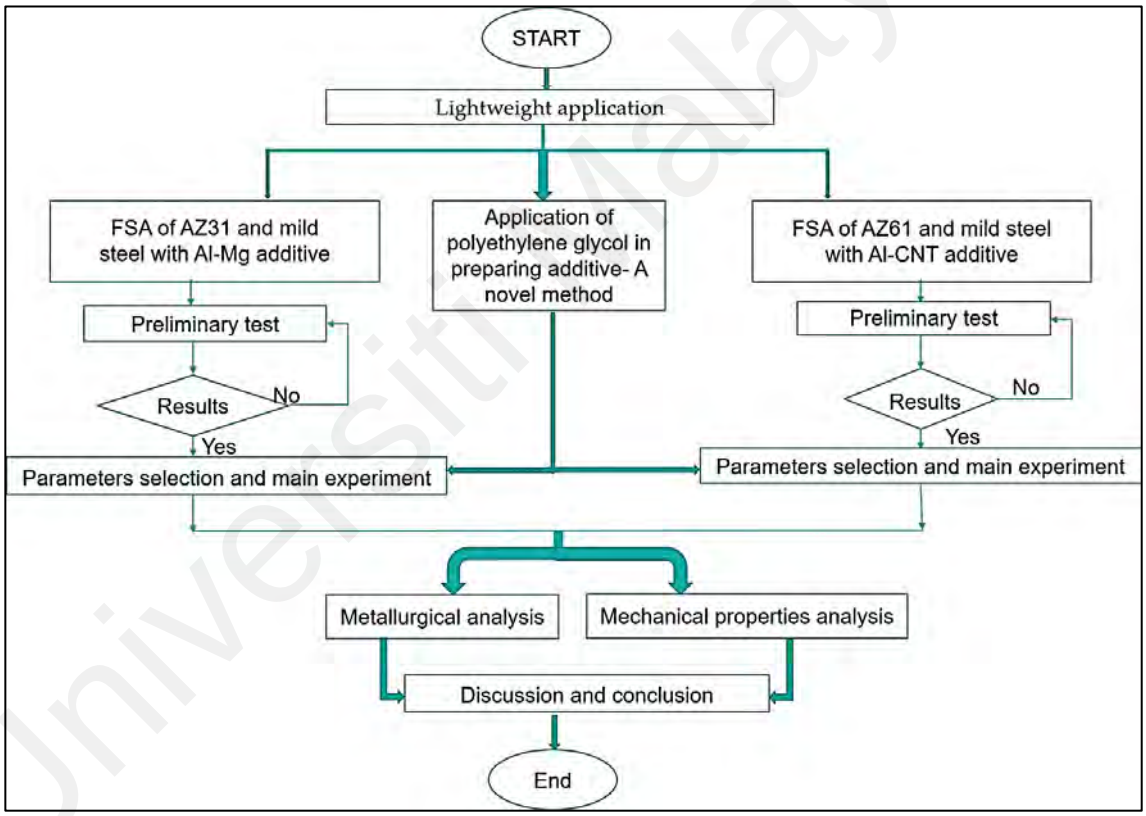


**Figure 3.1: Flowchart of experimentation**

## 3.2 Materials

### 3.2.1 Base workpiece materials

The commercial magnesium alloy of grade AZ31, AZ61 and low carbon steel was used in this research. The low carbon steel commercial name is steel pickle hot-rolled coil (SPHC) with JIS 3131 Japanese standard. Table 3.1 shows milled certified chemical

composition obtained from a material supplier. The schematic of base materials with dimensions is depicted in Figure 3.2.

**Table 3.1: Elemental composition of base materials (weight %)**

| | AZ31 | AZ61 | Mild steel |
|---|---|---|---|
| Magnesium, Mg | Balance | Balance | - |
| Aluminium, Al | 2.80 | 5.85 | - |
| Zinc, Zn | 0.60 | 0.65 | - |
| Copper, Cu | 0.050 | 0.025 | - |
| Nickel, Ni | 0.0050 | 0.001 | - |
| Silicon, Si | 0.10 | 0.05 | 0.01 |
| Manganese, Mn | 0.20 | 0.39 | 0.27 |
| Carbon, C | - | - | 0.05 |
| Phosphorus, P | - | | 0.13 |
| Sulfur, S | - | | 0.05 |
| Iron, Fe | - | - | Balance |

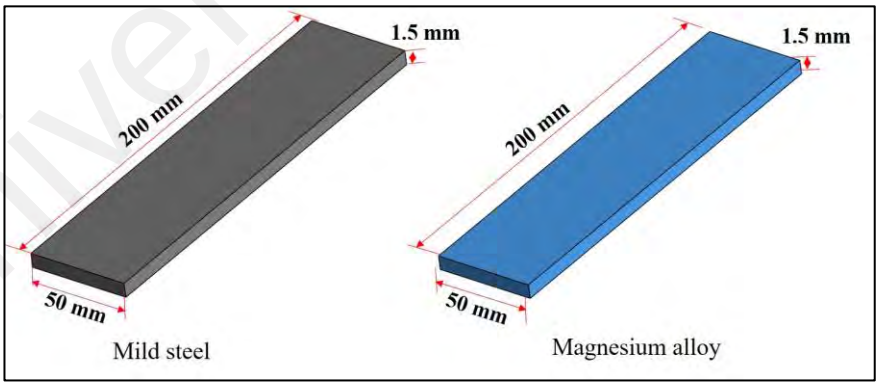


**Figure 3.2: Schematic of base material with dimension**

Table 3.2 shows the mechanical properties of the base material.

**Table 3.2: Mechanical characteristics of magnesium alloy and mild steel**

| Materials | Tensile strength (MPa) | Elongation (%) |
|---|---|---|
| AZ31 | 240 | 6 |
| AZ61 | 250 | 7 |
| Mild steel | 361 | 33 |

### 3.2.2 Magnesium and aluminium powder

Aluminium powder and magnesium (99.9% pure) were procured from ACROS Organic. The average particle size (APS) range was 40 μm for aluminium and magnesium. Figure 3.3 shows an SEM image of as-received magnesium and aluminium powder.

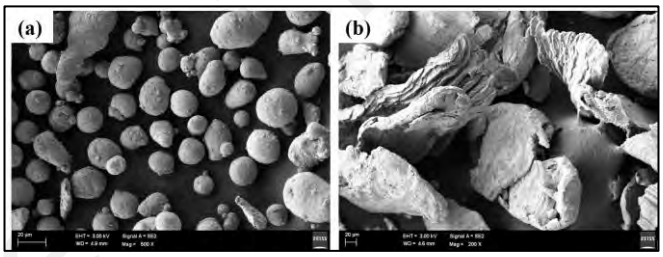


**Figure 3.3: SEM image of (a) Al powder (b) Mg powder**

### 3.2.3 Carbon nanotubes nanomaterial

Multiwalled carbon nanotubes (MWCNT) (98% pure) were procured from Nanostructured & Amorphous Materials. The outside diameter was in the range of 30-80 nm, and the inside diameter was 5-15 nm, as shown in Figure 3.4. The average length of MWCNT was 10 μm. As-received CNT was refined using the acid functionalisation method. The details of acid functionalisation and its analysis are discussed in the result and discussion section.

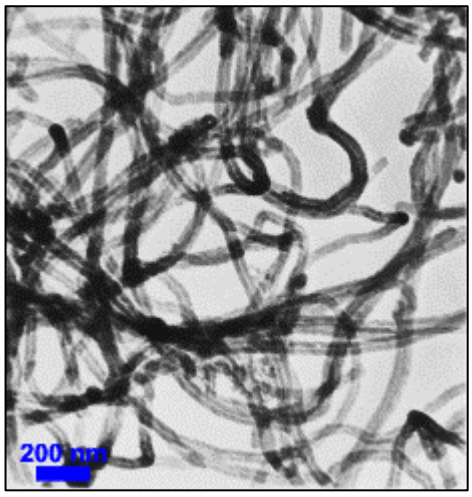


**Figure 3.4: TEM image of carbon nanotubes**

### 3.2.4 Polyethylene glycol (PEG)

Polyethylene glycol (PEG) is used to prepare the additive solution. PEG is hydrophilic polymeric material as well as has the ability to burn out entirely. The molecular weight of PEG used in the current study is 2000, and its melting point is 50 ºC-53 ºC.

The basic idea behind using PEG to make the additive paste is illustrated in Figure 3.5. It can be seen from Figure 3.4 that additive, either Al-CNT or Al-Mg, is mixed with PEG and form semi-solid. This semi-solid additive helps smooth the injection of additive in the FSA process. And due to the heat of the welding process, PEG decomposed from the additive mixture and evaporated. This makes PEG aim only to keep additive in the gap without scattering.

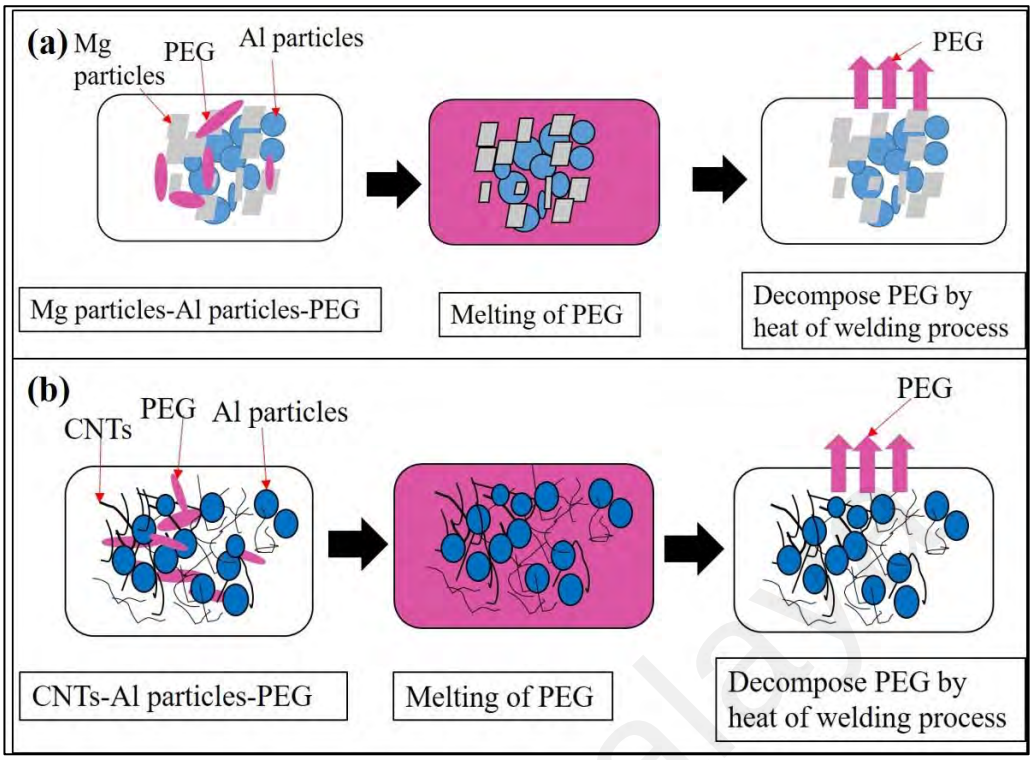


**Figure 3.5: Illustration of PEG mixing and decomposing with additives (a) Al-Mg (b) Al-CNTs**

Thermogravimetric analysis (TGA) analysis of PEG was performed to ensure complete decomposition of PEG during the FSA process, as shown in Figure 3.6. As can be seen from the TGA graph, PEG is completely decomposed at nearly 550 ºC.

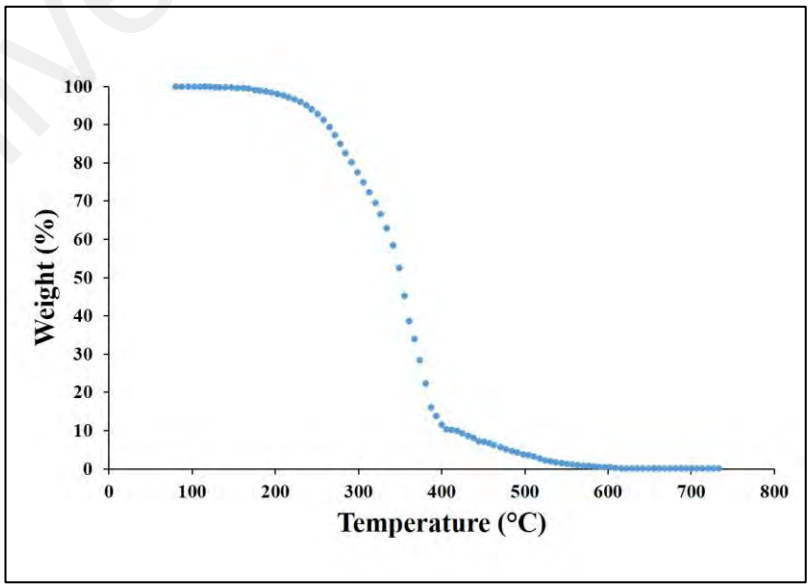


**Figure 3.6: TGA analysis of PEG**

### 3.3 Preparation of additive

For the preparation of the Al-Mg additive, initially, the predetermined amount of metal particles is ultrasonicated for hours in 10mL of ethanol. The ultrasonicated Al-Mg particles were then subjected to magnetic stirring for a further 1 hr to obtain the proper dispersion of both metal particles uniformly, as shown in Figure 3.7.

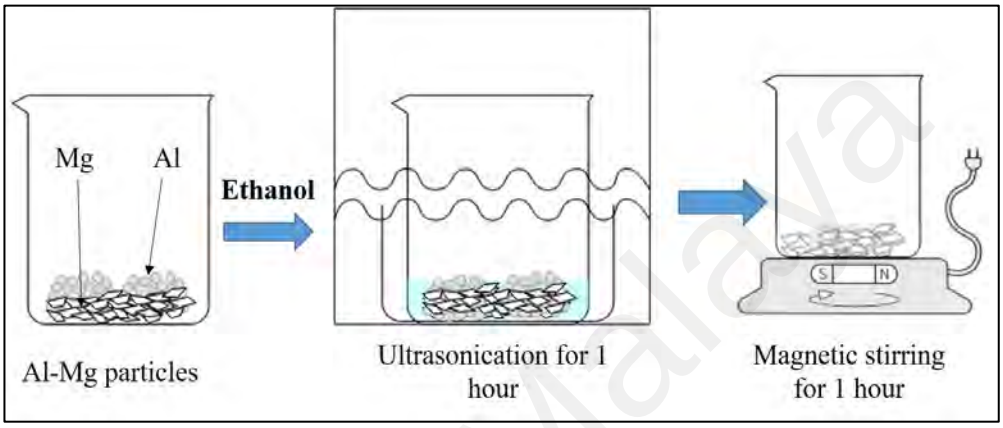


**Figure 3.7: Steps for preparation of aluminium-magnesium additive**

Similarly, the Al-CNT additive was also prepared. The steps followed in preparing the Al-CNT additive are illustrated in Figure 3.8. First of all, a predetermined amount of functionalised CNT is placed in the beaker. After that, it was ultrasonicated for 20 minutes. This particular timing is obtained from past studies for uniform distribution of CNT and to break agglomeration (Baig et al., 2018; Lavagna et al., 2021). Once CNT was dispersed in ethanol properly, Al powder with a predetermined amount was added gradually. The solution of Al-CNT was then ultrasonicated for 10 minutes for proper mixing. In the final step, a magnetic stir was used to increase the uniform dispersion of Al-CNT in the solution.

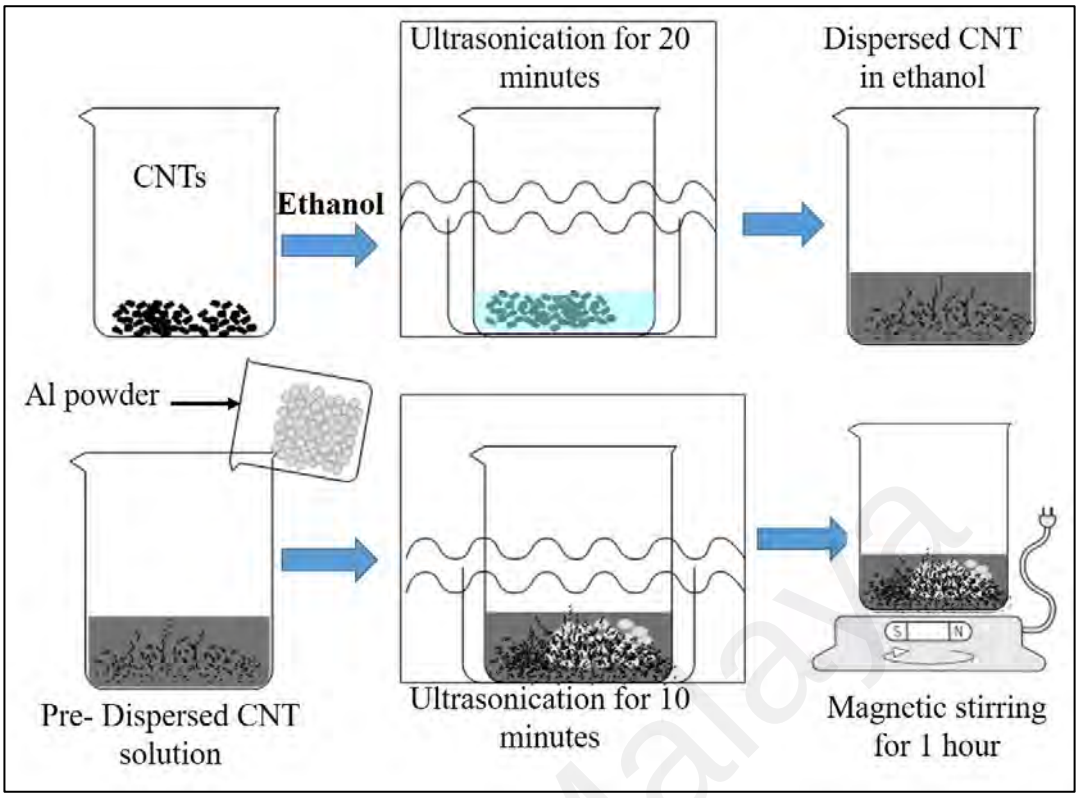


**Figure 3.8: Steps for preparation of Al-CNT additive**

The PEG solution was also prepared using 0.2 grams of PEG with 10 mL distilled water for 1 hour at 80 ºC. In the final stage, additives (Al-Mg and Al-CNT) were added gradually and kept at magnetic stir for 30 minutes at 80 ºC temperature. The schematic of the final stage of the preparation of the additive is depicted in Figure 3.9.

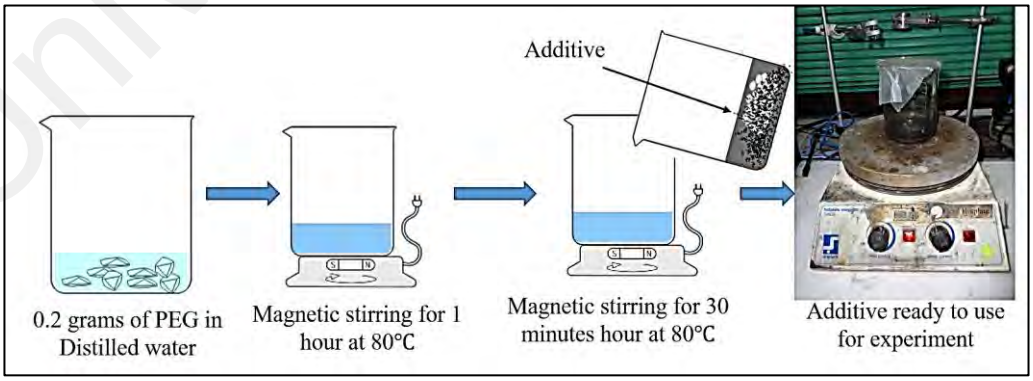


**Figure 3.9: Prepared additive solution for experimentation**

## 3.4 Friction stir alloying tool manufacturing process

The simplified FSA process tool design is shown below in Figure 3.10. There are two primary features of interest, tool shoulder and pin. $P_d$, $P_h$ and $S_d$ stand for pin diameter, pin height, and shoulder diameter, respectively. A critical correlation between the shoulder diameter and pin diameter was observed for optimal results and stated that a ratio of 3:1 should be used (Denquin et al., 2003).

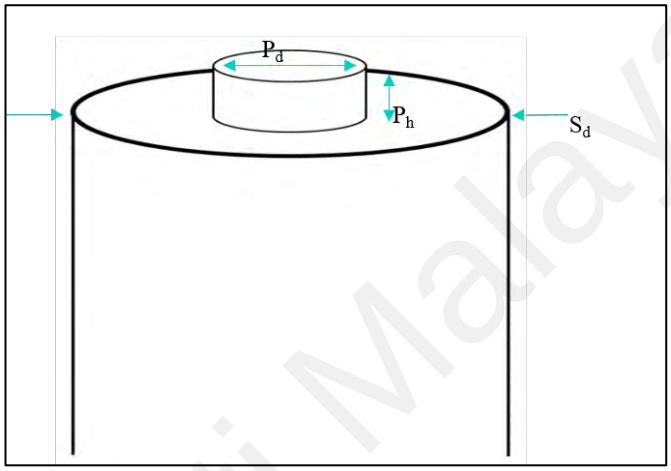


**Figure 3.10: Illustration of FSA tool**

The shape of the tool is considered fairly simple hence manufacturing it in-house as possible was done to save costs. A rod of tungsten carbide (length - 100 mm and diameter – 12 mm) was purchased and cut into two equal-length pieces (50 mm each). Tungsten carbide has very high hardness and is very abrasion resistant, hence its widespread use as a cutting tool (and as an FSW tool), but due to these factors machining tungsten carbide is challenging. The rod was cut to length using electric discharge machining (EDM).

After being cut to length, the tool was clamped onto the chuck of the rotary table. The rotary table was placed on the bed of the surface grinder. The tool was slowly processed according to the required dimensions with a diamond grinding wheel to achieve a pin with a height of 1.3 mm, and a pin diameter of 4 mm, as shown in Figure 3.11.

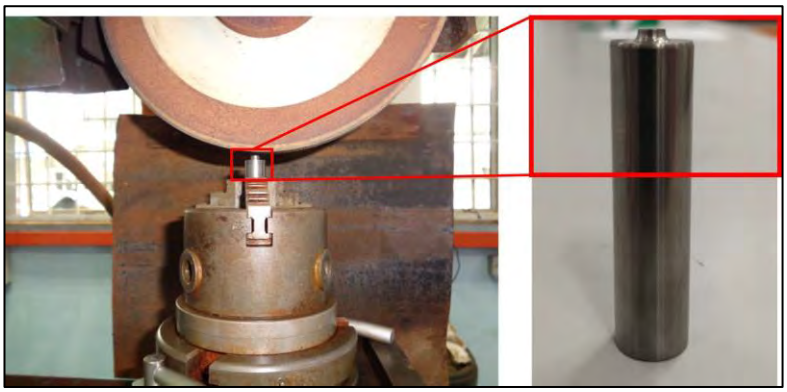

**Figure 3.11: Processing of FSA tool**

## 3.5 Friction stir alloying process experimental setup

Manford VL-610 vertical CNC milling machine was used for experimentation. The router bed (machine part on which the workpiece is clamped) has t-slots. The slots were measured as the fixture was designed to fit onto the base. The fixture base was placed on the CNC bed, and their holes were aligned to allow the clamping screws to pass through. The base was then held down with the screws and t-slot nuts. The plates were placed in their designated space, and a gap of 0.2 mm thickness was created at the faying surface of the workpiece plates. When needed, the additives were injected into the gap with a syringe. The pneumatic clamp was used to clamp the workpiece. The advantage of the pneumatic clamp over conventional nut and bolt arrangement is uniform pressure distribution and ease to clamp-unclamp. Argon is used to protect welded zone and tools from oxidation. It also helps to keep the tool cool after finishing each experiment. Figure 3.12 illustrates the experimental setup used in this study.

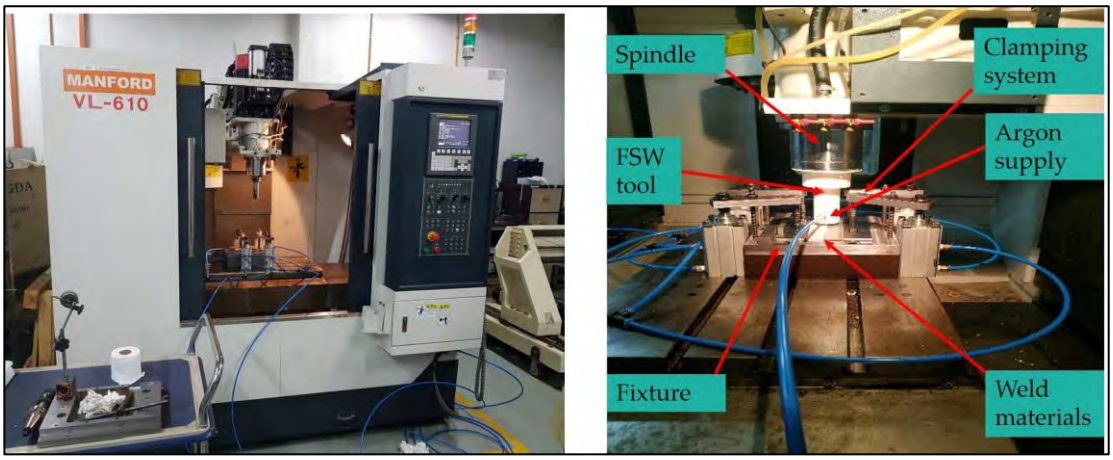


**Figure 3.12: Image of experimental setup**

## 3.6 Friction stir alloying of AZ31 and mild steel with Al-Mg as an additive

The specimens for the FSA consist of a pair of metal workpieces of AZ31 Mg alloy and mild steel, with each plate a length of 200, a width of 50 mm and a thickness of 1.5 mm. FSA was conducted using a tungsten carbide cylindrical tool with a shoulder diameter of 12 mm and a non-threaded 1.3 mm probe diameter of 4 mm. The rotational speed was kept constant at 500 RPM, and the traverse speeds were varied at 25, 50 and 100 mm/min. The zero offset is defined as the position where the probe plunges into the AZ31 workpiece and its side just touching the butt face of mild steel. A plus (+) offset is obtained as the position of the probe moves horizontally across the mild steel workpiece, as illustrated in Figure 3.13. The tool offset was kept as 1 mm into steel in the current study. The mild steel workpiece was kept at the advancing side and AZ31 at the retreating side of the process.

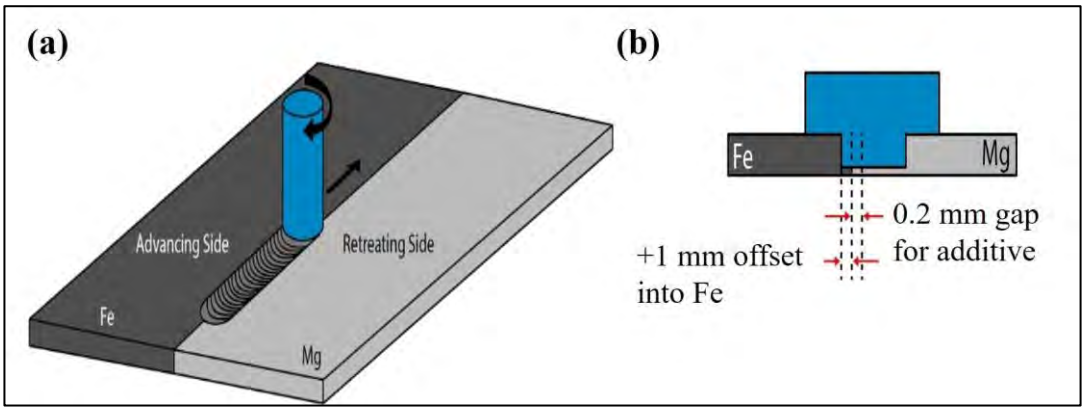


**Figure 3.13: Schematic illustration of (a) FSA process (b) tool offset into steel**

Before the welding process, the Mg-Al powder additive was injected into the gap between AZ31 and mild steel, as shown in Figure 3.14. Table 3.3 lists the details of the experiment, demonstrating the variations in the welding speeds and the weight per cent (wt.%) of the metal composition selected for each experimental run.

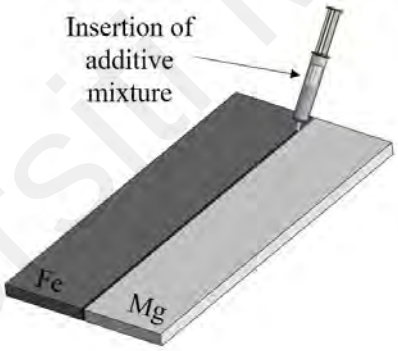


**Figure 3.14: Schematic for injection of additives into the gap**

**Table 3.3: Details of FSA experimental conditions for AZ31 and mild steel using Al-Mg as an additive**

| FSA condition | Value |
|---|---|
| Tool rotation (rpm) | 500 |
| Tool offset (mm) | 0.5 |
| Probe length (mm) | 1.3 |
| Probe intrusion depth (mm) | 1.4 |
| Welding speed (mm/min) | 25, 50, 100 |
| Material thickness (mm) | 1.5 |
| Powder type and percentage (wt.%) | 6.0 Al and Mg (balance), 10.0 Al and Mg (balance), 15.0 Al and Mg (balance) |
| Powder average diameter (μm) | 45 |

### 3.7 Friction stir alloying of AZ61 and mild steel with Al-CNT as an additive

In the FSA of AZ61 and mild steel with Al-CNT additive, mild steel was kept at the advancing side and AZ61 at the retreating side. A 1 mm offset into mild steel was maintained during the FSA process. A tungsten carbide cylindrical tool with a non-threaded probe was used for the FSA. The tool shoulder was 12 mm in diameter with a 1.3 mm tool probe in length. The probe diameter was 4 mm. The traverse speeds were changed between 15, 30, and 50 mm/min, keeping the rotating speed constant at 1500 RPM. Prior to the FSA process, the Al-CNT was placed in the 0.2 mm gap between the AZ61 and mild steel plates. Table 3 summarises the process parameters, including welding speed differences and the weight per cent (wt.%) of the CNT composition employed in experimentation. The schematic of the experiment is similar to the AZ31 and mild steel process and is illustrated in Figures 3.13 and 3.14.

**Table 3.4: Details of FSA experimental conditions for AZ61 and mild steel using Al-CNT as an additive**

| FSA condition | Value |
|---|---|
| Tool rotation (rpm) | 1500 |
| Tool offset (mm) | 1.0 |
| Probe length (mm) | 1.3 |
| Probe intrusion depth (mm) | 1.4 |
| Welding speed (mm/min) | 15, 30, 50 |
| Material thickness (mm) | 1.5 |
| Additive type and percentage (wt.%) | Aluminium with CNT 1%, 3% and 5% |
| Aluminium powder average diameter (μm) | 45 |
| Diameter of CNT dimension (nm) | 50-80 |

### 3.8 Microstructural characterization

Numerous characterisation methods were applied for the extensive analysis of microstructures in this work. Optical microscope (OM), Scanning Electron Microscope (SEM), energy dispersive spectroscopy (EDS), and transmission electron

microscopy (TEM) were used to examine FSA processed samples. X-Ray Diffraction (XRD) was also used to perform phase analysis on the samples.

### 3.8.1 Metallography

Samples were cut using a wire electrical discharge machining for metallographic analysis. The samples were then prepared using standard metallographic procedures. The samples were polished with various grades of emery paper (P800 - P5000) using the polishing machine model Metapol-2 Rax Vision, as shown in Figure 3.15. After that, alumina with 0.5 µm particle size was used to polish the using polishing cloth. De-ionized water was used during the polishing process. After that, the samples were soaked in ethanol. Finally, the polished samples were etched in a 5% Nital solution to unveil morphology details.


**Figure 3.15: Polishing machine**

### 3.8.2 Optical microscopy

The optical microscopic view of samples was observed with Olympus (Origin- Tokyo, Japan) optical microscope, as shown in Figure 3.16. The grains of samples were observed using various magnifications.

**Figure 3.16: Optical microscope**

### 3.8.3 Scanning electron microscope (SEM)

Figure 3.17 shows an SEM (Model: Hitachi, SU8030) used to characterise the materials. To get the best image, the SEM voltage was changed from 5 to 15 keV. Images of secondary electrons (SE) were captured in samples. The specimens' elements were mapped using an energy dispersive spectrum (EDS).

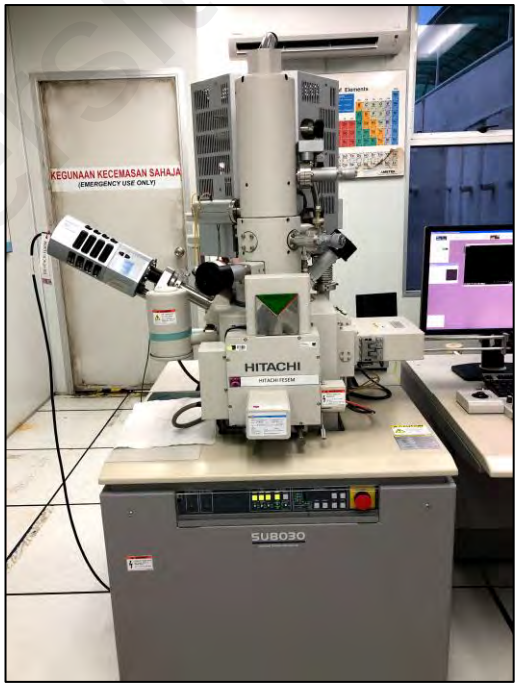


**Figure 3.17: Scanning electron microscope**

### 3.8.4 Transmission electron microscopic (TEM)

#### 3.8.4.1 Sample preparation

The thin lamella for transmission electron microscopic (TEM) was prepared using FEI Helios Nanolab 650 dual focused ion beam (FIB) instrument, as shown in Figure 3.18.

**Figure 3.18: Dual-focused ion beam machine for lamella preparation**

Steps to prepare the thin lamella, less than 100 nm thickness, by using a dual-beam for TEM analysis from the Mg/Fe interface are presented in Figure 3.19. Figure 3.19 (a) shows the interface of Mg/Steel from which lamella is planned to extract. Figure 3.19 (b-d) shows making trench all around the interface with ion beam bombardment. Using the platinum welding technique, a needle was used to pick up the lamella from the trench (Figure 3.19,e). After that, lamella was placed on a copper grid and welded to the copper grid using a platinum tool was performed. The thickness of lamella for TEM analysis after slicing was 100 nm.

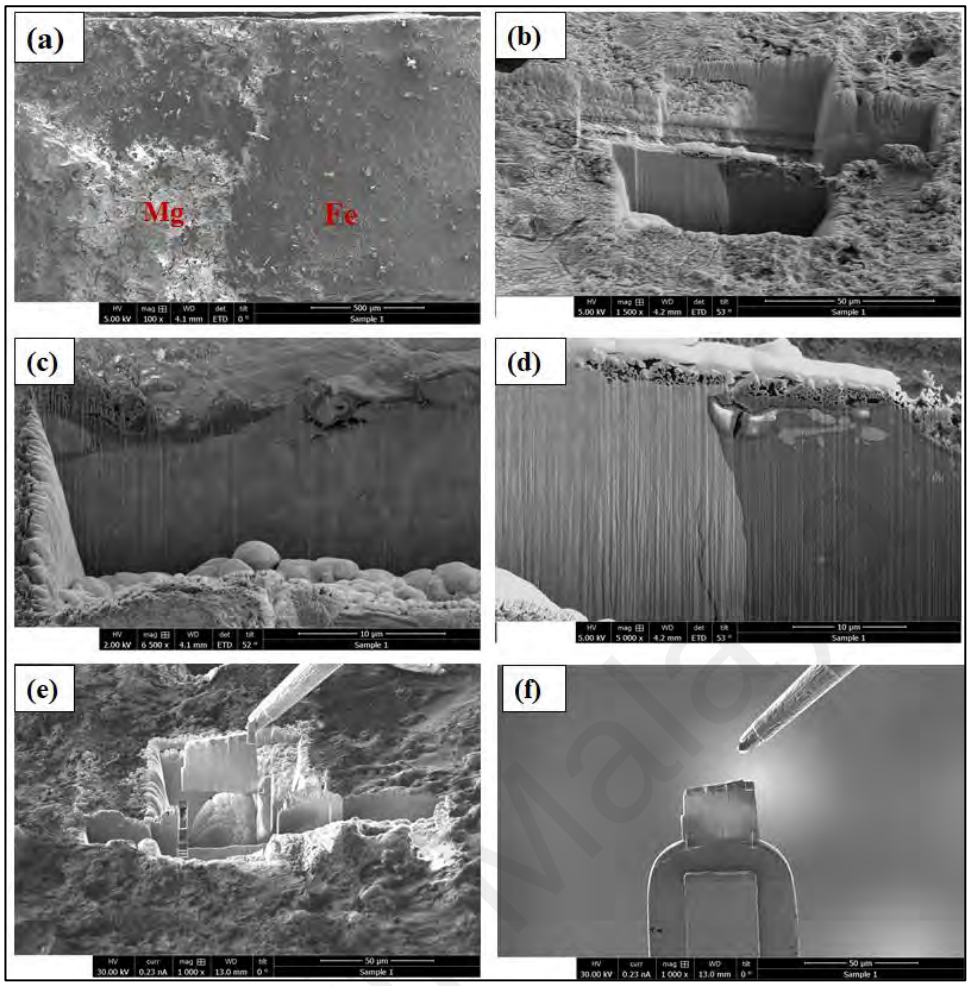


**Figure 3.19: Lamella preparation using dual-beam from the interface of Mg/Fe (a) Mg/Fe interface (b-d) digging of trench all around lamella (e) picking up of lamella (f) lamella mounted on a copper grid**

### 3.8.4.2 TEM analysis

TEM-EDS analysis was performed using FEI Tecnai G2 F20 TEM. The TEM machine was equipped with EDX. TEM imaging was performed at 300 kV accelerating voltage. EDX analysis was performed at different locations to know about elemental composition at the nanoscale level. Figure 3.20 shows the TEM machine image.

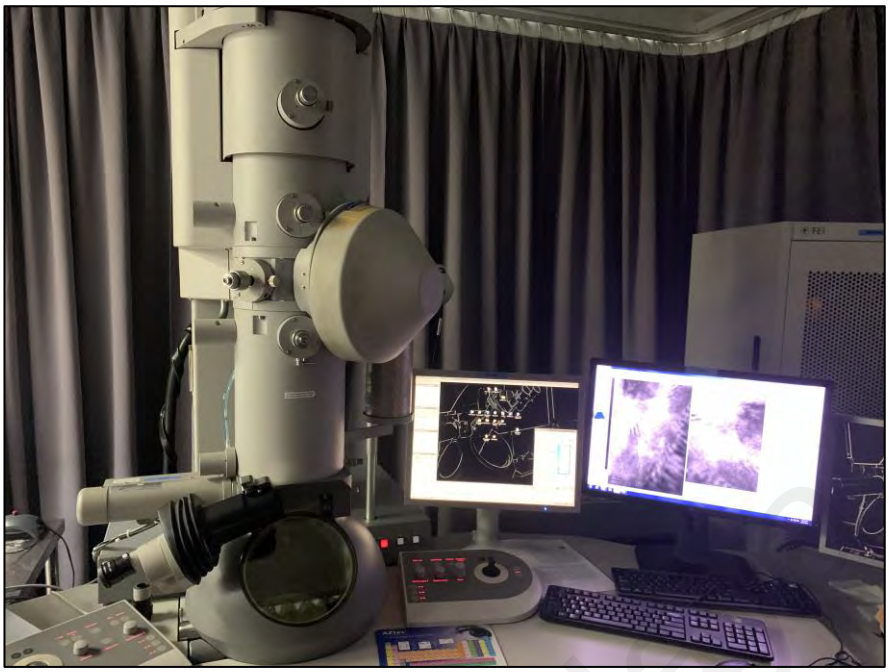

**Figure 3.20: FEI Tecnai G2 F20 TEM for TEM imaging**

### 3.8.5 X-ray diffraction analysis (XRD)

IMC phase identification was performed by XRD machine (Make- PANalytical Empyrean), as shown in Figure 3.21. The diffraction angle range was from 20º to 80º. Raw data was post-processed using Xpert Highscore software and matched with the JCPDS data card.

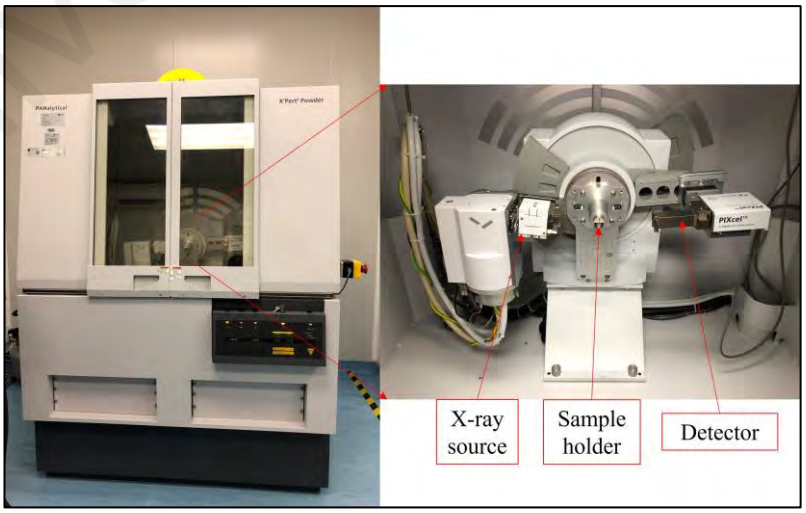


**Figure 3.21: XRD machine**

## 3.9 Mechanical tests

### 3.9.1 Tensile test

Tensile strength evaluation was performed on flat dog-bone-shaped welded sample pieces. The standard tensile test specimen followed by ASTM E8 was cut using a wire EDM machine. The standard tensile test specimen and wire EDM cut specimen is shown in Figure 3.22.

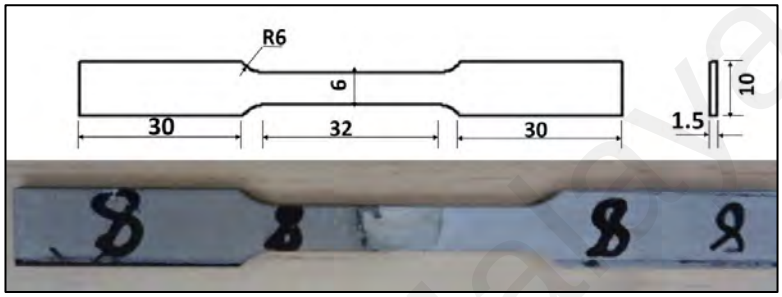


**Figure 3.22: Tensile test standard dimensions and wire EDM cut sample**

The tests were carried out using a universal testing machine (INSTRON model 3369) at a pull rate of 0.5 mm/min transverse to the welding direction, as shown in Figure 3.23. Three specimens for tensile testing were prepared for each joint condition. The average value of the tensile test for each condition is considered for analysis.

**Figure 3.23: Universal testing machine**

### 3.9.2 Microhardness test

Model HMV 2T E Vickers microhardness tester was used to measure hardness at the cross-sectional area of the specimen. Hardness tests were performed using diamond indenter pyramidal in shape with a load of 200 g for a dwell time of 5 seconds. Mirror polish samples were used for microhardness tests. Figure 3.24 shows the microhardness tester used in the study.

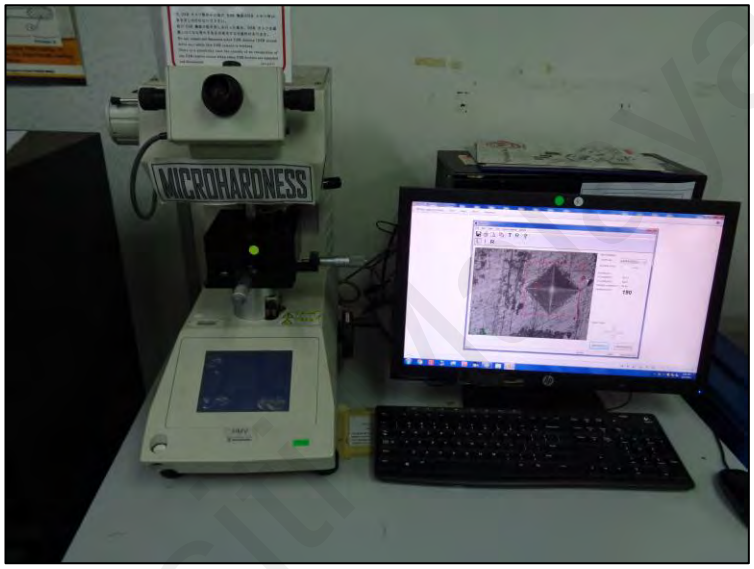


**Figure 3.24: Microhardness tester**

### 3.9.3 Safety guidelines followed during experimentation

Due to the robust nature of the experimental work, which includes heavy clamping and a high-speed milling machine, safety protocols were followed during experimentation.

a) The modified FSA machine must be operated with at least two people.

b) The experimental work was performed using the lab apron with full sleeves and shoes.

c) The safety guidelines prescribed by university authorities, such as handling heavy equipment carefully during pandemic social distancing, followed and handling sophisticated instruments carefully during the experiment and analysis.

# CHAPTER 4: RESULTS AND DISCUSSION

## 4.1 FSA of AZ31 and mild steel with Al-Mg as an additive

### 4.1.1 Appearance of the welded joint

All welded joints had good surface appearances with no flash produced. Figure 4.1 shows the variations of surface appearances with the additions of Al-Mg metal powders for a welding speed of 50 mm/min. The surface of the joint became sound when Al-Mg powder was added, as shown in the comparison between Figure 4.1 (a) with Figure 4.1 (b) and Figure 4.1 (c). However, the high content of Al would result in a rough surface appearance, as shown in Figure 4.1 (d), which is presumed to be due to improper mixing of the increased volume of Al powder. Finally, no defects, such as pores, voids or tunnels, were found in all the joints; however, Figures 4.1 (b) and (c) contain cracks at the weld's surface at the upper layer only.

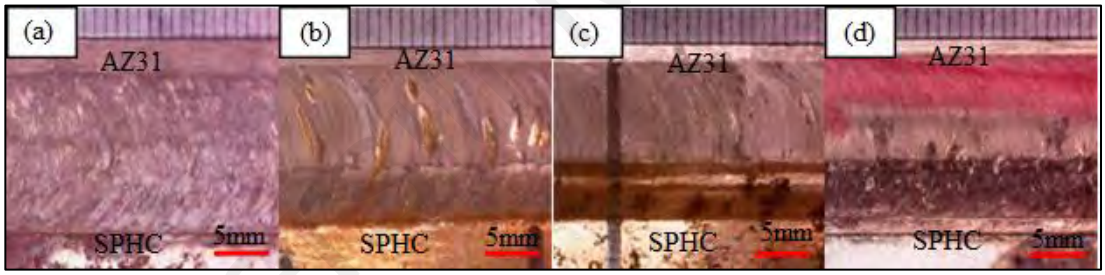


**Figure 4.1: The surface appearance of dissimilar friction stir alloy process between AZ31 and mild steel (a) no powder, (b) 6 wt.% Al and Mg (balance), (c) 10 wt.% Al and Mg (balance), (d) 15 wt.% Al and Mg (balance)**

### 4.1.2 Cross-sectional microstructure observation

Figure 4.2 shows optical microscope images of the specimen with 10 wt.% aluminium. We can see base AZ31 and mild steel grains in Figures 4.2 (a) and 4.2 (d), respectively. Base AZ31 is typical equiaxed grain, whereas mild steel grain can be seen as it consists of ferrite grain due to low carbon content. Figures 4.2 (b) and 4.2 (c) are AZ31 and mild steel stir zone microstructure. It can be seen that the stirring action of the tool severely deforms both AZ31 and mild steel side grains. The microstructure at the stir zone is more refined as compared to the base material.

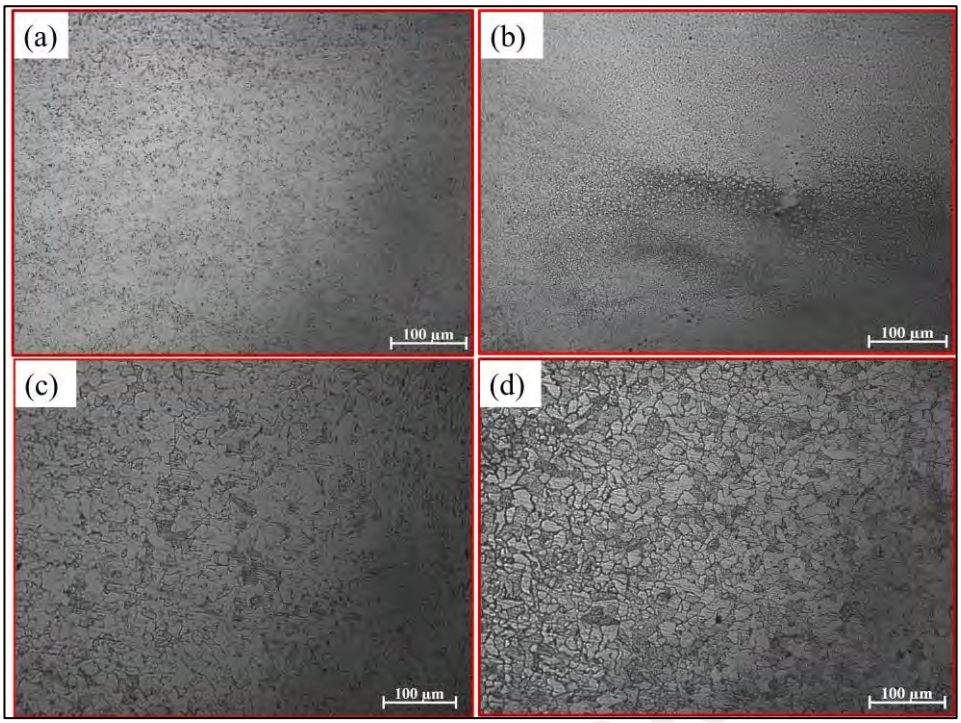


**Figure 4.2: Optical microscopic image of 10 wt% Al specimen (a) base AZ31 (b) stir zone from AZ31 side (c) stir zone from mild steel side (d) base mild steel**

Figure 4.3 shows the cross-sectional images of friction stir welded AZ31/mild SPHC mild steel joint at different welding conditions. In general, sound joints without defects were obtained using FSA. At lower welding speeds of 25 and 50 mm/min, as shown in Figures 4.3 (a) and 4.3 (b), significant mechanical interlocking with bent structures can be observed. Such interlocking would promote a stronger joint and results in higher tensile strength. However, in Figure 4.3 (d), a lower strength is probably due to the agglomeration of Al particles at the bottom of the gap. The tensile strength is depicted in the upcoming section. The mechanical interlocking structures are less seen in the specimen in Figure 4.3 (c) despite the highest strength recorded. This phenomenon remains unexplained in terms of observation by SEM capability. The combinations of powder additives weight percentage and welding speeds have affected the joint's physical features and mechanical properties.

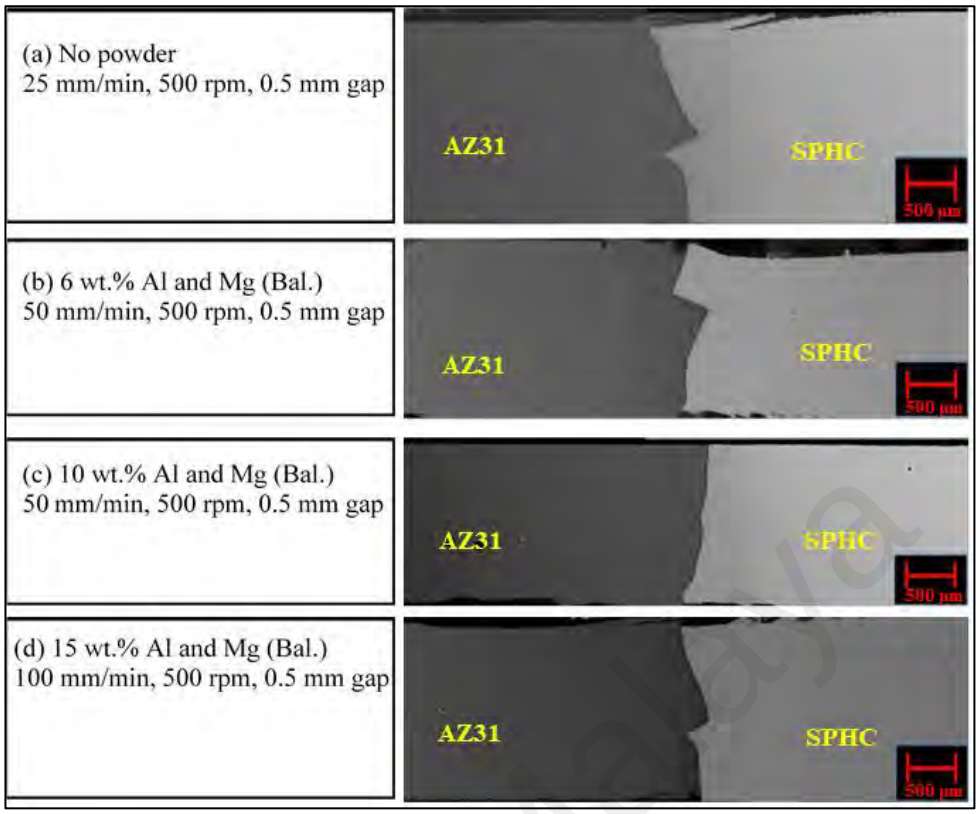


**Figure 4.3: Macroscopic images of the interfaces on the cross-section under different welding conditions (a) No powder (b) 6 wt.% Al (c) 10 wt.% Al (d) 15 wt.% Al**

Figure 4.4 and Figure 4.5 shows the SEM-EDS image taken at the interface of AZ31/SPHC mild steel joint with 10 wt.% Al and Mg (balance) powder additives at 50 mm/min welding speed. In Figure 4.4, five measurement points were taken across the welding interface to show the distribution of elements along the cross-section. Al and Mg powder elements can be observed near the interface on each side of two base materials, indicated by points 3 and 4. At point 3, proper mixing of powder additives and the base materials can be observed. Al and Mg powder additives were well dispersed at the interface, allowing interaction with the base materials elements. It can also be observed at points 3 and 4 that all three elements, magnesium, aluminium and iron, were present. From these two points, one can depict that intermetallic compounds could have formed resulting from the interactions of the powders with the base materials and heat generated from the FSW process.

As the magnesium-iron system is immiscible due to their weak interactions, Al alloying element in AZ31 and Al powder additive was expected to interact with the iron element in SPHC mild steel. Besides, interactions between powder additives and alloying elements present in AZ31 base materials might also induce the formation of IMC. However, the capability of IMCs detection is limited at 1 μm resolution with SEM spot analysis across the interface. Therefore, at this stage, no IMCs are detected. For investigation of whether IMCs are formed or not, TEM analyses were performed at nanometre (nm) resolution level and discussed in the following paragraphs.

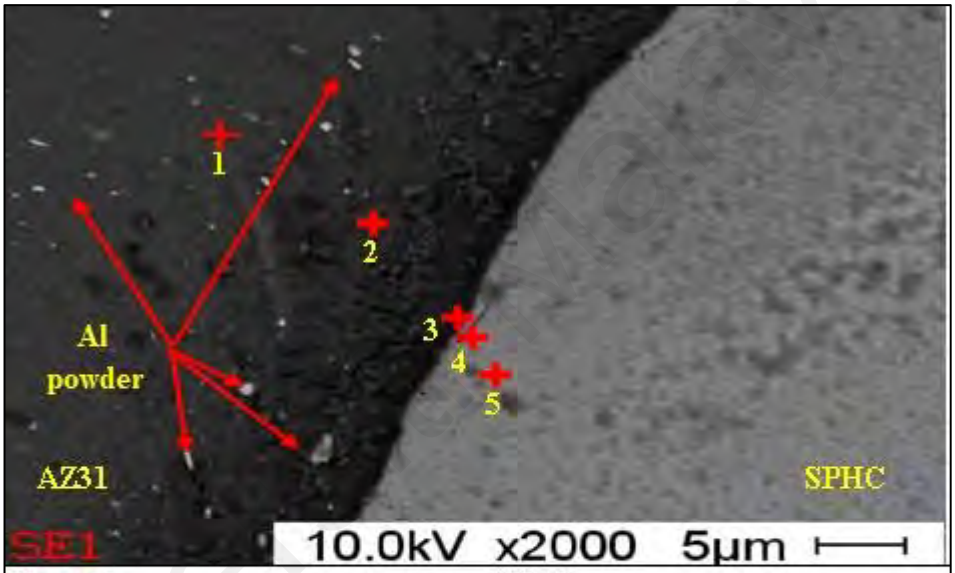


| Element | Wt.% | | | | |
|---|---|---|---|---|---|
| | Point 1 | Point 2 | Point 3 | Point 4 | Point 5 |
| Mg | 93.26 | 80.88 | 26.99 | 4.57 | 3.15 |
| Al | 4.44 | 6.29 | 7.77 | 1.26 | - |
| Fe | - | - | 14.69 | 86.61 | 86.32 |
| O | 2.30 | 12.83 | 20.54 | 4.29 | 4.32 |

**Figure 4.4: Analysis of elemental composition at different locations on the FSW for 50 mm/min with powder additives of 10 wt.% Al and Mg (balance)**

From Figure 4.4, it can also be observed that at point 3 near the interface, the oxygen content is high. This oxygen content existed in the form of a MgO layer at the AZ31 sheet prior to welding (Wang et al., 2020). During welding, some of the portions of MgO detached from the layer and existed in the form of MgO particles.

Figure 4.5 shows EDS mapping of the interface cross-section, which depicts the intensity of aluminium particles more into the magnesium side. It is evident that the magnesium alloy already has aluminium content as alloying elements. This intensity supports evidence from Figure 4.4, which also found increased aluminium content.

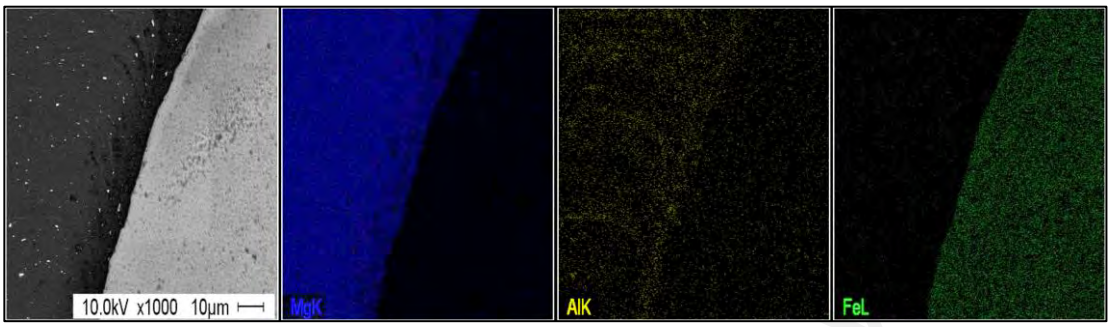


**Figure 4.5: SEM images and EDS mappings of the interfaces on the cross-section at 50 mm/min welding speed with 10 wt.% Al and Mg (balance)**

The successes of FSW in welding dissimilar materials have been reported in recent studies. However, interactions between dissimilar materials could produce the IMCs layer at the interface of the joint, which could improve the tensile properties and fracture behaviour significantly. In the FSW of AZ31B and Al6061, significant amounts of brittle intermetallic compounds of $Mg_2Al_3$ and $Mg_{17}Al_{12}$ were found near the interface (Dorbane, Mansoor, Ayoub, Shunmugasamy, & Imad, 2016). These IMCs would create brittle zones for crack propagation to initiate. It was mentioned that the IMC formed was strongly dependent on the heat input resulting from the welding parameters, and the stirred zone was identified as the most likely location for IMC formation due to the highest temperature recorded within this location (Yi et al., 2016). In the FSW of aluminium to mild steel, the IMCs formed in the weld zone have been identified as $Al_6Fe$ and $Al_5Fe_2$ (Pourali et al., 2017a). It was also mentioned that increasing the welding speeds would decrease the IMC layer, thus resulting in higher tensile strengths. Nevertheless, the Fe-Al intermetallic compound should be thin enough to restrain fracture at the intermetallic compound (Mao & Bell, 1979). However increase in thickness of IMCs lead to deterioration of the tensile strength of the joint (Jiang & Kovacevic, 2004). The necessity of IMCs also investigated

in the FSW of immiscible Mg and steel (Kasai et al., 2015a). In this study, it was found that an aluminium depletion region has developed near the interface. Al in Mg is used for the creation of the intermetallic compound Fe-Al. The improved tensile strength of joints attributed that the development of thin IMC at the interface is essential to producing sound steel/magnesium joints. The joint strength of steel/magnesium improved with an increasing aluminium content of magnesium alloy and a thinner intermetallic compound layer. Furthermore, researchers studied IMCs formation due to reactive elements present in the base material (Wang et al., 2019). They observed that interdiffusion took place between alloying elements in magnesium alloys and stainless steel, diffused to the welded interface to form an Al-rich zone and further formation of Al-Fe IMCs. Further joint strength analysis concluded that the presence of IMCs at the welded interface could also facilitated joint strength. Furthermore, FSW of Al-1050 and low carbon steel reveals multiple phase IMCs formation as $Al_{13}Fe_4$ and $FeAl_3$ (Abd Elnabi et al., 2020). In another study author observed Fe-rich IMCs FeAl and $Fe_3Al$ in joint interfaces. It was found that Fe-rich IMCs are not responsible to decrease in tensile strength of joint and defects, for instance voids, were accountable for the degraded strength (Pourali et al., 2017b). In this study, the addition of Al-Mg powder mixture has served as a metallurgical binder, increasing the joining performance due to the enhanced interaction between Al powder and AZ31/SPHC mild steel base metals.

Figures 4.6 and 4.7 shows TEM with intermetallic thickness and high-resolution TEM image of joint interface with corresponding fast fourier transformation (FFT) for welding speed 50 mm/min with powder additives of 10 wt.% Al and Mg (balance) has the highest tensile strength at different interfaces of joint. It was observed that a thin intermetallic compound formed between Al powder and Fe element of SPHC mild steel (Kasai et al., 2015a; Sun et al., 2013; Wang et al., 2019). Figure 4.6 shows high-resolution TEM and corresponding FFT of the base Mg side and base Fe side. From the figure of the FFT

diffraction ring, it can confirm that there is a crystal material present at that respective position.

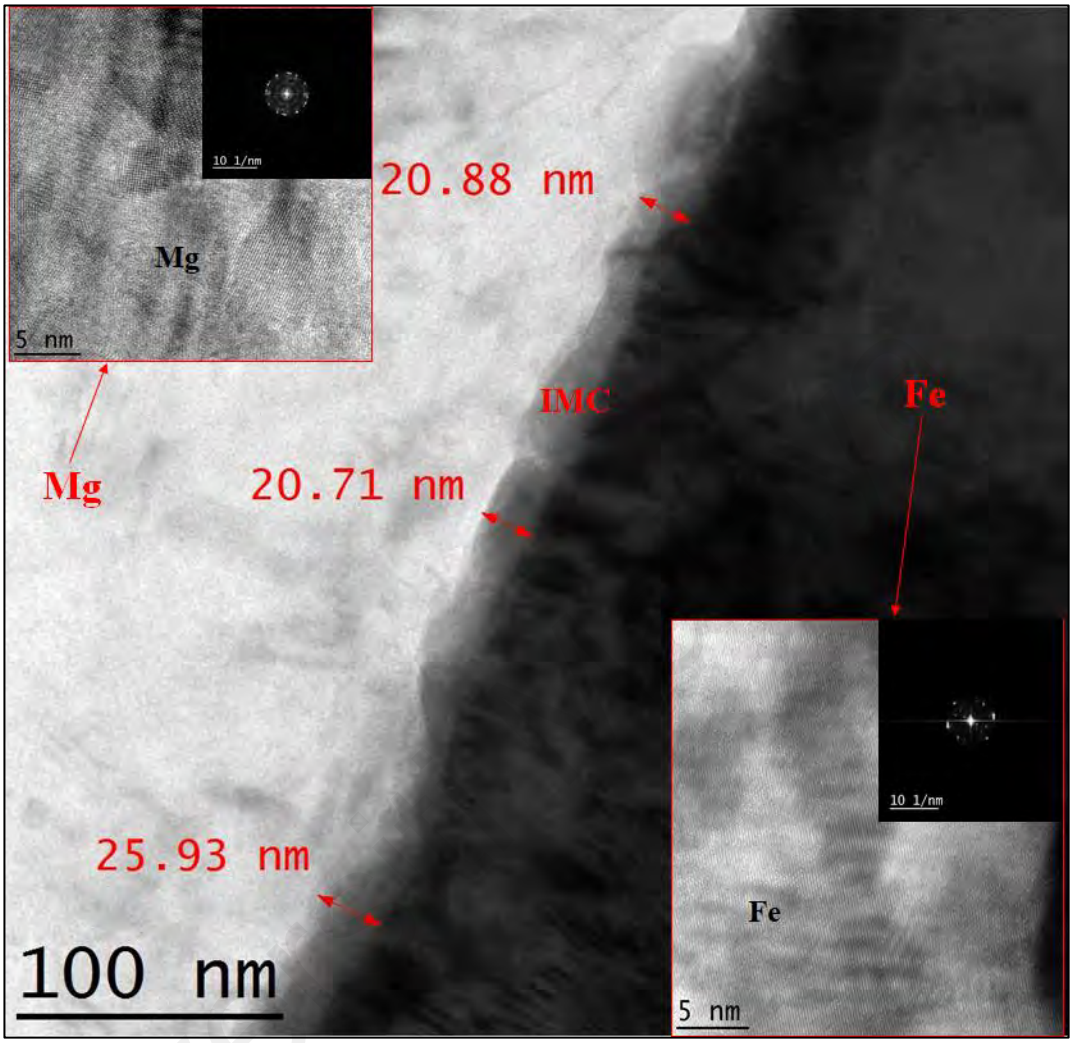


**Figure 4.6: TEM image showing the intermetallic compound (IMC) thickness and high-resolution TEM with corresponding FFT of base Mg and Fe**

Further, Figure 4.7 comprises three distinct zones of high-resolution TEM and corresponding FFT. The figure shows TEM and FFT of IMC zone, Mg/Al interface and Al/Fe interface. FFT image of IMC in inset has a broadened ring diffraction pattern, which is a characteristic of amorphous structure and leads to brittle fracture (Sun et al., 2013). This amorphous structure of IMC is also confirmed from fractography analysis which is discussed in the following subsection, in which all samples fractured from joint. However, the FFT of the rest of the two interfaces shows a diffraction ring, which depicts crystal structure.

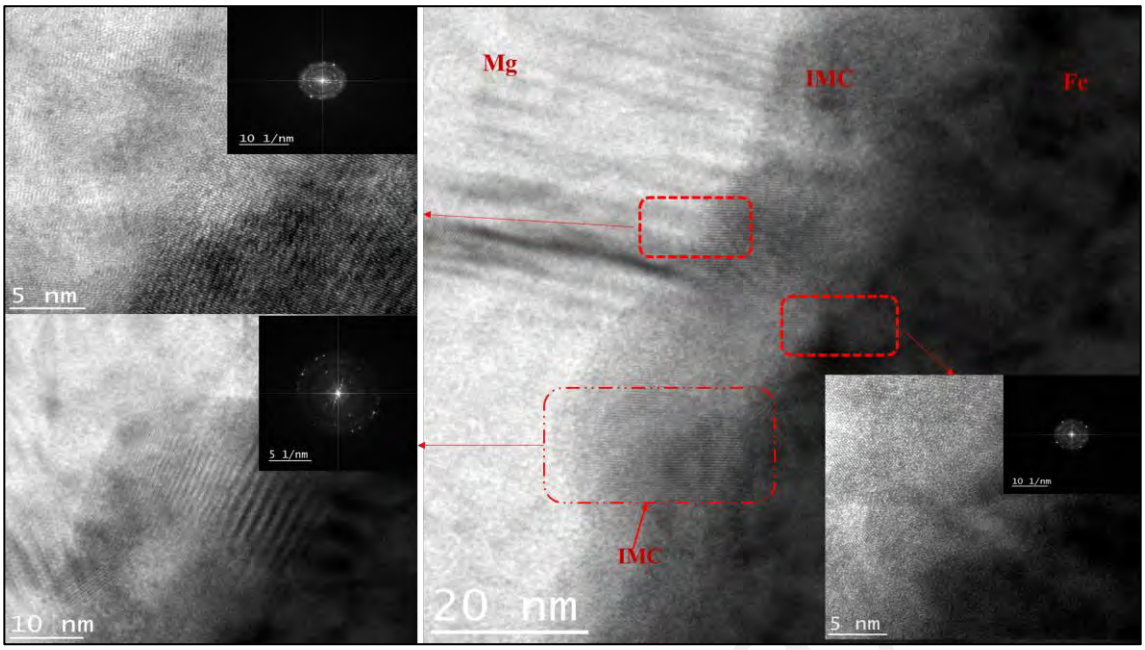


**Figure 4.7: High-resolution TEM with FFT diffraction pattern of three distinct zones; namely IMC zone, Mg/Al interface and Al/Fe interface (inset)**

The thin intermetallic compound formed between Al powder and Fe element of SPHC steel was confirmed by EDS point analysis in Figure 4.8. At interface point 3 in EDS, the Al counts and Fe counts were higher, which indicates the formation of Al and Fe intermetallic compounds. Furthermore, the IMC appeared uninterruptedly at the interface of the welding joint, and thickness was found to be almost constant irrespective of the length of the interface.

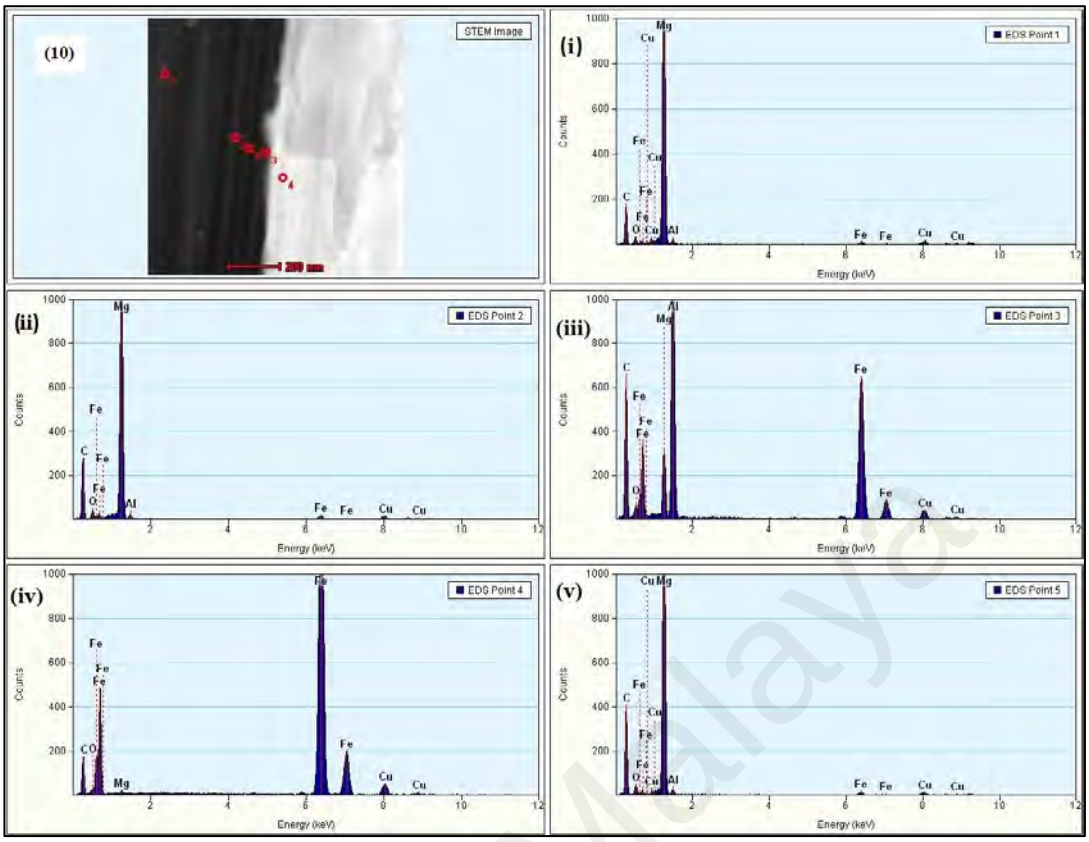


**Figure 4.8: TEM-EDS analysis at respective points across the joining interface for the specimen with 50 mm/min welding speed and 10 wt.% Al and Mg (balance)**

Figure 4.9 depicts XRD analysis of AZ31 and mild steel with 10 wt.% Al and Mg (balance) at 50 mm/min welding speed to identify IMC phases. IMC of $Al_{12}Mg_{17}$, Al-rich $Fe_2Al_5$ was detected along with the intensity of base magnesium, base steel, and magnesium oxides. The $Fe_2Al_5$ IMC from XRD analysis confirms the TEM-EDS results depicted in Figure 4.8, where at point 3 Al count and Fe count are detected (B. Fu et al., 2021). Also, from TEM-EDS, It can be noticed that Al-rich IMC is forming, which is confirmed by XRD analysis. As reported in the literature, the formation of magnesium oxide is mainly due to either reaction with atmospheric oxygen (Meng et al., 2021). In Figure 4.4, SEM-EDS presence of oxygen along with magnesium was also detected; however, from TEM-EDS, no MgO is detected. However, the formation of $Al_{12}Mg_{17}$ IMC is not detected through TEM-EDS.

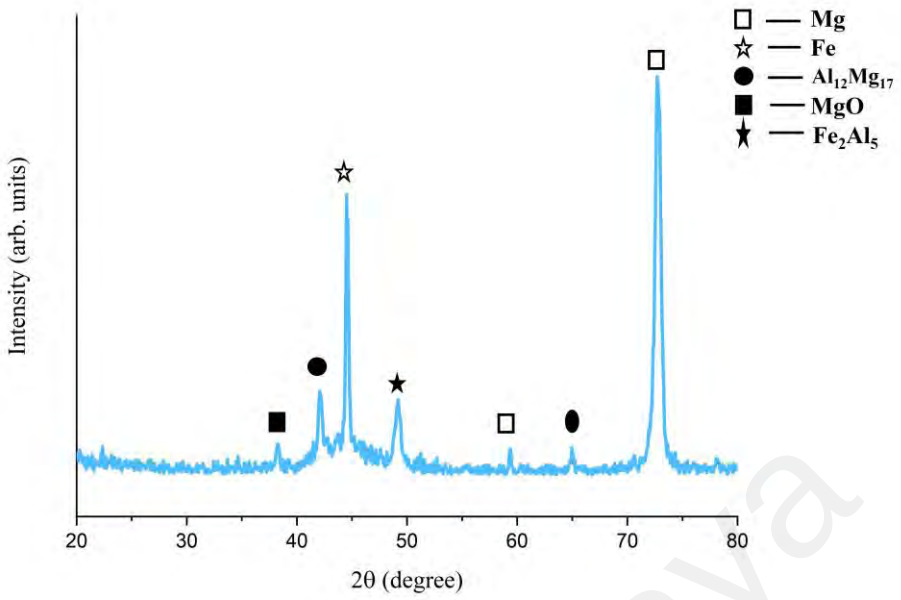


**Figure 4.9: XRD pattern of AZ31 and mild steel with 10 wt.% Al and Mg (balance) at 50 mm/min welding speed**

### 4.1.3 Effect of welding speed on tensile strength

Figure 4.10 shows the effect of welding speeds on tensile strengths of the FSW specimens, with and without powder additives. Generally, the addition of metal additives of 6 wt.% Al and Mg (balance), and 10 wt.% Al and Mg (balance) has resulted in increased tensile strengths as compared to specimens without powder additives at increasing traverse speeds from 25 mm/min to 50 mm/min. The highest tensile strength of 150 MPa was achieved for the specimen with powder additives of 10 wt.% Al and Mg (balance) at a welding speed of 50 mm/min. This tensile strength value is 17% better than its equivalent specimen without powder additives. The reason for the lower strength of welded specimens without additives can be explained as magnesium and iron are immiscible, and oxides of magnesium (MgO) at the surface of AZ31 prevent reaction between Mg alloys and steel (Wang et al., 2020). Increasing the welding speed to 100 mm/min has caused a significant decrease in the tensile strength of specimens with 6 wt.% Al and Mg (balance) and 10 wt.% Al and Mg (balance) as compared to the specimen without powder additives, which could have been caused by the improper stirring of metal additives at high welding speeds. Increasing the percentage of aluminium to 15 wt.% has resulted in a decrease of

tensile strength for all welding speeds and is lower than their corresponding non-powder added joints. The high Al powder content could have hindered the uniform dispersion of the powders at the interface during welding.

In conclusion, the addition of Al-Mg powder additives in small quantities (less than 10 wt.%) and welding with low welding speeds would improve the tensile strength of AZ31 magnesium alloy and SPHC mild steel. The highest tensile strength of welded specimen with powder additives was 62.5% better than the tensile strength of AZ31 and 41.5% better than that of SPHC. This result indicated that the joint had achieved a good weld performance. In the dissimilar joining of AZ31 and SPHC steel, there is a mismatch between elastic modulus which further leads to stress localization, in other words, stress concertation. Al-Mg Additives serve as strengthening particle which strengthens the Mg side of the joint locally. Because of the working mechanism of strengthening particle stress concentration at the interface, relived and subsequently enhanced joint strength is achieved (Lei et al., 2018; Liu & Qi, 2010; Song et al., 2012; Wang et al., 2020).

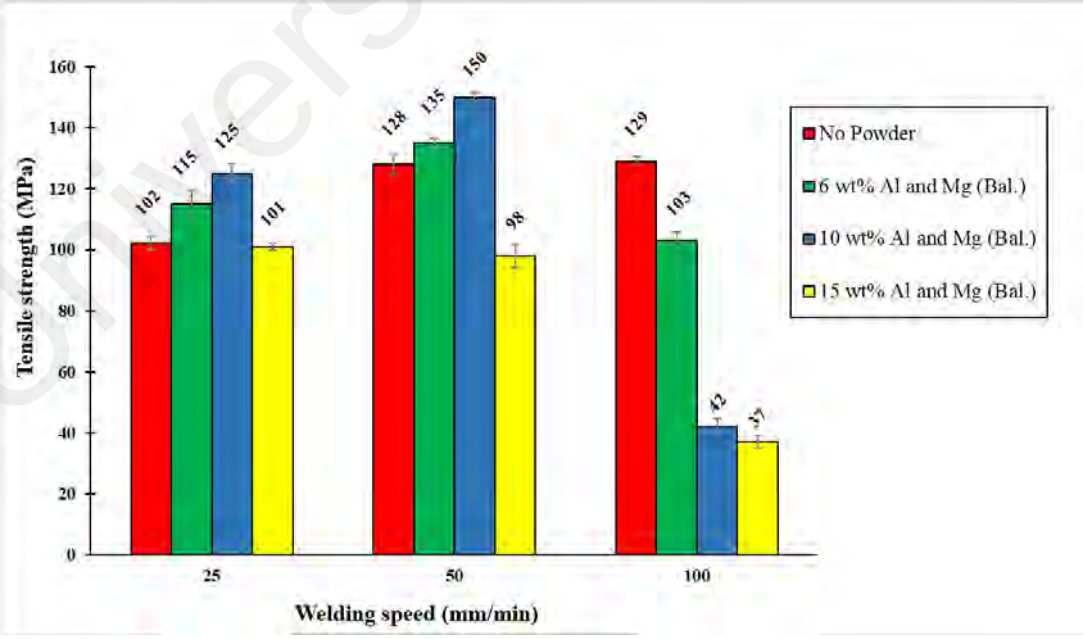


**Figure 4.10: Joint strength for different welding speeds and Al powder percentage**

### 4.1.4 Hardness assessments

Figure 4.11 shows hardness results measured along the cross-section of the welded joint, with and without powder additives. The measurements were recorded across these welding regions: stirred zone (SZ), thermomechanical heat affected zone (TMAZ), heat affected zone (HAZ), and base metal (BM). The variation in the hardness value corresponds to the distinct microstructural zones. The inherent material properties of AZ31 magnesium alloy and mild steel exhibited two specific hardness profiles of advancing (AZ31) and retreating (SPHC) sides. The highest hardness value was recorded at the interface in the SZ zone, which indicates the brittle behaviour of the joint. The hardness value at the SZ sharply decreased towards the TMAZ/HAZ at AZ31 advancing side as compared to the TMAZ/HAZ at mild steel retreating side, as the hardness value of steel is higher than that of magnesium.

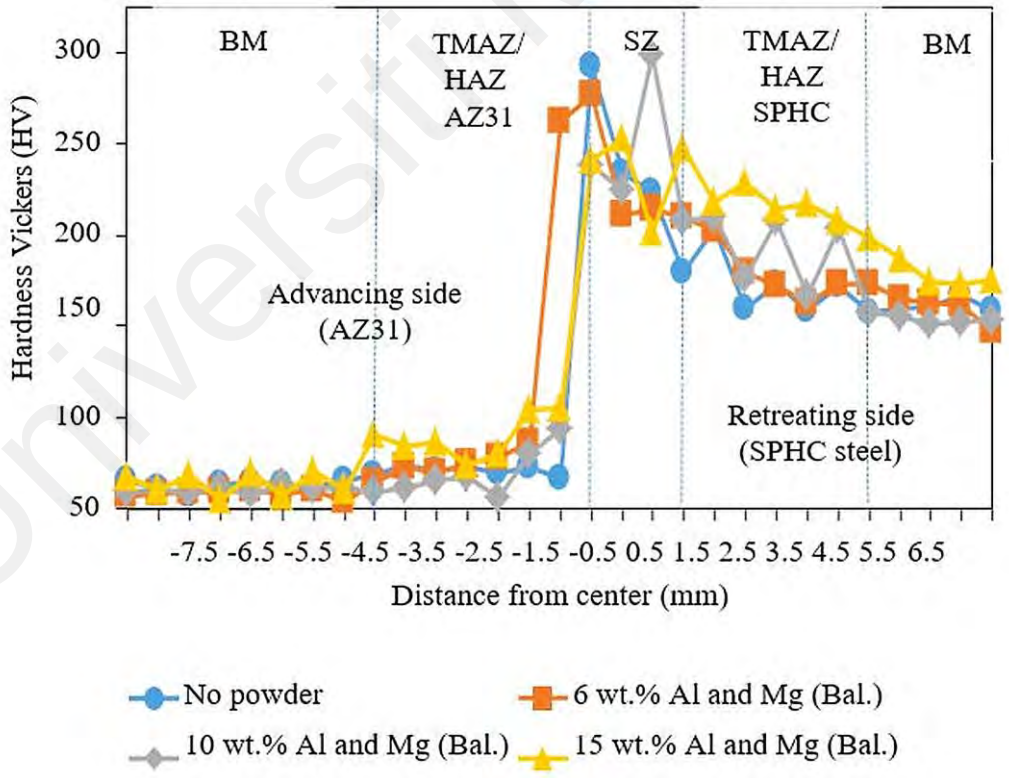


**Figure 4.11: Hardness measurement of welded joint at a welding speed of 50 mm/min**

## 4.2 FSA of AZ61 and mild steel with Al-CNT as an additive

### 4.2.1 Functionalisation of CNT

CNTs are considered great reinforcement nano-additive among carbonaceous nanomaterials because of their excellent properties (Luca et al., 2017). Composite properties enhanced with carbon nanotubes should have significant characteristics to be used in many applications, such as lightweight, strong materials for use in harsh conditions successfully (Coleman et al., 2006). The resulting characteristics of composites reinforced with CNTs are greatly influenced by their dispersion in the matrix, limiting the use of CNTs as reinforcement additives. Due to strong Van der Waals forces, the CNTs tend to agglomerate in bundles and show a very little or negligible affinity for other materials (Ma et al., 2010). To overcome the issues mentioned above related to CNTs, CNTs subjected to chemical functionalization prior to use in the FSA process in the current study.

Several functional groups allow attaching with carbon atoms in the chemical functionalisation process. These attached functional groups enhance the affinity of CNTs with non-graphitic materials (Balasubramanian & Burghard, 2005; Banerjee et al., 2003; Hirsch & Vostrowsky, 2005). In the current study, the CNTs are functionalized with sulfonitric acid. Sulphonitric acid consists of sulphuric acid and nitric acid in the 3:1 ratio (Pavese et al., 2008). Figure 4.12, which depicts Fourier transform-infrared spectroscopy (FTIR), several functional groups are attached with CNTs. After functionalisation, CNTs were used in preparing additives with different proportion combinations with aluminium particles.

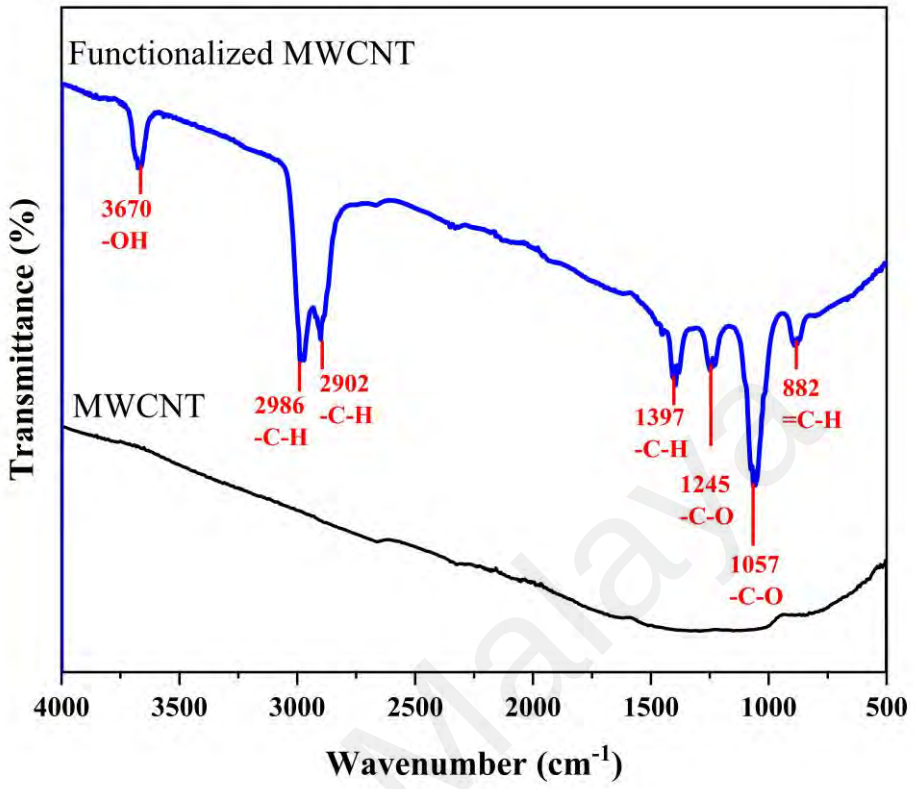


**Figure 4.12: FTIR analysis of functionalised CNT showing functional groups**

### 4.2.2 Appearance of AZ61 and mild steel joint with and without additive

The welded joints produced by the FSA technique were free from defects for welding speeds 15 mm/min and 30 mm/min. However, tunnel defects and holes were observed for 50 mm/min welding speed. Figure 4.13 the FSA of AZ61 and mild steel with 3% CNT-Al (balance) as an additive at 15, 30 and 50 mm/min welding speed. With lower tool traverse speed and the stirring action of workpiece materials happened properly. This proper stirring at sufficient heat leads to the smooth flow of materials inside the stir zone. In the case of 50 mm/min, tool traverse speed workpiece material and additive were not stirred properly. This, in turn, insufficient heat available to plasticise the workpiece material and formed a tunnel all along the weldment pathway.


**Figure 4.13: The surface appearance of dissimilar friction stir alloy process between AZ61 and mild steel at different welding with 3% CNT additive, at (a) 15 mm/min, (b) 30 mm/min (c) 50 mm/min**

### 4.2.3 Cross-sectional microstructure observation

Figure 4.14 (a)-(d) shows the optical microscopic view of samples with 3%CNT+Al (balance) with 30 mm/min welding speed at the stir zone as well as the base material. Figure 4.14 (a) depicts base AZ61 with coarser equiaxed grains. Also, in the stir zone, equiaxed grain forms with the finer grain size, Figure 4.14 (b). The AZ61 grains in the stir zone were recrystallised and converted into the equiaxed finer grain by the stirring action of the tool probe. After the passing of the tool probe, due to the unfavourable heat input state, the growth of Mg grain did not happen (Meng et al., 2021). Figure 4.14 (d) shows base mild steel grain typically in the ferrite phase. The stir zone in the mild steel side also exhibits more refined grains than the base material due to the stirring action of the tool, as shown in Figure 4.14 (c).

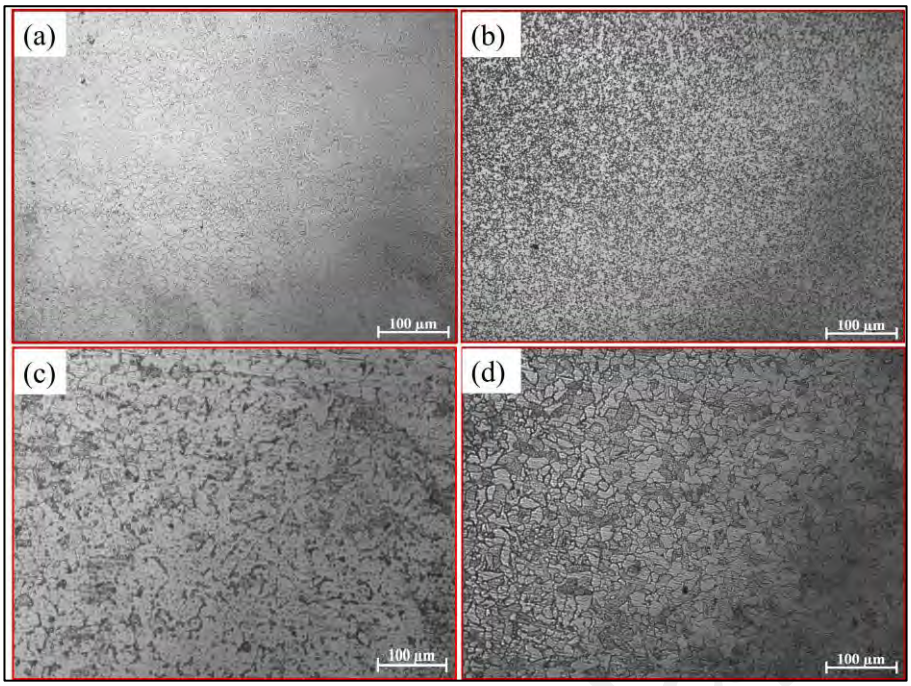


**Figure 4.14: Optical microscopic images of the specimen with (a) base AZ61 (b) stir zone of 3% CNT+Al (balance) at Mg side (c) SZ of 3% CNT+Al (balance) at mild steel (d) base mild steel**

Figure 4.15 (a) shows the joint cross-sectional macroscopic view with 3% CNT and Al (balance) at 30 mm/min welding speed. A strip of steel is flown into the Mg side and makes the hook-like structure. This also illustrates that the tool probe is not penetrating the overall thickness of the workpiece as we kept the plunge depth of 1.4 mm. Steel fragments are also visible in the magnesium side stir zone. The mechanical performance of the joint benefited from the pinning action of the strip employing mechanical interlocking.

The SEM images in Figure 4.15 (b) and (c) correspond to the two distinct zones, which are marked in Figure 4.15 (a). Figure 4.15 (b) shows the magnesium side stir zone. It can be observed that CNTs are distributed in the stir zone almost homogeneously. The precipitates of aluminium particles are also seen in the stir zone of magnesium. Figure 4.15 (c) shows the joint interface. It can be observed the CNT distribution is more in the stir zone of magnesium. Near interface precipitates of aluminium are observed. Figure 4.15 (d) shows the magnified view from the zone marked in Figure 4.15 (c). It can be

observed that near the interface, a typical lamellar structure is formed on the magnesium side. This lamellar is formed all along with the interface on the magnesium side. We performed point EDS analysis to find out the composition of the lamellar structure. It was found that composition comprises Mg 63.6 wt. %, O 27.9 wt. %, Al 8.5 wt. %. This EDS composition reveals that there is a possible formation of MgO at the interface into the magnesium side. There are studies reported about the formation of MgO in the joining of magnesium and steel. It was reported that there were two possibilities for the formation of MgO. One possibility is that atmospheric oxygen may be reacted with the stir zone during the welding process. In another possibility, the galvanic couple formed between Mg and steel during the polishing process, which started MgO formation (Fu et al., 2021; Meng et al., 2021). In the current study, argon gas shielding is used to protect the stir zone from atmospheric air reaction. However, it is observed that the cross-section area is severely affected if we keep microstructure samples in the open air during polishing. For this reason, de-ionized water is used during polishing and used ethanol at final finishing. However, the formation of MgO was ultimately unavoidable.

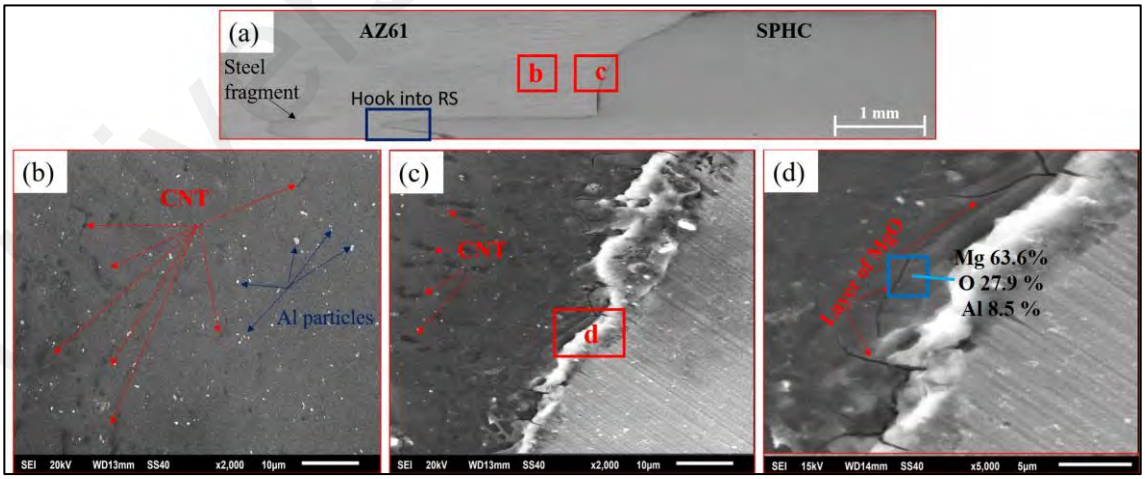


**Figure 4.15: Macro/microstructure of joint interface. (a) cross-sectional view of joint (b-c) SEM images (marked in 'a') (d) MgO formation at interface**

SEM-EDS mapping was conducted to know the dispersion of additive materials at the interface. In Figure 4.16, it can be seen that aluminium is well distributed on both sides

of the interface: magnesium and mild steel sides. The CNT distribution is more towards the magnesium side. From the distribution of CNT by observing the EDS mapping, it can be assumed that CNT is reinforcing the magnesium matrix. A fascinating finding is observed in the interface: magnesium and mild steel sides, which is the mapping of oxygen. It can be observed that oxygen is distributed along with the interface only, which verifies the galvanic coupling during polishing.

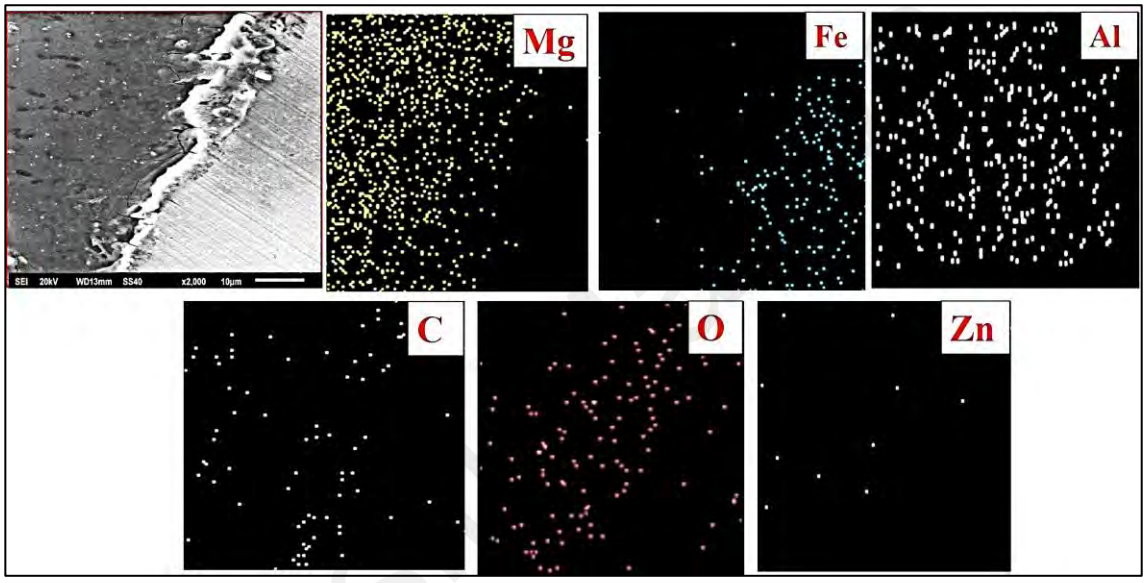


**Figure 4.16: SEM-EDS mapping of the specimen with 3% CNT+Al (balance) at 30 mm/min**

As already discussed in AZ31 and mild steel with Al-Mg additive in the FSA process, the successful joint between immiscible materials is formed when an IMC exists at the interface. The alloying elements in base materials are used to create the IMC in immiscible materials welding between magnesium alloy and steel (Kasai et al., 2015b). Therefore to control the depletion of alloying elements from base materials, they can be used as second phase particles to maintain the alloying element composition.

In the AZ31 and mild steel joining, it is already found that their Al-Mg additives help maintain the aluminium percentage in the vicinity of the joint. In the case of AZ61 and mild steel joining with Al-CNT additives, it can also assume the formation of IMC.

Several IMC formations were reported in the case of magnesium alloy and mild steel. In one study, zinc coating was stripped from galvanised steel and discovered $Fe_2Al_5$ on the steel in the base metal. They used the $Fe_2Al_5$ that remained on the base steel's surface to join with magnesium alloy (Liu et al., 2011). The AlFe IMC was reported at 44.370ºand 81.506º XRD peaks in the FSW of AZ31 and DP 600 steel. Apart from the AlFe IMC, Mg0.97Zn0.03 was also reported in the same study (Sahu et al., 2021). The aluminium, which was available as an alloying element in the AZ31 magnesium alloy, interacts with Fe, resulting in the $Fe_2Al_5$ IMC, and was advantageous for improving mechanical characteristics (Fu et al., 2021). Zhou et al. (2020) investigated the effect of Al foil addition in AZ31 and DP 600 steel using laser welding. They observed the formation of FeAl, $FeAl_2$, and $Fe_3Al$ IMCs in the weld pool.

It can be observed from immiscible material joining between magnesium and steel that joining strength is still not up to the mark of industrial application. The formation of IMCs helped in the sound joint between magnesium and steel, but this needs to be improved further from a strength point of view. The formation of various IMC, including Al-rich IMC at the interface in AZ31 and mild steel joining using Al-Mg, is observed in Figure 4.9. And the formation of IMC with improved tensile strength revealed the effective use of Al-Mg additive for IMC formation, as shown in Figure 4.10. The IMC was continuous along with the interface, as depicted in Figure 4.6.

The usage of CNT with aluminium as an additive can give an advantage over joining with only aluminium additives. Very few studies reported using CNT in FSW of dissimilar material. However, research was reported on friction stir alloying of similar materials using CNT. Researchers experimented with AZ91D magnesium alloy with CNT to make a composite using the FSA technique (Liang et al., 2017). They found that $Al_2MgC_2$ carbide was formed. They reported improved mechanical strength by using

CNT to make the composite. In another experiment, Al and CNT were used to make a composite using the powder metallurgy technique. After that, the prepared Al/CNT composite was subjected to the friction stir processing technique. The formation of aluminium carbide was revealed. Due to CNT and aluminium carbide formation, strength improvement but also improvements in ductility were reported (Li et al., 2021). The improvement in composite reinforced properties by CNT depends not only on carbide formation but also on various strengthening mechanisms.

In the current study of AZ61 and mild steel with Al-CNT as the additive is supposed to improve joint properties further apart from the formation of IMC. TEM analysis was performed to find out CNT behaviour in the current experiment.

Figure 4.17 shows TEM analysis of specimen with 3% CNT and Al (balance) at 30 mm/min. Figure 4.17 (a) shows the location from which lamella was extracted. We can see the fragment of steel on the Mg side exists. Figure 4.17 (b) shows lamella with CNT dispersed into the Mg side. The assumption for dispersion of CNT into the magnesium side only made in SEM and SEM-EDS analysis observation, as depicted in Figure 4.15 and 4.16, is almost true by looking at the TEM lamella. The formation of IMC can be observed in Figure 4.17 (c). The thickness of IMC is about 250 nm which is much higher than AZ31 and mild steel with Al-Mg additives. Also, the IMC in the case of AZ61 and mild steel is not continuous compared to the previous case. Figure 4.17 (d) shows the CNT in the magnesium matrix. The addition of CNT could be one reason behind this, as it may hinder IMC's formation. One most important aspects of CNT in the matrix is restricting dislocation, which improves strength (Dieringa, 2011; Mohammed & Chen, 2020; Rajesh et al., 2018). The motion of dislocations is arrested by CNT, which leads to a bending of dislocations, as we can see in Figure 4.17 (e). CNT may also be dispersed at grain boundaries, which helps in load transfer from matrix to itself.

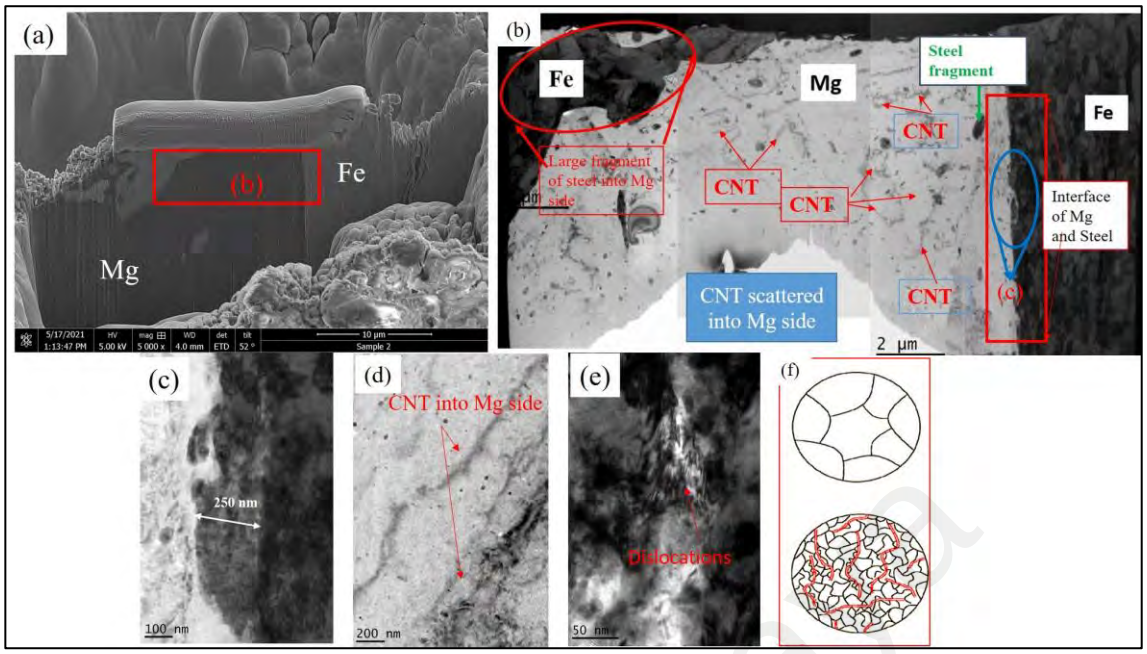


**Figure 4.17: TEM analysis of specimen with 3%CNT+Al (balance) (a) location of lamella preparation (b) complete lamella overview (c) magnified TEM image from,b (d) CNT embedded into Mg side SZ (e) dislocation due to CNT (f) schematic of CNT dispersion at grain**

Figure 4.18 shows TEM-SAED analysis to support IMC and other compound formations. Point 1 is on the magnesium side. The ring pattern of selected area electron diffraction (SAED) can be seen, which depicts polycrystalline material. At point 2, which is at IMC, more than one ring in a concentric circle is observed, revealing the polycrystalline materials. At point 3, steel side, the SAED pattern indicates monocrystalline materials. The SAED result at point 3 again supports the claim that CNT distribution happens only on the magnesium side.

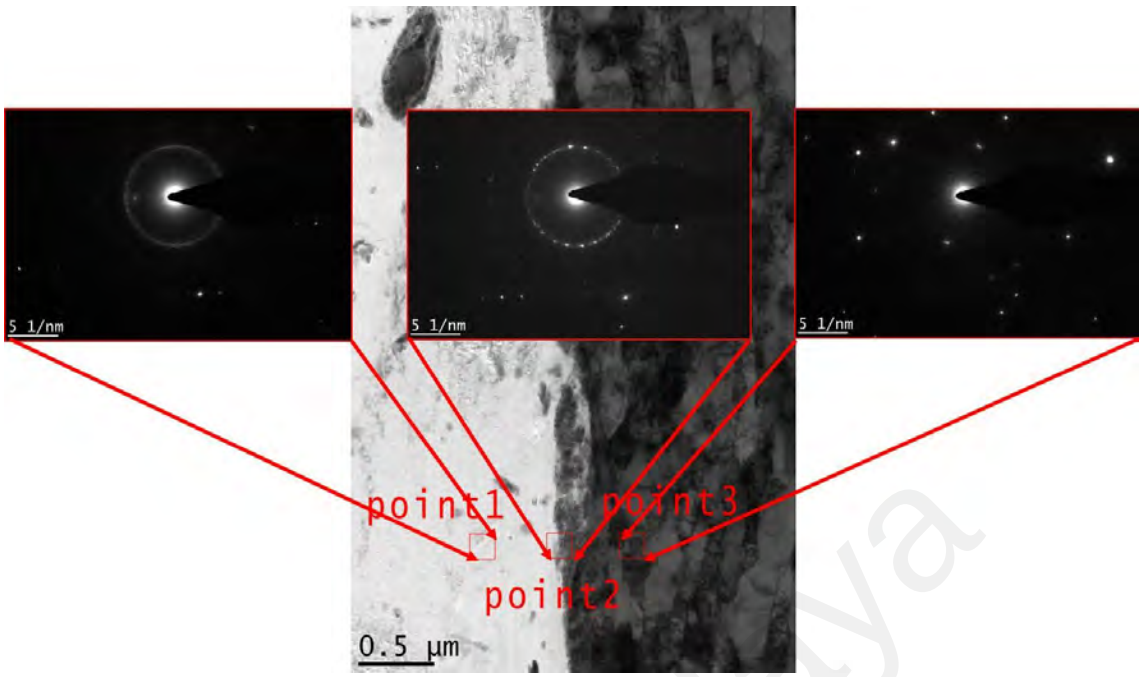


**Figure 4.18: SAED analysis of AZ61 and mild steel with 3% CNT and Al (balance)**

Figure 4.19 shows AZ61 and mild steel TEM-EDS at the interface with 3% CNT and Al (balance) at three locations. From TEM-EDS at point 2, it can be seen that Al-rich IMC is forming. The weight percentage at that point nature of IMC formation is $Fe_2Al_5$. Which is most commonly IMC formed between steel and aluminium at elevated temperature of the process. From point 1 TEM-EDS analysis, it is evident that $Al_2MgC_2$ carbide is forming. It was reported that when the temperature is below 700K, and aluminium content in Mg alloy varies between 0.6% to 19%, it is most likely to form $Al_2MgC_2$ carbide, which could also improve joint strength (Shimizu et al., 2008). The formation of $Al_2MgC_2$ carbide is also mentioned above. Point 3 TEM-EDS shows only Fe atom. This means the CNT is completely dispersed in the magnesium matrix only.

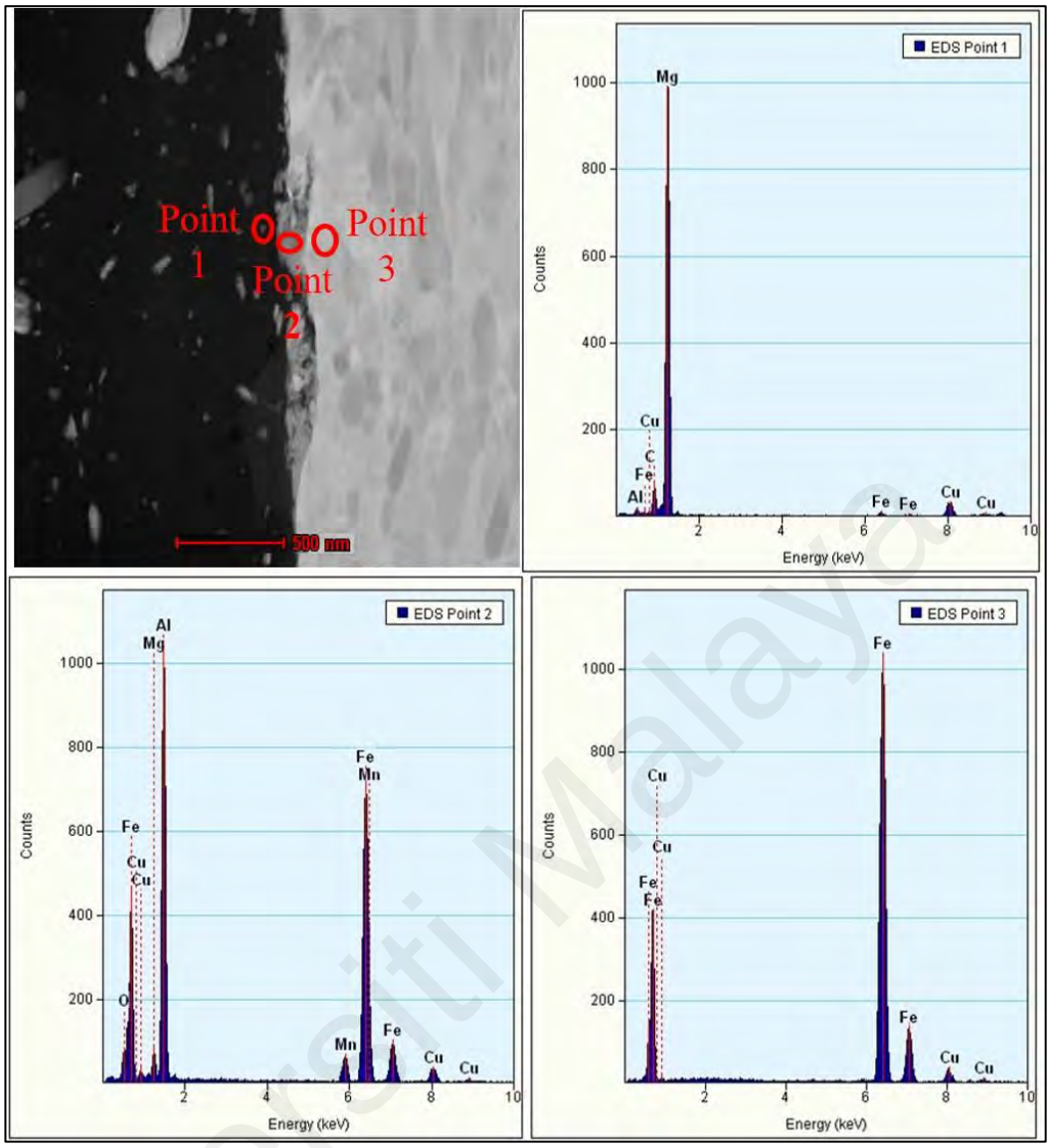


**Figure 4.19: TEM-EDS at 3 different points with 3%CNT and Al (balance) additive**

XRD analysis was performed to confirmation of IMC formation, as shown in Figure 4.20. It can be seen from XRD that $Al_2MgC_2$ and $Fe_2Al_5$ compound is detected. The base Fe and Mg were also detected. $Al_{12}Mg_{17}$ and AlMg compound was also detected in addition to these compounds, which is not confirmed through TEM-EDS. One possible reason could be that we analysed TEM-EDS near the interface, and the formation of the $Al_{12}Mg_{17}$ compound happened in the magnesium matrix far from the interface region. Because in SEM-EDS mapping from Figure 4.16, it can be seen that the mapping of aluminium and magnesium is overlapping in the magnesium matrix.

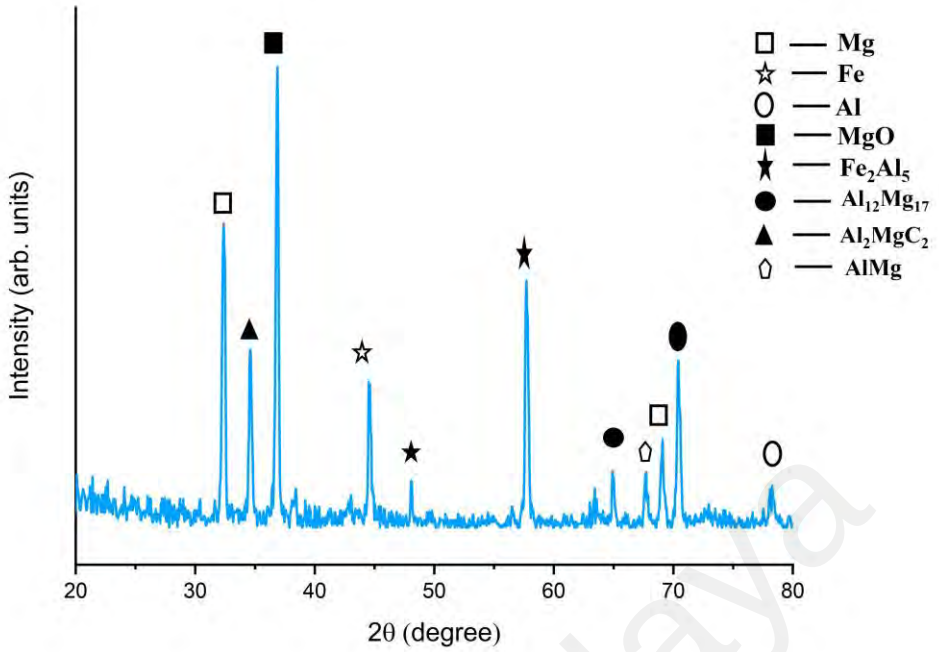


**Figure 4.20: XRD analysis of interface of AZ61 and mild steel specimen with 3% CNT and Al (balance) additive**

### 4.2.4 Effect of welding speed and additive on tensile strength

Figure 4.21 shows the tensile strength of welded samples with the FSA technique at different welding speeds. It can be seen that the tensile strength of 3% CNT+Al (balance) is highest compared to all other conditions. Tensile strength for the sample with 3% CNT is improved up to 88.8% compared to base AZ61 and 61.4% compared to the base steel. The reason behind the improvement is mainly due to the incorporation of additives. It can also be seen that 3% of CNT samples tensile strength is 222 MPa while only aluminium additive samples exhibited 178 MPa, and without any additive, it revealed 137 MPa. At a higher percentage of CNT additive, tensile strength shows the lowest values. The lowering in strength is probably agglomerated CNT, which had an adverse effect on joint strength. The Al additive helps in IMC formation, which is an essential part of joint formation leading to improved strength compared to without any additive specimen, which is demonstrated in FSA of AZ31 and mild steel with Al-Mg additive.

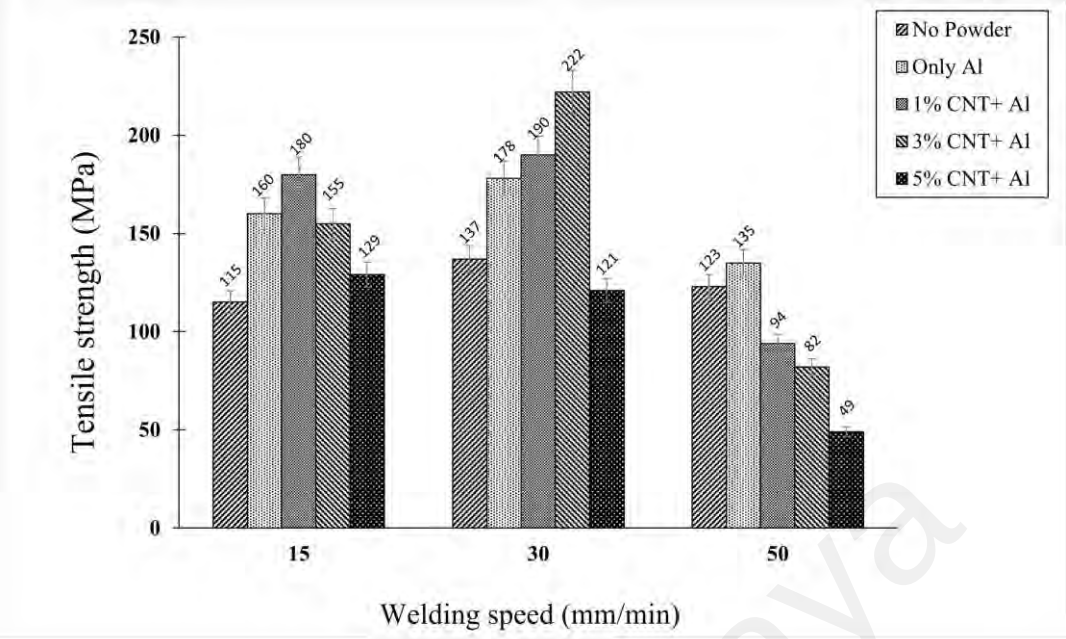


**Figure 4.21: Joining strength for different welding speeds and additives composition**

Various strengthening mechanisms are involved in the improvement of tensile strength. Grain refinement, carbide formation, formation of IMC, load transfer from matrix to CNT, the thermal mismatch between CNT and matrix, and dislocation piled up due to CNT.

The improved mechanical properties of joint with Al-CNT as an additive are due to four strengthening mechanisms: (a) the coefficient of thermal expansion (CTE) gap between the magnesium matrix and the CNT, (b) the Hall-Petch mechanism associated with refined grain, (c) shear lag or load transfer mechanism, and (d) the Orowan mechanism. According to the Zener-Holloman effect, inhibiting grain growth causes grain size to decrease, as shown in Figure 4.14 (b), where magnesium stir zone grain is very fine compared to base magnesium. This grain refinement could contribute to joint strength through the Hall-Petch relationship. Hall-Petch relationship states that the lesser the grain size of material higher the strength. There is a significant mismatch between the magnesium's CTE and CNT's CTE. This mismatch causes dislocation by punching at the boundaries. In addition, due to continuous CNT dispersion, the dislocation density in the

magnesium matrix increases. The dislocation can be observed in Figure 4.17 (e). Furthermore, the accumulation of dislocations at the magnesium matrix and CNT interface boosts joint strength even further. According to the Orowan mechanism, these produced dislocations along the magnesium grain boundary are blocked by microscopic-sized carbide particles. In the current case, a carbide of $Al_2MgC_2$ was formed. As a result, these grains bend, generating back stress and increasing the strength of the weld zone material. The magnesium and the CNT interface establishes the load transfer between the two materials, and we observed that CNT is dispersed in the magnesium matrix.

### 4.2.5 Hardness assessments

Figure 4.22 depicts microhardness of 3% CNT+Al (balance), only Al and without any additive samples along the cross-section. The highest hardness value was recorded with the sample with 3% CNT+Al (balance) additive. The highest hardness value was recorded at 471 HV, which is far higher than Al additive and without any additives samples. The stir zone of the magnesium side exhibits the highest hardness value due to the presence of CNT.

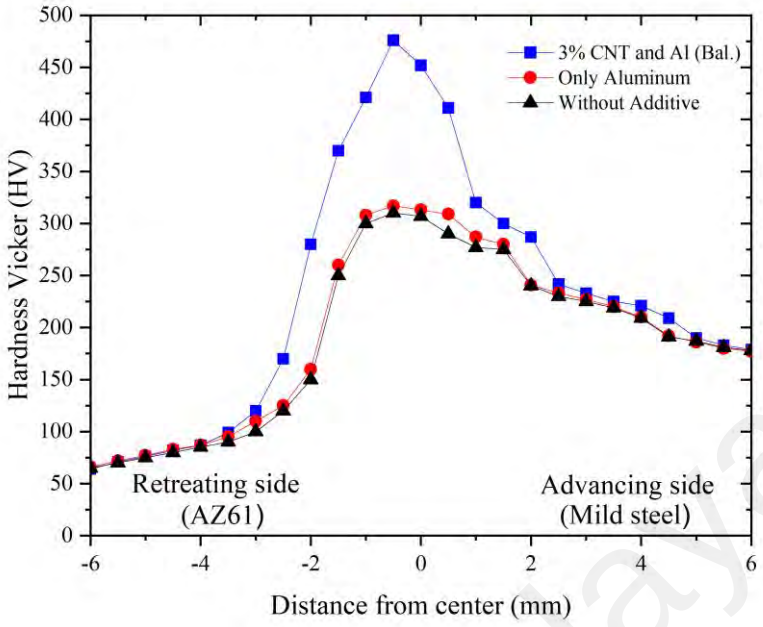


**Figure 4.22: Micro hardness measurement of samples with 3%CNT+Al (balance), only Al and without any additive at 30 mm/min welding speed**

# CHAPTER 5: CONCLUSIONS AND FUTURE RECOMMENDATIONS

## 5.1 Conclusions

In this research, immiscible magnesium alloys and mild steel were joined using the FSA technique with additives in butt configuration. The microstructural evolution was analysed using optical microscopy, SEM imaging, SEM-EDS point and mapping, TEM imaging, and TEM-EDS. Mechanical properties were evaluated using tensile strength tests and microhardness. The conclusion drawn from this study is presented below.

1. A novel method for applying the additives in the FSA was successfully developed and demonstrated. PEG aims to keep additives in the gap during the process without reacting with welding outcomes successfully achieved by eliminating problems associated with additive injection at the interface of workpieces.
2. The dissimilar joint of AZ31 and mild steel with Al-Mg additives using FSA was successfully achieved. The addition of Al powder at a weight percentage of less than 10 wt.% Al-Mg(balance) into the joining interface was designed to maintain the aluminium content that could be lost due to welding heat. The study from SEM-EDS has shown that the aluminium content in the vicinity of the welding interface was successfully maintained. It is considered at this condition, the Al powder was well-dispersed, which can be confirmed in the SEM-EDS mapping, undergone metallurgical reaction during the process with suitable heat input. The formation of the intermetallic compound was confirmed by TEM analysis, measured at 20 to 26-nanometer thickness, which is believed to have improved tensile strength. The highest tensile strength of 150 MPa was recorded for FSA joint with 10 wt.% Al-Mg powder additives produced at a welding speed of 50 mm/min.

3. The AZ61 and mild steel joined were successfully achieved with the Al-CNT additive. The tensile strength was found to be increased as compared to without additive and only Al powder additive. The tensile strength of 3% CNT and Al (balance) at 30 mm/min is 222 MPa, higher than only aluminium and without an additive specimen. Microhardness also improved in the case of CNT additives. Nanoscale level microstructure reveals the formation of IMC, which is in the order of 250 nm and CNT dispersion in the Mg stir zone. The appearance of Al-rich IMC happens in 3% CNT additive, and $Al_2MgC_2$ is also prone to form detected through TEM-EDS. The aim of using CNT is to improve joint strength achieved successfully.
4. Various strengthening mechanisms contributed to the enhance the joint properties in CNT additives. It was revealed that the Zenner pinning mechanism, formation of carbide, dislocation pilling, formation of IMC, and load transfer strengthening mechanism helped in improving strength.

## 5.2 Recommendations for future work

Very few researches have been conducted on CNT additive in FSA. The suitable process parameter still needs to be investigated in detail. The Mg-Fe dissimilar welding using CNT needs to explore more extensively in terms of corrosion and tribological properties. The current research aims toward Mg-Fe joining using the FSA technique. It can be extended to other dissimilar materials too. The deposition method of nanoparticles during FSA must be explored more to operate in industrial practice. Other nanomaterials, such as graphene, and ceramic-based nanomaterials, could also be used to improve the joint properties of dissimilar materials. The IMC and its modelling is also an exciting future work which needs to be addressed. The numerical simulation of the process is not reported, so this could be a possible area for future work.

## REFERENCES


Abd Elnabi, M. M., Osman, T. A., El Mokadem, A., & Elshalakany, A. B. (2020). Evaluation of the formation of intermetallic compounds at the intermixing lines and in the nugget of dissimilar steel/aluminum friction stir welds. *Journal of Materials Research and Technology*, *9*(5), 10209–10222.

Abdollahzadeh, A., Shokuhfar, A., Cabrera, J. M., Zhilyaev, A. P., & Omidvar, H. (2019). In-situ nanocomposite in friction stir welding of 6061-T6 aluminum alloy to AZ31 magnesium alloy. *Journal of Materials Processing Technology*, *263*(March 2018), 296–307.

Abioye, T. E., Zuhailawati, H., Anasyida, A. S., Yahaya, S. A., & Dhindaw, B. K. (2019). Investigation of the microstructure, mechanical and wear properties of AA6061-T6 friction stir weldments with different particulate reinforcements addition. *Journal of Materials Research and Technology*, *8*(5), 3917–3928.

Acharya, U., Roy, B. S., & Saha, S. C. (2019). Torque and force perspectives on particle size and its effect on mechanical property of friction stir welded AA6092/17.5SiC p -T6 composite joints. *Journal of Manufacturing Processes*, *38*(December 2018), 113–121.

Agrawal, P., Shukla, S., Gupta, S., Agrawal, P., & Mishra, R. S. (2020). Friction stir gradient alloying: A high-throughput method to explore the influence of V in enabling HCP to BCC transformation in a γ-FCC dominated high entropy alloy. *Applied Materials Today*, *21*, 100853.

Ahmad Shah, L. H., Sonbolestan, S., Midawi, A. R. H., Walbridge, S., & Gerlich, A. (2019). Dissimilar friction stir welding of thick plate AA5052-AA6061 aluminum alloys: effects of material positioning and tool eccentricity. *International Journal of Advanced Manufacturing Technology*, *105*(1–4), 889–904.

Alireza Askariani, S., Pishbin, H., & Moshref-Javadi, M. (2017). Effect of welding parameters on the microstructure and mechanical properties of the friction stir welded joints of a Mg-12Li-1Al alloy. *Journal of Alloys and Compounds*, *724*, 859–868.

Bahrami, M., Dehghani, K., & Besharati Givi, M. K. (2014). A novel approach to develop aluminum matrix nano-composite employing friction stir welding technique. *Materials and Design*, *53*, 217–225.

Bahrami, M., Farahmand Nikoo, M., & Besharati Givi, M. K. (2015). Microstructural and mechanical behaviors of nano-SiC-reinforced AA7075-O FSW joints prepared through two passes. *Materials Science and Engineering A*, *626*, 220–228.

Bahrami, M., Helmi, N., Dehghani, K., & Givi, M. K. B. (2014). Exploring the effects of SiC reinforcement incorporation on mechanical properties of friction stir welded 7075 aluminum alloy: Fatigue life, impact energy, tensile strength. *Materials Science and Engineering A*, *595*, 173–178.

Baig, Z., Mamat, O., & Mustapha, M. (2018). Recent Progress on the Dispersion and

the Strengthening Effect of Carbon Nanotubes and Graphene-Reinforced Metal Nanocomposites: A Review. *Critical Reviews in Solid State and Materials Sciences*, *43*(1), 1–46.

Balasubramanian, K., & Burghard, M. (2005). Chemically Functionalized Carbon Nanotubes. *Small*, *1*(2), 180–192.

Balog, M., Hu, T., Krizik, P., Castro Riglos, M. V., Saller, B. D., Yang, H., … Lavernia, E. J. (2015). On the thermal stability of ultrafine-grained Al stabilized by in-situ amorphous Al2O3 network. *Materials Science and Engineering A*, *648*, 61–71.

Balog, M., Krizik, P., Nosko, M., Hajovska, Z., Victoria Castro Riglos, M., Rajner, W., … Simancik, F. (2014). Forged HITEMAL: Al-based MMCs strengthened with nanometric thick Al2O3 skeleton. *Materials Science and Engineering A*, *613*, 82–90.

Balog, M., Poletti, C., Simancik, F., Walcher, M., & Rajner, W. (2011). The effect of native Al2O3 skin disruption on properties of fine Al powder compacts. *Journal of Alloys and Compounds*, *509*(SUPPL. 1), S235–S238.

Banerjee, S., Kahn, M. G. C., & Wong, S. S. (2003). Rational Chemical Strategies for Carbon Nanotube Functionalization. *Chemistry – A European Journal*, *9*(9), 1898–1908.

Bisadi, H., Tavakoli, A., Tour Sangsaraki, M., & Tour Sangsaraki, K. (2013). The influences of rotational and welding speeds on microstructures and mechanical properties of friction stir welded Al5083 and commercially pure copper sheets lap joints. *Materials & Design*, *43*, 80–88.

Bodaghi, M., & Dehghani, K. (2017). Friction stir welding of AA5052: the effects of SiC nano-particles addition. *International Journal of Advanced Manufacturing Technology*, *88*(9–12), 2651–2660.

Boucherit, A., Avettand-Fènoël, M.-N., & Taillard, R. (2017). Effect of a Zn interlayer on dissimilar FSSW of Al and Cu. *Materials & Design*, *124*, 87–99.

Brinson, L. C. (2021). How much air pollution comesfrom cars? Retrieved November 25, 2021, from https://auto.howstuffworks.com/air-pollution-from-cars.htm

Buchibabu, V., Reddy, G. M., & De, A. (2017). Probing torque, traverse force and tool durability in friction stir welding of aluminum alloys. *Journal of Materials Processing Technology*, *241*, 86–92.

Buffa, G., Campanella, D., Forcellese, A., Fratini, L., Simoncini, M., & Barcellona, A. (2019). Constant Heat Input Friction Stir Welding of Variable Thickness AZ31 Sheets Through In-Process Tool Rotation Control. *Journal of Manufacturing Science and Engineering*, *141*(8). https://doi.org/10.1115/1.4043838

Cao, R., Chang, J. H., Huang, Q., Zhang, X. B., Yan, Y. J., & Chen, J. H. (2018). Behaviors and effects of Zn coating on welding-brazing process of Al-Steel and Mg-steel dissimilar metals. *Journal of Manufacturing Processes*, *31*, 674–688.

Cao, R., Xu, Q. W., Zhu, H. X., Mao, G. J., Lin, Q., Chen, J. H., & Wang, P.-C. (2016). Weldability and Distortion of Mg AZ31-to-Galvanized Steel SPOT Plug Welding Joint by Cold Metal Transfer Method. *Journal of Manufacturing Science and Engineering*, *139*(2). https://doi.org/10.1115/1.4034009

Casalino, G., Guglielmi, P., Lorusso, V. D., Mortello, M., Peyre, P., & Sorgente, D. (2017). Laser offset welding of AZ31B magnesium alloy to 316 stainless steel. *Journal of Materials Processing Technology*, *242*, 49–59.

Chen, K., Liu, X., & Ni, J. (2018). Friction Stir Resistance Spot Welding of Aluminum Alloy to Advanced High Strength Steel. *Journal of Manufacturing Science and Engineering, Transactions of the ASME*, *140*(11), 1–10.

Chen, Y. C., & Nakata, K. (2009). Effect of tool geometry on microstructure and mechanical properties of friction stir lap welded magnesium alloy and steel. *Materials & Design*, *30*(9), 3913–3919.

Chen, Y., Chen, J., Amirkhiz, B. S., Worswick, M. J., & Gerlich, A. P. (2015). Microstructures and properties of Mg alloy/DP600 steel dissimilar refill friction stir spot welds. *Science and Technology of Welding and Joining*, *20*(6), 494–501.

Coelho, R. S., Kostka, A., dos Santos, J. F., & Kaysser-Pyzalla, A. (2012). Friction-stir dissimilar welding of aluminium alloy to high strength steels: Mechanical properties and their relation to microstructure. *Materials Science and Engineering: A*, *556*, 175–183.

Coleman, J. N., Khan, U., Blau, W. J., & Gun'ko, Y. K. (2006). Small but strong: A review of the mechanical properties of carbon nanotube–polymer composites. *Carbon*, *44*(9), 1624–1652.

Denquin, A., Allehaux, D., MH, C., & Lapasset, G. (2003). Microstructural and mechanical evolutions within friction stir welds of precipitation hardened aluminium alloys. *Materials Science Forum*, *426–4*, 2921–2926.

Derazkola, H. A., & Khodabakhshi, F. (2020). A novel fed friction-stir (FFS) technology for nanocomposite joining. *Science and Technology of Welding and Joining*, *25*(2), 89–100.

Dharani Kumar, S., & Suresh Kumar, S. (2022). Effect of Shot Peening on the Ballistic Performance of Friction Stir Welded Magnesium Alloy (AZ31B) Joints. *Journal of Materials Engineering and Performance*.

Dieringa, H. (2011). Properties of magnesium alloys reinforced with nanoparticles and carbon nanotubes: A review. *Journal of Materials Science*, *46*(2), 289–306.

Ding, M., Liu, S. S., Zheng, Y., Wang, Y. C., Li, H., Xing, W. Q., … Dong, P. (2018). TIG–MIG hybrid welding of ferritic stainless steels and magnesium alloys with Cu interlayer of different thickness. *Materials & Design*, *88*, 375–383.

Doley, J. K., & Kore, S. D. (2016). A Study on Friction Stir Welding of Dissimilar Thin Sheets of Aluminum Alloys AA 5052–AA 6061. *Journal of Manufacturing Science and Engineering*, *138*(11)

Dorbane, A., Mansoor, B., Ayoub, G., Shunmugasamy, V. C., & Imad, A. (2016). Mechanical, microstructural and fracture properties of dissimilar welds produced by friction stir welding of AZ31B and Al6061. *Materials Science and Engineering: A*, *651*, 720–733.

Dragatogiannis, D. A., Koumoulos, E. P., Kartsonakis, I. A., Pantelis, D. I., Karakizis, P. N., & Charitidis, C. A. (2016). Dissimilar Friction Stir Welding Between 5083 and 6082 Al Alloys Reinforced With TiC Nanoparticles. *Materials and Manufacturing Processes*, *31*(16), 2101–2114.

Elthalabawy, W. M., & Khan, T. I. (2015a). Eutectic bonding of austenitic stainless steel 316L to magnesium alloy AZ31 using copper interlayer. *The International Journal of Advanced Manufacturing Technology*, *55*(1), 235–241.

Elthalabawy, W. M., & Khan, T. I. (2015b). Microstructural development of diffusion-brazed austenitic stainless steel to magnesium alloy using a nickel interlayer. *Materials Characterization*, *61*(7), 703–712.

ESAB. (2009). Technical Hand Book: Friction Stir Welding. *Global Welding & Cutting*, 1–45. Retrieved from http://www.esab.com/global/en/education/tech-info-friction-stir-welding.cfm%5Cnwww.esab.com%5Cn13/04/2012

Esmaeili, A., Zareie Rajani, H. R., Sharbati, M., Givi, M. K. B., & Shamanian, M. (2011). The role of rotation speed on intermetallic compounds formation and mechanical behavior of friction stir welded brass/aluminum 1050 couple. *Intermetallics*, *19*(11), 1711–1719.

Fallahi, A. A., Shokuhfar, A., Ostovari Moghaddam, A., & Abdolahzadeh, A. (2017). Analysis of SiC nano-powder effects on friction stir welding of dissimilar Al-Mg alloy to A316L stainless steel. *Journal of Manufacturing Processes*, *30*, 418–430.

Fu, B., Shen, J., Suhuddin, U. F. H. R., Pereira, A. A. C., Maawad, E., dos Santos, J. F., … Rethmeier, M. (2021). Revealing joining mechanism in refill friction stir spot welding of AZ31 magnesium alloy to galvanized DP600 steel. *Materials and Design*, *209*, 109997.

Fu, X., Chen, K., Liu, C., Wang, M., & Hua, X. (2022). Microstructure and mechanical properties of dissimilar friction stir lap welding between AZ31 Mg alloy and DC01 steel. *Materials Characterization*, *187*, 111870.

Gao, J., Li, C., Shilpakar, U., & Shen, Y. (2015). Improvements of mechanical properties in dissimilar joints of HDPE and ABS via carbon nanotubes during friction stir welding process. *Materials and Design*, *86*, 289–296.

Geim, A. K., & Novoselov, K. S. (2007). The rise of graphene. *Nature Materials*, *6*(3), 183–191. https://doi.org/10.1038/nmat1849

Hasiri, A. M., & Al, E. (2015). Interfacial Microstructure of Laser Brazed AZ31B Magnesium to Sn - Plated Steel Sheet. *Welding Journal*, *94*(03), 61–72.

Hirsch, A., & Vostrowsky, O. (2005). Functionalization of Carbon Nanotubes. In A. D. Schlüter (Ed.), *Functional Molecular Nanostructures* (pp. 193–237).

Hong, S. T., Das, H., Oh, H. S., Nasim, M. N. E. A. Al, & Chun, D. M. (2017). Combination of nano-particle deposition system and friction stir spot welding for fabrication of carbon/aluminum metal matrix composite joints of dissimilar aluminum alloys. *CIRP Annals*, *66*(1), 261–264.

Ibrahim, I., Ito, R., Kakiuchi, T., Uematsu, Y., Yun, K., & Matsuda, C. (2016). Fatigue behaviour of Al/steel dissimilar resistance spot welds fabricated using Al–Mg interlayer. *Science and Technology of Welding and Joining*, *21*(3), 223–233.

Iijima, S., & Ichihashi, T. (1993). Single-shell carbon nanotubes of 1-nm diameter. *Nature*, *363*(6430), 603–605.

Imam, M., Racherla, V., Biswas, K., Fujii, H., Chintapenta, V., Sun, Y., & Morisada, Y. (2017). Microstructure-property relation and evolution in friction stir welding of naturally aged 6063 aluminium alloy. *International Journal of Advanced Manufacturing Technology*, *91*(5–8), 1753–1769.

Inada, K., Fujii, H., Ji, Y. S., Sun, Y. F., & Morisada, Y. (2010). Effect of gap on FSW joint formation and development of friction powder processing. *Science and Technology of Welding and Joining*, *15*(2), 131–136.

Jana, S., Hovanski, Y., & Grant, G. J. (2015). Friction stir lap welding of magnesium alloy to steel: A preliminary investigation. *Metallurgical and Materials Transactions A: Physical Metallurgy and Materials Science*, *41*(12), 3173–3182.

Jayabalakrishnan, D., & Balasubramanian, M. (2018). Eccentric-weave FSW between Cu and AA 6061-T6 with reinforced Graphene nanoparticles. *Materials and Manufacturing Processes*, *33*(3), 333–342.

Jeon, C. H., Jeong, Y. H., Seo, J. J., Tien, H. N., Hong, S. T., Yum, Y. J., … Lee, K. J. (2014). Material properties of graphene/aluminum metal matrix composites fabricated by friction stir processing. *International Journal of Precision Engineering and Manufacturing*, *15*(6), 1235–1239.

Jiang, M., Gao, M., Li, G., Zhang, C., & Zeng, X. (2014). Research on laser welding-brazing of dissimilar Mg alloy and stainless steel. *Kovove Materialy*, *52*(1), 11–17. https://doi.org/10.4149/km_2014_1_11

Jiang, W. H., & Kovacevic, R. (2004). Feasibility study of friction stir welding of 6061-T6 aluminium alloy with AISI 1018 steel. *Proceedings of the Institution of Mechanical Engineers, Part B: Journal of Engineering Manufacture*, *218*(10), 1323–1331.

John, V. (2021). 1.2 Billion Vehicles On World's Roads Now, 2 Billion By 2035: Report. Retrieved November 20, 2021, from https://www.greencarreports.com/news/1093560_1-2-billion-vehicles-on-worlds-roads-now-2-billion-by-2035-report

Joo, S. (2013). Joining of dissimilar AZ31B magnesium alloy and SS400 mild steel by hybrid gas tungsten arc friction stir welding. *Metals and Materials International*, *19*(6), 1251–1257.

Kang, M., Kim, C., & Kim, Y. M. (2018). Joining of AZ31 magnesium alloy and steel sheet under four different coating conditions based on gas metal arc weld-brazing. *Materials Transactions*, *58*(1), 95–102.

Kar, A., Choudhury, S. K., Suwas, S., & Kailas, S. V. (2018). Effect of niobium interlayer in dissimilar friction stir welding of aluminum to titanium. *Materials Characterization*, *145*(September), 402–412.

Karakizis, P. N., Pantelis, D. I., Dragatogiannis, D. A., Bougiouri, V. D., & Charitidis, C. A. (2019). Study of friction stir butt welding between thin plates of AA5754 and mild steel for automotive applications. *The International Journal of Advanced Manufacturing Technology*, *102*(9), 3065–3076.

Karakizis, P. N., Pantelis, D. I., Fourlaris, G., & Tsakiridis, P. (2018a). Effect of SiC and TiC nanoparticle reinforcement on the microstructure, microhardness, and tensile performance of AA6082-T6 friction stir welds. *International Journal of Advanced Manufacturing Technology*, *95*(9–12), 3823–3837.

Karakizis, P. N., Pantelis, D. I., Fourlaris, G., & Tsakiridis, P. (2018b). The role of SiC and TiC nanoparticle reinforcement on AA5083-H111 friction stir welds studied by electron microscopy and mechanical testing. *International Journal of Advanced Manufacturing Technology*, *94*(9–12), 4159–4176.

Karthik, G. M., Ram, G. D. J., & Kottada, R. S. (2017). Fiction stir selective alloying. *Materials Science & Engineering A*, *684*(December 2016), 186–190.

Karthikeyan, P., & Mahadevan, K. (2015). Investigation on the effects of SiC particle addition in the weld zone during friction stir welding of Al 6351 alloy. *International Journal of Advanced Manufacturing Technology*, *80*(9–12), 1919–1926.

Kartsonakis, I. A., Dragatogiannis, D. A., Koumoulos, E. P., Karantonis, A., & Charitidis, C. A. (2016). Corrosion behaviour of dissimilar friction stir welded aluminium alloys reinforced with nanoadditives. *Materials and Design*, *102*, 56–67.

Kasai, H., Morisada, Y., & Fujii, H. (2015a). Dissimilar FSW of immiscible materials: Steel/magnesium. *Materials Science and Engineering A*, *624*, 250–255.

Kasai, H., Morisada, Y., & Fujii, H. (2015b). *FSW of immiscible materials : Steel / magnesium*. *624*, 250–255.

Kaye, G. W. C., & Laby, T. H. (1997). Tables of Physical and Chemical Constants. *Zeitschrift Fur Kristallographie - New Crystal Structures*, *212*(5), 400. https://doi.org/10.1524/zkri.1997.212.5.400

Khodabakhshi, F., Nosko, M., & Gerlich, A. P. (2018). Effects of graphene nano-platelets (GNPs) on the microstructural characteristics and textural development of an Al-Mg alloy during friction-stir processing. *Surface and Coatings Technology*, *335*, 288–305.

Kim, Y. G., Fujii, H., Tsumura, T., Komazaki, T., & Nakata, K. (2006). Three defect

types in friction stir welding of aluminum die casting alloy. *Materials Science and Engineering: A*, *415*(1), 250–254.

Küçükömeroğlu, T., Aktarer, S. M., İpekoğlu, G., & Çam, G. (2018). Microstructure and mechanical properties of friction-stir welded St52 steel joints. *International Journal of Minerals, Metallurgy and Materials*, *25*(12), 1457–1464.

Kurmanaeva, L., Topping, T. D., Wen, H., Sugahara, H., Yang, H., Zhang, D., … Lavernia, E. J. (2015). Strengthening mechanisms and deformation behavior of cryomilled Al-Cu-Mg-Ag alloy. *Journal of Alloys and Compounds*, *632*, 591–603.

Kusuda, Y. (2013). Honda develops robotized FSW technology to weld steel and aluminum and applied it to a mass-production vehicle. *Industrial Robot*, *40*(3), 208–212.

Lavagna, L., Nisticò, R., Musso, S., & Pavese, M. (2021). Functionalization as a way to enhance dispersion of carbon nanotubes in matrices: a review. *Materials Today Chemistry*, *20*. https://doi.org/10.1016/j.mtchem.2021.100477

Lavagna, Luca, Massella, D., & Pavese, M. (2017). Preparation of hierarchical material by chemical grafting of carbon nanotubes onto carbon fibers. *Diamond and Related Materials*, *80*, 118–124.

Lavernia, E. J., Han, B. Q., & Schoenung, J. M. (2008). Cryomilled nanostructured materials: Processing and properties. *Materials Science and Engineering A*, *493*(1–2), 207–214.

Lee, S. J., Shin, S. E., Sun, Y., Fujii, H., & Park, Y. (2018). Friction stir welding of multi-walled carbon nanotubes reinforced Al matrix composites. *Materials Characterization*, *145*(July), 653–663.

Li, L., Tan, C., Chen, Y., Guo, W., & Mei, C. (2013). CO2 laser welding–brazing characteristics of dissimilar metals AZ31B Mg alloy to Zn coated dual phase steel with Mg based filler. *Journal of Materials Processing Technology*, *213*(3), 361–375.

Li, X., Zhang, Z., Peng, Y., Yan, D., Tan, Z., Zhou, Q., & Wang, K. (2021). In situ synthesized nano-Al4C3 reinforced aluminum matrix composites via friction stir processing. *Journal of Materials Research and Technology*, *14*, 2658–2664.

Liang, J., Li, H., Qi, L., Tian, W., Li, X., Chao, X., & Wei, J. (2017). Fabrication and mechanical properties of CNTs/Mg composites prepared by combining friction stir processing and ultrasonic assisted extrusion. *Journal of Alloys and Compounds*, *728*, 282–288.

Lipecka, J., Andrzejczuk, M., Lewandowska, M., Janczak-Rusch, J., & Kurzydłowski, K. J. (2011). Evaluation of thermal stability of ultrafine grained aluminium matrix composites reinforced with carbon nanotubes. *Composites Science and Technology*, *71*(16), 1881–1885.

Liu, L, Xiao, L., & Chen, D. L. (2017). Microstructure and fatigue properties of Mg-to-steel dissimilar resistance spot welds. *Materials & Design*, *45*, 336–342.

Liu, L, Xiao, L., Feng, J., Li, L., Esmaeili, S., & Zhou, Y. (2011). Bonding of immiscible Mg and Fe via a nanoscale Fe2Al5 transition layer. *Scripta Materialia*, *65*(11), 982–985.

Liu, L, Xiao, L., Feng, J., Li, L., Esmaeili, S., & Zhou, Y. (2017). Bonding of immiscible Mg and Fe via a nanoscale Fe2Al5 transition layer. *Scripta Materialia*, *65*(11), 982–985.

Liu, Lei, Zou, G., Mori, H., Esmaeili, S., & Zhou, Y. N. (2018). Nanostructure of immiscible Mg–Fe dissimilar weld without interfacial intermetallic transition layer. *Materials & Design*, *92*, 445–449.

Liu, Liming, & Qi, X. (2010). Strengthening effect of nickel and copper interlayers on hybrid laser-TIG welded joints between magnesium alloy and mild steel. *Materials & Design*, *31*(8), 3960–3963.

Liu, Liming, Qi, X., & Zhang, Z. (2016). The effect of alloying elements on the shear strength of the lap joint of az31b magnesium alloy to q235 steel by hybrid laser-tig welding technique. *Metallurgical and Materials Transactions A: Physical Metallurgy and Materials Science*, *43*(6), 1976–1988.

Liu, X. C., & Wu, C. S. (2015). Material flow in ultrasonic vibration enhanced friction stir welding. *Journal of Materials Processing Technology*, *225*, 32–44.

Liu, X., Wang, X., Wang, B., Zhang, L., Yang, C., & Chai, T. (2017). The Role of Mechanical Connection during Friction Stir Keyholeless Spot Welding Joints of Dissimilar Materials. *Metals*, *7*(6). https://doi.org/10.3390/met7060217

Liyanage, T., Kilbourne, J., Gerlich, A. P., & North, T. H. (2009). Joint formation in dissimilar Al alloy/steel and Mg alloy/steel friction stir spot welds. *Science and Technology of Welding and Joining*, *14*(6), 500–508.

Lohwasser, D., & Chen, Z. (2010). *Friction stir welding: From basics to applications*. Cambridge:Woodhead publishing limited.

Ma, P.-C., Mo, S.-Y., Tang, B.-Z., & Kim, J.-K. (2010). Dispersion, interfacial interaction and re-agglomeration of functionalized carbon nanotubes in epoxy composites. *Carbon*, *48*(6), 1824–1834.

Magalhães, V. M., Leitão, C., & Rodrigues, D. M. (2018). Friction stir welding industrialisation and research status. *Science and Technology of Welding and Joining*, *23*(5), 400–409.

Manladan, S. M., Yusof, F., Ramesh, S., Zhang, Y., Luo, Z., & Ling, Z. (2017). Microstructure and mechanical properties of resistance spot welded in welding-brazing mode and resistance element welded magnesium alloy/austenitic stainless steel joints. *Journal of Materials Processing Technology*, *250*, 45–54.

Mao, H. K., & Bell, P. M. (1979). Equations of state of MgO and ε Fe under static pressure conditions. *Journal of Geophysical Research: Solid Earth*, *84*(B9), 4533–4536.

Martinsen, K., Hu, S. J., & Carlson, B. E. (2015). Joining of dissimilar materials. *CIRP Annals*, *64*(2), 679–699.

Maurya, R., Kumar, B., Ariharan, S., Ramkumar, J., & Balani, K. (2016). Effect of carbonaceous reinforcements on the mechanical and tribological properties of friction stir processed Al6061 alloy. *Materials and Design*, *98*, 155–166.

McClure, J. C. (1998). Intercalation vortices and related microstructural features in the friction-stir welding of dissimilar metals. *Materials Research Innovations*, *2*(3), 150–163.

Meng, X., Huang, Y., Cao, J., Shen, J., & dos Santos, J. F. (2021). Recent progress on control strategies for inherent issues in friction stir welding. *Progress in Materials Science*, *115*(June 2020), 100706. https://doi.org/10.1016/j.pmatsci.2020.100706

Meng, Y., Ma, Y., Chen, S., Han, Y., Chen, S., Huang, J., & Yang, J. (2021). Friction stir butt welding of magnesium alloy to steel by truncated cone-shaped stirring pin with threads. *Journal of Materials Processing Technology*, *291*(June 2020), 117038. https://doi.org/10.1016/j.jmatprotec.2020.117038

Messler, R. W. (2004). Joining of Materials and Structures. *Pragmatic Process to Enabling Technology*, xxi–xxiv. https://doi.org/10.1016/B978-075067757-8/50000-2

Miao, Y. G., Han, D. F., Yao, J. Z., & Li, F. (2010). Microstructure and interface characteristics of laser penetration brazed magnesium alloy and steel. *Science and Technology of Welding and Joining*, *15*(2), 97–103.

Miao, Y., Han, D., Xu, X., & Wu, B. (2014). Phase constitution in the interfacial region of laser penetration brazed magnesium–steel joints. *Materials Characterization*, *93*, 87–93.

Miao, Y., Han, D., Yao, J., & Li, F. (2010). Effect of laser offsets on joint performance of laser penetration brazing for magnesium alloy and steel. *Materials & Design*, *31*(6), 3121–3126.

Mirjavadi, S. S., Alipour, M., Emamian, S., Kord, S., Hamouda, A. M. S., Koppad, P. G., & Keshavamurthy, R. (2017). Influence of TiO2 nanoparticles incorporation to friction stir welded 5083 aluminum alloy on the microstructure, mechanical properties and wear resistance. *Journal of Alloys and Compounds*, *712*, 795–803.

Mishra, R. S., & Ma, Z. Y. (2005a). Friction stir welding and processing. *Materials Science and Engineering R: Reports*, *50*(1–2), 1–78.

Mishra, R. S., & Ma, Z. Y. (2005b). Friction stir welding and processing. *Materials Science and Engineering: R: Reports*, *50*(1), 1–78.

Mohammed, S. M. A. K., & Chen, D. L. (2020). Carbon Nanotube-Reinforced Aluminum Matrix Composites. *Advanced Engineering Materials*, *22*(4), 1–26.

Moiduddin, K., Siddiquee, A. N., Abidi, M. H., Mian, S. H., & Mohammed, M. K. (2021). On novel copper based alloys development via friction stir alloying.

*Crystals*, *11*(5), 1–12.

Mokabberi, S. R., Movahedi, M., & Kokabi, A. H. (2018). Effect of interlayers on softening of aluminum friction stir welds. *Materials Science and Engineering A*, *727*(April), 1–10.

Montazerian, M. H., Movahedi, M., & Jondi, M. R. (2019). Effect of Graphene and Process Parameters on Mechanical Performance and Electrical Resistance of Aluminum to Copper Friction Stir Joint. *Materials Research Express*, 0–12. https://doi.org/10.1088/2053-1591/aafe1a

Moradi, M. M., Jamshidi Aval, H., & Jamaati, R. (2018). Microstructure and mechanical properties in nano and microscale SiC-included dissimilar friction stir welding of AA6061-AA2024. *Materials Science and Technology (United Kingdom)*, *34*(4), 388–401.

Muhamad, M. R., Raja, S., Jamaludin, M. F., Yusof, F., Morisada, Y., Suga, T., & Fujii, H. (2021). Enhancements on dissimilar friction stir welding between AZ31 and SPHC mild steel with Al-Mg as powder additives. *Journal of Manufacturing Science and Engineering*, *143*(July), 1–22.

Murdoch, J. (2008). Cars and Metal, Metal and Cars. Retrieved June 13, 2020, from The World Steel Association website: https://www.etf.com/sections/features-and-news/1289-cars-and-metal-metal-and-cars?nopaging=1.

Nasiri, A M, & Zhou, Y. (2015). Effect of Zn interlayer on brazeability of AZ31B–Mg alloy to steel sheet. *Science and Technology of Welding and Joining*, *20*(2), 155–163.

Nasiri, Ali M, Chartrand, P., Weckman, D. C., & Zhou, N. Y. (2019). Thermochemical Analysis of Phases Formed at the Interface of a Mg alloy-Ni-plated Steel Joint during Laser Brazing. *Metallurgical and Materials Transactions A*, *44*(4), 1937–1946.

Nasiri, Ali M, Lee, M. Y., Weckman, D. C., & Zhou, Y. (2014). Effects of Interfacial Lattice Mismatching on Wetting of Ni-Plated Steel by Magnesium. *Metallurgical and Materials Transactions A*, *45*(12), 5749–5766.

Nosko, M., Štepánek, M., Zifčák, P., Orovčík, L., Nagy, Dvorák, T., … Gerlich, A. P. (2019). Solid-state joining of powder metallurgy Al-Al 2 O 3 nanocomposites via friction-stir welding: Effects of powder particle size on the weldability, microstructure, and mechanical property. *Materials Science and Engineering A*, *754*(January), 190–204.

Paidar, M., Asgari, A., Ojo, O. O., & Saberi, A. (2018). Mechanical Properties and Wear Behavior of AA5182/WC Nanocomposite Fabricated by Friction Stir Welding at Different Tool Traverse Speeds. *Journal of Materials Engineering and Performance*, *27*(4), 1714–1724.

Pang, Q., Hu, Z. L., & Song, J. S. (2019). Preparation and mechanical properties of closed-cell CNTs-reinforced Al composite foams by friction stir welding. *International Journal of Advanced Manufacturing Technology*, *103*(5–8), 3125–

3136.

Patel, V. K., Bhole, S. D., & Chen, D. L. (2013). Formation of zinc interlayer texture during dissimilar ultrasonic spot welding of magnesium and high strength low alloy steel. *Materials & Design*, *45*, 236–240.

Patel, V. K., Bhole, S. D., & Chen, D. L. (2015). Characterization of ultrasonic spot welded joints of Mg-to-galvanized and ungalvanized steel with a tin interlayer. *Journal of Materials Processing Technology*, *214*(4), 811–817.

Patterson, E. E., Hovanski, Y., & Field, D. P. (2016). Microstructural Characterization of Friction Stir Welded Aluminum-Steel Joints. *Metallurgical and Materials Transactions A: Physical Metallurgy and Materials Science*, *47*(6), 2815–2829.

Pavese, M., Musso, S., Bianco, S., Giorcelli, M., & Pugno, N. (2008). An analysis of carbon nanotube structure wettability before and after oxidation treatment. *Journal of Physics: Condensed Matter*, *20*(47), 474206. https://doi.org/10.1088/0953-8984/20/47/474206

Petroleum Consumption/Countries of the World. (n.d.). Retrieved November 30, 2021, from https://www.citypopulation.de/en/world/bymap/OilConsumption.html

Phaneesh, K. R., Bhat, A., Mukherjee, P., & Kashyap, K. T. (2012). On the Zener limit of grain growth through 2D Monte Carlo simulation. *Computational Materials Science*, *58*, 188–191.

Pourali, M., Abdollah-zadeh, A., Saeid, T., & Kargar, F. (2017a). Influence of welding parameters on intermetallic compounds formation in dissimilar steel/aluminum friction stir welds. *Journal of Alloys and Compounds*, *715*, 1–8.

Pourali, M., Abdollah-zadeh, A., Saeid, T., & Kargar, F. (2017b). Influence of welding parameters on intermetallic compounds formation in dissimilar steel/aluminum friction stir welds. *Journal of Alloys and Compounds*, *715*, 1–8.

Pouriamanesh, R., Dehghani, K., & Vallant, R. (2019). Friction stir welding of API X70 steel incorporating Ti-dioxide. *Canadian Metallurgical Quarterly*, *58*(1), 69–81.

Prasad, B. L., Neelaiah, G., Krishna, M. G., Ramana, S. V. V, Prakash, K. S., Sarika, G., … Sunil, B. R. (2018). Joining of AZ91 Mg alloy and Al6063 alloy sheets by friction stir welding. *Journal of Magnesium and Alloys*, *6*(1), 71–76.

Raj, S., & Biswas, P. (2022). Mechanical and microstructural characterizations of friction stir welded dissimilar butt joints of Inconel 718 and AISI 204Cu austenitic stainless steel. *Materials Characterization*, *185*, 111763.

Raja, S., Muhamad, M. R., Jamaludin, M. F., & Yusof, F. (2020). A review on nanomaterials reinforcement in friction stir welding. *Journal of Materials Research and Technology*, *9*(6), 16459–16487.

Rajesh Jesudoss Hynes, N., Sankaranarayanan, R., Kathiresan, M., Senthamaraikannan, P., Khan, A., Asiri, A. M., & Khan, I. (2018). Synthesis, properties, and characterization of carbon nanotube-reinforced metal matrix composites. In

*Nanocarbon and its Composites: Preparation, Properties and Applications*. https://doi.org/10.1016/B978-0-08-102509-3.00027-4

Ramachandran, K. K., Murugan, N., & Shashi Kumar, S. (2015). Influence of tool traverse speed on the characteristics of dissimilar friction stir welded aluminium alloy, AA5052 and HSLA steel joints. *Archives of Civil and Mechanical Engineering*, *15*(4), 822–830.

Ren, D., & Liu, L. (2017). Interface microstructure and mechanical properties of arc spot welding Mg–steel dissimilar joint with Cu interlayer. *Materials & Design*, *59*, 369–376.

Rezaee Hajideh, M., Farahani, M., & Molla Ramezani, N. (2018). Reinforced Dissimilar Friction Stir Weld of Polypropylene to Acrylonitrile Butadiene Styrene with Copper Nanopowder. *Journal of Manufacturing Processes*, *32*, 445–454.

Rohrer, G. S. (2010). "introduction to grains, phases, and interfaces-an interpretation of microstructure," Trans. AIME, 1948, vol. 175, pp. 15-51, by C.S. Smith. In *Metallurgical and Materials Transactions A: Physical Metallurgy and Materials Science* (Vol. 41).

Sahu, S., Mypati, O., Pal, S. K., & Shome, M. (2021). Effect of weld parameters on joint quality in friction stir welding of Mg alloy to DP steel dissimilar materials. *CIRP Journal of Manufacturing Science and Technology*, *35*, 502–516.

Sakthivel, T., Sengar, G. S., & Mukhopadhyay, J. (2009). Effect of welding speed on microstructure and mechanical properties of friction-stir-welded aluminum. *The International Journal of Advanced Manufacturing Technology*, *43*(5), 468–473.

Sanaty-Zadeh, A. (2012). Comparison between current models for the strength of particulate-reinforced metal matrix nanocomposites with emphasis on consideration of Hall-Petch effect. *Materials Science and Engineering A*, *531*, 112–118.

Sarkari Khorrami, M., Samadi, S., Janghorban, Z., & Movahedi, M. (2015). In-situ aluminum matrix composite produced by friction stir processing using FE particles. *Materials Science and Engineering: A*, *641*, 380–390.

Sato, Y. S., Urata, M., Kokawa, H., & Ikeda, K. (2003). Hall-Petch relationship in friction stir welds of equal channel angular-pressed aluminium alloys. *Materials Science and Engineering A*, *354*(1–2), 298–305.

Sattari, S., Bisadi, H., & Sajed, M. (2012). Mechanical Properties and Temperature Distributions of Thin Friction Stir Welded Sheets of AA5083. *International Journal of Mechanics and Applications*, *2*(1), 1–6.

Schneider, C., Weinberger, T., Inoue, J., Koseki, T., & Enzinger, N. (2011). Characterisation of interface of steel/magnesium FSW. *Science and Technology of Welding and Joining*, *16*(1), 100–107.

Shah, P. H., & Badheka, V. J. (2016). An Experimental Insight on the Selection of the Tool Tilt Angle for Friction Stir Welding of 7075 T651 Aluminum Alloys. *Indian*

*Journal of Science and Technology*, *9*(S1), 1–11.

Sharifi Asl, N., Mirsalehi, S. E., & Dehghani, K. (2019). Effect of TiO 2 nanoparticles addition on microstructure and mechanical properties of dissimilar friction stir welded AA6063-T4 aluminum alloy and AZ31B-O magnesium alloy. *Journal of Manufacturing Processes*, *38*(November 2018), 338–354.

Sharma, A., Morisada, Y., & Fujii, H. (2022). Bending induced mechanical exfoliation of graphene interlayers in a through thickness Al-GNP functionally graded composite fabricated via novel single-step FSP approach. *Carbon*, *186*, 475–491.

Sharma, A., Sharma, V. M., Gugaliya, A., Rai, P., Pal, S. K., & Paul, J. (2020). Friction stir lap welding of AA6061 aluminium alloy with a graphene interlayer. *Materials and Manufacturing Processes*, *35*(3), 258–269.

Sharma, A., Sharma, V. M., & Paul, J. (2020). Fabrication of bulk aluminum-graphene nanocomposite through friction stir alloying. *Journal of Composite Materials*, *54*(1), 45–60.

Sharma, N., Khan, Z. A., & Siddique, A. N. (2017). Friction stir welding of aluminum to copper—An overview. *Transactions of Nonferrous Metals Society of China*, *27*(10), 2113–2136.

Sharma, V., Prakash, U., & Kumar, B. V. M. (2015). Surface composites by friction stir processing: A review. *Journal of Materials Processing Technology*, *224*(May 2015), 117–134.

Shen, Z., Ding, Y., Chen, J., & Gerlich, A. P. (2016a). Comparison of fatigue behavior in Mg/Mg similar and Mg/steel dissimilar refill friction stir spot welds. *International Journal of Fatigue*, *92*, 78–86.

Shen, Z., Ding, Y., Chen, J., & Gerlich, A. P. (2016b). Comparison of fatigue behavior in Mg/Mg similar and Mg/steel dissimilar refill friction stir spot welds. *International Journal of Fatigue*, *92*, 78–86.

Shimizu, Y., Miki, S., Soga, T., Itoh, I., Todoroki, H., Hosono, T., … Koide, A. (2008). Multi-walled carbon nanotube-reinforced magnesium alloy composites. *Scripta Materialia*, *58*(4), 267–270.

Shukla, S., Wang, T., Frank, M., Agrawal, P., Sinha, S., Mirshams, R. A., & Mishra, R. S. (2020). Friction stir gradient alloying: A novel solid-state high throughput screening technique for high entropy alloys. *Materials Today Communications*, *23*(November 2019), 100869. https://doi.org/10.1016/j.mtcomm.2019.100869

Singarapu, U., Adepu, K., & Arumalle, S. R. (2015). Influence of tool material and rotational speed on mechanical properties of friction stir welded AZ31B magnesium alloy. *Journal of Magnesium and Alloys*, *3*(4), 335–344.

Singh, R., Kumar, V., Feo, L., & Fraternali, F. (2016). Experimental investigations for mechanical and metallurgical properties of friction stir welded recycled dissimilar polymer materials with metal powder reinforcement. *Composites Part B: Engineering*, *103*, 90–97.

Singh, T., Tiwari, S. K., & Shukla, D. K. (2020). Mechanical and microstructural characterization of friction stir welded AA6061-T6 joints reinforced with nano-sized particles. *Materials Characterization*, *159*(September 2019), 110047. https://doi.org/10.1016/j.matchar.2019.110047

Song, G., An, G., & Liu, L. (2012). Effect of gradient thermal distribution on butt joining of magnesium alloy to steel with Cu–Zn alloy interlayer by hybrid laser–tungsten inert gas welding. *Materials & Design*, *35*, 323–329.

Song, G., Li, T., & Chen, L. (2018). The mechanical properties and interface bonding mechanism of immiscible Mg/steel by laser–tungsten inert gas welding with filler wire. *Materials Science and Engineering: A*, *736*, 306–315.

Song, G., Li, T., Chi, J., & Liu, L. (2018). Bonding of immiscible Mg/steel by butt fusion welding. *Scripta Materialia*, *157*, 10–14.

Song, G., Li, T., Yu, J., & Liu, L. (2018). A review of bonding immiscible Mg/Steel dissimilar metals. *Materials*, *10*(12), 1–25.

Sun, Y. F., & Fujii, H. (2011). The effect of SiC particles on the microstructure and mechanical properties of friction stir welded pure copper joints. *Materials Science and Engineering A*, *528*(16–17), 5470–5475.

Sun, Y. F., Fujii, H., Takaki, N., & Okitsu, Y. (2013). Microstructure and mechanical properties of dissimilar Al alloy/steel joints prepared by a flat spot friction stir welding technique. *Materials and Design*, *47*, 350–357.

Tan, C., Li, L., Chen, Y., & Guo, W. (2017). Laser-tungsten inert gas hybrid welding of dissimilar metals AZ31B Mg alloys to Zn coated steel. *Materials & Design*, *49*, 766–773.

Tan, C., Song, X., Meng, S., Chen, B., Li, L., & Feng, J. (2016). Laser welding-brazing of Mg to stainless steel: joining characteristics, interfacial microstructure, and mechanical properties. *The International Journal of Advanced Manufacturing Technology*, *86*(1), 203–213.

Tan, C. W., Chen, B., Song, X. G., Zhou, L., Meng, S. H., Li, L. Q., & Feng, J. C. (2016). Influence of Al interlayer thickness on laser welding of Mg/steel. *Welding Journal*, *95*(10), 384-394.

Tan, C. W., Chen, Y. B., Li, L. Q., & Guo, W. (2013). Comparative study of microstructure and mechanical properties of laser welded–brazed Mg/steel joints with four different coating surfaces. *Science and Technology of Welding and Joining*, *18*(6), 466–472.

Tan, C., Xiao, L., Liu, F., Chen, B., Song, X., Li, L., & Feng, J. (2017). Influence of Laser Power on the Microstructure and Mechanical Properties of a Laser Welded-Brazed Mg Alloy/Ni-Coated Steel Dissimilar Joint. *Journal of Materials Engineering and Performance*, *26*(6), 2983–2997.

Tebyani, S. F., & Dehghani, K. (2015). Friction stir spot welding of interstitial free steel with incorporating silicon carbide nanopowders. *International Journal of*

*Advanced Manufacturing Technology*, *79*(1–4), 343–350.

Thomas, J., Chihpin Chuang, A., Das, H., Xiong, L., Upadhyay, P., & Singh, D. (2022). Three-dimensional microstructure of a friction stir welded magnesium/steel interface characterized via high-energy synchrotron X-rays. *Materials Science and Engineering: A*, *852*, 143708.

Tolephih, M. H., Mahmood, H. M., & Esam, H. H. (2013). *Effect of tool offset and tilt angle on weld strength of butt joint friction stir welded specimens of AA2024 aluminum alloy welded to commercial pure cupper*. *3*(4).

von Goldbeck, O. K. (1982). Iron-Magnesium. In *IRON-Binary Phase Diagrams*. Springer-Verlag Berlin Heidelberg GmbH.

Wahba, M., & Katayama, S. (2012). Laser welding of AZ31B magnesium alloy to Zn-coated steel. *Materials & Design*, *35*, 701–706.

Wang, F. F., Li, W. Y., Shen, J., Hu, S. Y., & dos Santos, J. F. (2015). Effect of tool rotational speed on the microstructure and mechanical properties of bobbin tool friction stir welding of Al-Li alloy. *Materials and Design*, *86*, 933–940.

Wang, K., Upadhyay, P., Wang, Y., Li, J., Sun, X., & Roosendaal, T. (2018). Investigation of Interfacial Layer for Friction Stir Scribe Welded Aluminum to Steel Joints. *Journal of Manufacturing Science and Engineering, Transactions of the ASME*, *140*(11), 1–9.

Wang, S., Wei, X., Xu, J., Hong, J., Song, X., Yu, C., … Lu, H. (2020). Strengthening and toughening mechanisms in refilled friction stir spot welding of AA2014 aluminum alloy reinforced by graphene nanosheets. *Materials and Design*, *186*, 108212.

Wang, T., Ramírez-Tamayo, D., & Jiang, X. (2020). Effect of interfacial characteristics on magnesium to steel joint obtained using FAST. *Materials and Design*, *192*, 108697.

Wang, T., Ramírez-Tamayo, D., Jiang, X., Kitsopoulos, P., Kuang, W., Gupta, V., … Upadhyay, P. (2020). Effect of interfacial characteristics on magnesium to steel joint obtained using FAST. *Materials and Design*, *192*, 108697.

Wang, T., Shukla, S., Gwalani, B., Komarasamy, M., Reza-Nieto, L., & Mishra, R. S. (2019). Effect of reactive alloy elements on friction stir welded butt joints of metallurgically immiscible magnesium alloys and steel. *Journal of Manufacturing Processes*, *39*(January), 138–145.

Wang, T., Upadhyay, P., & Whalen, S. (2020). A Review of Technologies for Welding Magnesium Alloys to Steels. *International Journal of Precision Engineering and Manufacturing - Green Technology*, (0123456789).

Wang, W., Deng, D., Mao, Z., Tong, Y., & Ran, Y. (2017). Influence of tool rotation rates on temperature profiles and mechanical properties of friction stir welded AZ31 magnesium alloy. *The International Journal of Advanced Manufacturing Technology*, *88*(5), 2191–2200.

Watanabe, T., Takayama, H., & Yanagisawa, A. (2006). Joining of aluminum alloy to steel by friction stir welding. *Journal of Materials Processing Technology*, *178*(1), 342–349.

Weng, F., Liu, Y., Chew, Y., Lee, B. Y., Ng, F. L., & Bi, G. (2020). Double-side friction stir welding of thick magnesium alloy: microstructure and mechanical properties. *Science and Technology of Welding and Joining*, *11*(4), 1–10.

Xu, R. Z., Ni, D. R., Yang, Q., Xiao, B. L., Liu, C. Z., & Ma, Z. Y. (2018). Influencing mechanism of Al-containing Zn coating on interfacial microstructure and mechanical properties of friction stir spot welded Mg–steel joint. *Materials Characterization*, *140*, 197–206.

Yi, D., Onuma, T., Mironov, S., Sato, Y. S., & Kokawa, H. (2016). Evaluation of heat input during friction stir welding of aluminium alloys. *Science and Technology of Welding and Joining*, *22*(1), 41–46.

Yusof, F., bin Muhamad, M. R., Moshwan, R., bin Jamaludin, M. F., & Miyashita, Y. (2016). Effect of surface states on joining mechanisms and mechanical properties of aluminum alloy (A5052) and Polyethylene Terephthalate (PET) by dissimilar friction spot welding. *Metals*, *6*(5). https://doi.org/10.3390/met6050101

Zhang, N., Wang, W., Cao, X., & Wu, J. (2015). The effect of annealing on the interface microstructure and mechanical characteristics of AZ31B/AA6061 composite plates fabricated by explosive welding. *Materials & Design (1980-2015)*, *65*, 1100–1109.

Zhang, Z., Wang, X., Wang, P., & Zhao, G. (2014). Friction stir keyholeless spot welding of AZ31 Mg alloy-mild steel. *Transactions of Nonferrous Metals Society of China*, *24*(6), 1709–1716.

Zhao, K., Liu, Z., Xiao, B., & Ma, Z. (2017). Friction stir welding of carbon nanotubes reinforced Al-Cu-Mg alloy composite plates. *Journal of Materials Science and Technology*, *33*(9), 1004–1008.

Zhao, S., Ni, J., Wang, G., Wang, Y., Bi, Q., Zhao, Y., & Liu, X. (2018). Effects of tool geometry on friction stir welding of AA6061 to TRIP steel. *Journal of Materials Processing Technology*, *261*, 39–49.

Zhao, Y., Lu, Z., Yan, K., & Huang, L. (2015). Microstructural characterizations and mechanical properties in underwater friction stir welding of aluminum and magnesium dissimilar alloys. *Materials & Design (1980-2015)*, *65*, 675–681.

Zhou, H., Liu, J. shui, Zhou, D. wu, & Tao, T. (2020). Effect of Al-foil addition on microstructure and temperature field of laser fusion welded joints of DP590 dual-phase steel and AZ31B magnesium alloy. *Transactions of Nonferrous Metals Society of China (English Edition)*, *30*(10), 2669–2680.

Zolghadr, P., Akbari, M., & Asadi, P. (2019). Formation of thermo-mechanically affected zone in friction stir welding. *Materials Research Express*, *6*(8), 0–11.